Using Satellite Ocean Colour to Explore Phytoplankton Dynamics and Size in East Australian Waters

Student: Leonardo Laiolo

B.Sc. (Biological Sciences)
M.Sc. (Marine Biology)

Submitted in fulfilment of the requirements
for the degree of Doctor of Philosophy in Science.

August 2018

Supervisors:

Prof. Martina Doblin

Dr. Richard Matear

CERTIFICATE OF ORIGINAL AUTHORSHIP

I, Leonardo Laiolo declare that this thesis, is submitted in fulfilment of the requirements for the award of Doctor of Philosophy, in the Faculty of Science at the University of Technology Sydney.
This thesis is wholly my own work unless otherwise reference or acknowledged. In addition, I certify that all information sources and literature used are indicated in the thesis.
This document has not been submitted for qualifications at any other academic institution.

Production Note:
Signature: Signature removed prior to publication.

Date: 23rd August 2018

ACKNOWLEDGEMENTS

I would like to thank all the people who made this PhD possible. Thank you Martina, for giving me the opportunity to do the PhD, for always encouraging me and for your logistical support. Thanks Richard, for everything you taught me, for always challenging me and for showing me the creative side of science, this has become part of me. Thanks to Monika and Allison, for your help and your patience, I learnt so much from you both and not just about science. I'm really glad for the friendship that arose from our collaborations. Mark thanks for the insightful and understanding discussions during my PhD. I would like to thank the Marine National Facility staff, the amazing crew and scientists I met aboard the *RV Investigator*. The four voyagers that I have been involved in during my PhD would have to be amongst the toughest, yet rewarding days of the past three years.

Thanks to my partner and best friend Emily, for showing me the bright side of everything even on the stressful days. Ana and Giulia, I wish to thank you for making me feel at home, and always being there to listen. Daniel, thanks for the chilled evenings at home after the hard days at work, it was a pleasure sharing that quirky house with you. Thanks to the Tasmanian waves, that always brought me peace and mindfulness even on the toughest days. And thanks to the boys of Taroona Football Club, for being welcoming since the first day and making me feel part of a soccer team, a joy that reminds me of home.

Thanks to my family for being understanding, supportive and so enthusiastic to maintain constant contact, despite the distance with me living across the world. Last but not least, thanks to myself for never giving up, maintaining high spirits following my passions.

TABLE OF CONTENTS

CERTIFICATE OF ORIGINAL AUTHORSHIP ..... **i**
ACKNOWLEDGEMENTS ..... **ii**
TABLE OF CONTENTS ..... **iii**
LIST OF ILLUSTRATIONS ..... **vi**
LIST OF TABLES ..... **xii**
LIST OF ABBREVIATIONS ..... **xiv**
ABSTRACT ..... **xvi**
CHAPTER 1 – General Introduction **1**
1.1 Phytoplankton 2
1.2 Off shore Eastern Australian waters 4
1.2.1 Physical dynamics 4
1.2.2 Phytoplankton dynamics 8
1.2.3 Climate change impacts to the ocean 10
1.3 Modelling phytoplankton dynamics 11
1.3.1 Biogeochemical models approaches 11
1.3.2 Data assimilation: calibrating biogeochemical models 15
1.3.3 Satellite remote sensing of ocean colour 17
1.4 Objectives of this thesis 19

CHAPTER 2 – Key drivers of seasonal plankton dynamics in cyclonic and anticyclonic eddies off East Australia **21**
2.1 Abstract 22
2.2 Introduction 23
2.3 Materials and Methods 27
2.3.1 Study region and location of voyage experiment 27
2.3.2 Description of biogeochemical models 27
2.3.3 Input data and implementation to biogeochemical models 29
2.3.4 Statistical analysis and goodness of the fit 31
2.3.5 Data assimilation 32
2.3.6 Shipboard manipulation experiment 34
2.4 Results 35

2.4.1 Characterization of cyclonic and anticyclonic eddies....35
2.4.2 WOMBAT and EMS simulations....37
2.4.3 Shipboard manipulation experiment....42
2.5 Discussion....44
2.5.1 The role of mixed layer depth and light on phytoplankton....44
2.5.2 Phytoplankton composition and size structure....45
2.5.3 Zooplankton....46
2.6 Conclusion....47
2.7 Acknowledgments....48

CHAPTER 3 – Information content of *in* situ and remotely sensed chlorophyll-*a*: learning from size-structured phytoplankton model....49
3.1 Abstract....50
3.2 Introduction....51
3.2.1 Model simulations to understand observation platforms....54
3.3 Materials and Methods....55
3.3.1 Study Region and Biogeochemical Model Description....55
3.3.2 Simulated surface Chlorophyll-*a* and simulated OC3M Chlorophyll-*a* synthetic dataset....57
3.3.3 Settings of the twin experiments....60
3.4 Results....62
3.4.1 Simulated surface Chlorophyll-*a* and simulated OC3M Chlorophyll-*a* dataset....62
3.4.2 Twin experiments....63
3.5 Discussion....67
3.6 Conclusion....72
3.7 Acknowledgments....73

CHAPTER 4 – Comparing size fractionated *in* situ chlorophyll-*a* measurements with a satellite ocean colour product in Eastern Australian open ocean waters....74
4.1 Abstract....75
4.2 Introduction....76
4.3 Materials and Methods....79

4.3.1 Area of the Study 79
4.3.2 *In situ* size fractionated chlorophyll-*a* measurements 81
4.3.3 Ocean colour observations 84
4.3.4 Satellite Chl-*a* product and *in situ* Chl-*a* measurements comparison 85
4.3.5 Optical Model 86
4.4 Results 87
4.4.1 Satellite Chl-*a* product and *in situ* Chl-*a* measurements comparison 87
4.4.2 Optical model simulations 92
4.5 Discussion 94
4.6 Conclusion 99
CHAPTER 5 – General Discussion 101
5.1 Summary 102
5.2 Implications for primary productivity 104
5.3 Implications for upper trophic levels 107
5.4 *In situ* and remotely-sensed measurements 108
5.5 Future research 110
Appendix 1 113
References 117

LIST OF ILLUSTRATIONS

Figure 1.1: Representation of Australia with focus on eastern Australia offshore waters physical dynamics. This area is strongly influenced by the Eastern Australian Current (EAC) that originates from the warm oligotrophic waters of the Coral Sea (Cor. Sea) and flows southward forming eddies. In the figure is represented the Tasman Front as well (Tas. Front).

Figure 1.2: Sea surface height anomalies in a wide area off eastern Australia on a 8-day remotely sensed averaged dataset. Colours span from pink (representing -0.52 m low sea level anomalies) to red (representing +0.40 m high sea level anomalies).

Figure 1.3: Conceptual diagram of a NPZD biogeochemical model structure.

Figure 1.4: Global surface Chl-*a* concentration (mg m^{-3}) from GlobColour climatology (August 2014) computed from 8-day composite, 4-km resolution product.

Figure 2.1: Map showing the study area, including the location of the where water was collected for the shipboard manipulation experiment (CTD35 IN2015_V03).

Figure 2.2: Structure of biogeochemical models used in this study. Arrows represent interactions and links between model compartments. A) WOMBAT (Whole Ocean Model of Biogeochemistry And Trophic-dynamics), which has one phytoplankton (P) and one zooplankton (Z) class, detritus (D) and one nutrient compartment (N). B) EMS (Environmental Modelling Suite), characterized by two phytoplankton (P) and zooplankton (Z) sized-based classes, detritus (D) and one nutrient compartment divided into dissolved inorganic carbon, nitrogen, phosphate (DIC, DIN, DIP) and dissolved organic carbon, nitrogen, phosphate (DOC, DON, DOP).

Figure 2.3: Seasonal climatology of the study area (-30°S -40°S, 150°W 160°E) for A) surface temperature; B) surface irradiance; C) nitrate concentration 5 m below seasonal mixed layer depth. Data for A and C

come from the CSIRO Atlas of Regional Seas (CARS) available at http://www.marine.csiro.au/~dunn/cars2009/. Data for B comes from seasonal climatology of the downward short wave radiation at the surface of the ocean (Large and Yeager 2008).

Figure 2.4: Seasonal climatology of cold core CE (solid blue lines) and warm core ACE (solid red lines) eddies for: A) mixed layer depth (MLD) (GODAE); B) surface chlorophyll-a concentration (GlobColour). The light blue and light red areas represent standard deviation for CE and ACE, respectively.

Figure 2.5: WOMBAT's acceptable solutions obtained from data assimilation. Left column shows ACE seasonality and right column CE seasonality. The red solid lines in plots A and B show the Chl-a observed seasonal climatology with the red shading denoting the standard deviation variability. In all remaining plots, the blue areas represent WOMBAT acceptable solutions. Plots C (ACE) and D (CE) represent primary production (g C m^{-2}) while plots E and F represent the zooplankton dynamics for the ACE and CE systems, respectively.

Figure 2.6: EMS acceptable solutions from the data assimilation. Left column shows ACE seasonality and right column CE seasonality. The red solid lines in plots A and B show the Chl-a observed seasonal climatology with the red shading denoting the standard deviation variability. Patterns of the two EMS phytoplankton classes (Chl-a) are represented in plot C (ACE) and D (CE), where red areas represent the large phytoplankton class (40 μm diameter) and blue areas represent the small phytoplankton class (2 μm diameter). Plots E (ACE) and F (CE) represent the total primary production (g C m^{-2}) in black and the primary production for small (blue) and large phytoplankton (red). The total zooplankton biomass (g C m^{-2}) is represented in black on plots G (ACE) and H (CE), while the small and large zooplankton biomass is represented in blue and red, respectively.

Figure 2.7: Pigment analysis of phytoplankton in different treatments (shipboard incubation experiment): A) size distribution at the initial and

final time of the experiment; B) ratio between characteristic phytoplankton classes pigment and total Chl-*a* (Diatoms: Fucoxanthin, Haptophytes: 19-Hex-fucoxanthin, Synechococcus: Zeaxanthin, *Prochlorococcus*: DV Chlorophyll *a*, Barlow et al. (2004)). In all panels it is represented the "T0 (110m)" showing the initial condition and the "T final" showing the last day of the experiment (6th day). The treatments are labelled as: LL (20% surface irradiance), HL (40% surface irradiance), N (daily nutrients addition). The control (CON, ~1% incident light, no nutrient amendment). The CON is not represented at the end of the experiment (T final) because the pigment concentrations were below detection (>0.004 µg/L).

Figure 3.1: Diagrams representing how the two synthetic datasets were created (panel a) and how the twin experiments were conducted (panel b).

Figure 3.2: Australian region and the study area highlighted by the dashed line (150° E – 160° E; 30° S – 40° S). To illustrate the main features (cyclonic eddy CE, anticyclonic ACE, East Australian Current EAC) occurring in the study area, the satellite image of surface Chl-*a* calculated with OC3M algorithm using reflectance acquired with the MODIS radiometer (2nd April 2016) and the current pattern based on altimeter data is shown. Data source: Australia's Integrated Marine Observing System (http://oceancurrent.imos.org.au/oceancolour.php).

Figure 3.3: Simulated seasonal climatology of total Chl-*a* concentration (solid black line), Chl-*a* in small phytoplankton (blue dotted) and Chl-*a* in large phytoplankton (red dashed line) for CE (a) and ACE (b) off East Australia. The green line represents seasonal climatology for CE (a) and ACE (b) off East Australia (Laiolo et al. 2016) calculated from GlobColour (25 km spatial resolution, 8-day average; http://hermes.acri.fr/index.php?class=archive), while the shaded green areas represent the corresponding standard deviation. The middle panel shows for the same simulations, the corresponding simulated OC3M Chl-*a* obtained from the R_{rs} calculated from the simulated surface Chl-*a* for the two phytoplankton classes (panels a and b) for CE (c) and ACE (d). Note there is a different scale on the Chl-*a* concentration between panel a - c

and b - d. The lower panel compares the simulated surface Chl-*a*, with the corresponding simulated OC3M Chl-*a* for CE (e) and ACE (f).

Figure 3.4: For various pairs of parameters, the region of parameter values that produced acceptable fits to the data. Here we show results for CE as similar plots were obtained for ACE. Black circles represent the global minimum, where the cost function is equal to zero. Red shaded areas represent acceptable solutions for the simulated surface Chl-*a* assimilation; within this area, light red shows cost function equal to one highlighting local minima. Red dashed lines show the simulated surface Chl-*a* cost values. Blue dashed lines and blue shaded areas show the simulated OC3M Chl-*a* cost values. Shaded blue areas represent acceptable solutions; within this area, light blue shows a cost function equal to one, highlighting local minima. Acceptable solutions (i.e., (x)<1 and (α)<1) are represented by values less than two.

Figure 3.5: Absorption, backscattering and R_{rs} spectra of small (2 μm) (left column) and large (40 μm) (right column) phytoplankton classes for different ratios of phytoplankton Carbon (C) to Chl-*a*. The black lines represent a scenario with 0.3 mg m^{-3} of Chl-*a* and 6 mg m^{-3} C (C:Chl-*a* 20:1); the red lines represent a scenario with 0.3 mg m^{-3} of Chl-*a* and 15 mg m^{-3} C (C:Chl-*a* 50:1); the green lines represent a scenario with 0.3 mg m^{-3} of Chl-*a* and 30 mg m^{-3} C (C:Chl-*a* 100:1); and the blue lines represent a scenario with 0.3 mg m^{-3} of Chl-*a* and 45 mg m^{-3} C (C:Chl-*a* 150:1). The amount of Chl-*a* and C in the left and right columns are equal and entirely distributed in the small phytoplankton class (left) or large phytoplankton class (right). Panels a and b show absorption spectra, panels c and d backscattering and panels e and f the R_{rs} for the two phytoplankton classes.

Figure 4.1: Different scenarios showing phytoplankton abundance (a), size structure (b) and pigment content changes (c) related to increased Chl-*a*.

Figure 4.2 (a): The Australian region and physical features that characterise eastern Australian waters. The study area is highlighted by

the dashed line (150° E – 160° E; 30° S – 40° S). **(b)** Location of the match-up points # (Table 4.1) are represented by #, while non match-up points are represented by CTD # (Table 4.2) inside circles. The background is a Globcolour Chl-*a* (mg m^{-3}) satellite field averaged from the 31st August to 16th September 2016. White areas indicate land or no data.

Figure 4.3: Comparison between *in situ* and satellite Chl-*a* match-up points. (a) Comparison between the size fractionated Chl-*a* and the satellite Chl-*a* through bar charts. While grey bars represent the satellite Chl-*a*, the narrow blue, green and red bars show the *in situ* Chl-*a* for the small (< 2 μm), medium (between 2 to 10 μm) and large (> 10 μm) phytoplankton class respectively. Errors bars represent the standard deviation in the 3x3 pixel box that has been used for the matchup with the *in situ* Chl-*a*. (b) Relationship between total *in situ* Chl-*a* and satellite Chl-*a*. The green solid line indicates a 1:1 relationship and dashed green lines show the ± 35% uncertainty interval.

Figure 4.4: Relationship between *in situ* Chl-*a* and satellite Chl-*a.* Red dots and corresponding red linear regression lines represent the direct comparison between *in situ* Chl-*a* vs satellites Chl-*a*. The green dots and lines show the linear fit to the remotely sensed Chl-*a* where a different weighting is given for the *in situ* Chl-*a* associated with small, medium and large phytoplankton. Panel (a) shows regression model A in red font and regression model C in green font. The regression model B (in red) and regression model D (in green) are represented in panel (b). (c) The bar chart shows the size distribution (%) of the phytoplankton community for every match-up point. Match-up point's numbers correspond to numbers in Table 4.1 and Fig. 4.2.

Figure 4.5: Bio-optical properties in different simulated scenarios obtained through the optical model (Bair et al., 2016). The three columns represent three different Chl-*a* concentration, 0.2, 1.0 and 3.0 mg m^{-3} respectively. The first three rows show the corresponding absorption, backscattering and R_{rs} for the wavelength 443 nm in function of increasing phytoplankton

sizes, while the fourth row shows the R_{rs} for the wavelength 551 nm. The last row is showing the simulated satellite-like Chl-*a* product. Different ratios of phytoplankton Carbon (C) to Chl-*a* are represented in black (20:1), red (50:1), green (100:1) and blue (150:1) lines. Correspondent phytoplankton abundances (cells L^{-1}) are shown at the bottom of the figure with the same colour scheme.

Figure 4.6: Simulated satellite Chl-*a* normalised by the 1 µm phytoplankton cells (3 mg m^{-3} Chl-*a* scenario from Fig. 4.5q). The figure shows C:Chl-*a* included between 20:1 and 150:1 in function of increasing phytoplankton sizes. The red area is comparing the simulated satellite-like Chl-*a* produced by 1 µm phytoplankton cells with the simulated satellite-like Chl-*a* produced by 10 ± 1 µm phytoplankton cells.

Figure 5.1: Conceptual diagram showing the key results of the thesis.

Figure 5.2: Primary prouctivity in ACE (left column) and CE (right column) before and after considering the remotely sensed Chl-*a* underestimation associated with large-sized phytoplankton. Dashed lines in all panels show the primary productivity from Laiolo et al., 2016 (Chapter 2), while solid lines show the corrected primary productivity based on Chapter 4 (Table 4.2). Panels a and b represent the total primary productivity, panels c and d separate the total primary productivity into large (40 µm) and small (2 µm) phytoplankton contributions.

LIST OF TABLES

Table 2.1: Schematic representation of main physical and biological differences between CE and ACE off East Australia.

Table 2.2: Results of the statistical comparisons (student-t test): Chl-a means (observed vs simulated, ACE observed vs CE observed) and MLD means (ACE observed vs CE observed). Results at significance values are highlighted: N.S. indicates not significant ($p > 0.05$); * indicates $p < 0.05$; ** $p < 0.01$; and *** $p < 0.001$. χ^2 indicates the Chi-squared misfit value: the closer χ^2 is to 1, the more accurate the simulation. In this table, "p" and "χ^2" intervals represent the minimum and the maximum value obtained from acceptable solutions. Simulations were considered acceptable when both $p > 0.05$ and $\chi^2 > 2.5$.

Table 2.3: WOMBAT parameter set for CE and ACE fitted independently, and the optimized parameter set fitting the two environments simultaneously (CE + ACE).

Table 2.4: EMS parameter set for CE and ACE. EMS contains a total of 104 different parameters, in this table are shown only the parameters that were allowed to vary during the data assimilation analyses (except large and small phytoplankton cells diameter, remineralization rate and sinking velocity).

Table 3.1: EMS 'original parameter set' for cyclonic eddy (CE) and anticyclonic eddy (ACE) used to obtain the simulated surface Chl-*a* dataset; T_{ref} refers to reference temperature (Laiolo et al., 2016). The sub-set of parameters included in this study is composed of large phytoplankton natural (linear) mortality, small phytoplankton natural (linear) mortality rate, large zooplankton natural (quadratic) mortality and small zooplankton natural (quadratic) mortality.

Table 4.1: Details about the match-up points, CTD number (CTD #), *in situ* sampling time, location and total Chl-*a* (TChl-*a in situ*). The averaged Chl-*a* from satellite measurements (Avg Chl-*a* satellite), the corresponding standard deviation (SD), the coefficient of variation (CV) and number of satellite observations (i.e., pixels averaged) are shown in the last columns.

Table 4.2: Details about the stations sampled that have no corresponding satellite match-up measurements. The table shows CTD number (CTD #), *in situ* sampling time, location, site and total Chl-*a* (TChl-*a in situ*). The contribution to the TChl-*a in situ* from the three different phytoplankton size classes (i.e., Small <2, Medium between 2 μm and 10 μm and Large >10 μm) is represented in percentages in the last columns. The "Site" column indicates stations near the continental shelf (c.s.) and off-shore stations (o.s.).

Table 4.3: Weighting applied to the *in situ* size-fractionated Chl-*a* to produce the least squares best fit to the satellite Chl-*a* values. A measure of the fit is given by R^2 values. While x corresponds to the in situ observations and y to the corresponding satellite Chl-*a*. P represents *p*-values obtained testing the data against a slope of 1, Eq. (5).

LIST OF ABBREVIATIONS

a	Absorption coefficient
ACE	Anticyclonic eddy
AOPs	Apparent optical properties
b_b	Backscattering coefficient
C	Carbon
CARS	CSIRO Atlas of Regional Seas
CDOM	Coloured dissolved organic matter
CE	Cyclonic eddy
Chl-*a*	Chlorophyll-*a* concentration
Chl-a_{lrg}	Percentage of Chl-*a* concentration in the large (> 10 µm) phytoplankton class
Chl-a_{med}	Percentage of Chl-*a* concentration in the medium between 2 and 10 µm) phytoplankton class
Chl-a_{sml}	Percentage of Chl-*a* concentration in the small (< 2 µm) phytoplankton class
CO_2	Carbon dioxide
c.s.	Continental shelf station
CV	Coefficient of variation
DA	Data assimilation
EAC	East Australian Current
EMS	Environmental Modelling Suite
IOPs	Inherent optical properties
MODIS-Aqua	Moderate Resolution Imaging Spectroradiometer
NAP	Non-algal particulates
NPZD	Nutrient, Phytoplankton,

	Zooplankton and Detritus
O_2	Oxigen
OC3M	Band ratio algorithm of Chl-*a* concentration for data from MODIS radiometer
OLCI	Ocean and Land Colour Instrument
o.s.	Off-shore station
R_{rs}	Remote sensing reflectance
RS	Regression slope
SD	Standard deviation
SE	Standard error
SeaWIFS	Sea-Viewing Wide Field-of-View Sensor
simulated OC3M Chl-*a*	Satellite-like Chl-*a* product obtained from EMS output
simulated surface Chl-*a*	*In situ*-like Chl-*a* measurements
TChl*a*	Total chlorophyll-*a*
TSS	Total suspended particles
VIIRS	Visible Infrared Imaging Radiometer Suite
WOMBAT	Whole Ocean Model of Biogeochemistry And Trophic-dynamics

ABSTRACT

The eastern Australian ocean region is strongly influenced by the East Australian Current (EAC). Waters in this region are generally oligotrophic; despite this, nutrient enrichment and phytoplankton blooms occur as a response to physical events such as the seasonal deepening of the mixed layer or the formation of cyclonic eddies. In this PhD project, biogeochemical and optical modelling, ocean color data assimilation, *in situ* measurements and ship-board experiments were used to investigate phytoplankton dynamics and size structure in offshore eastern Australian waters, information that is necessary to improve estimates of future ocean primary productivity.

First, the seasonal phytoplankton dynamics in averaged cyclonic and anticyclonic eddies (CE and ACE, respectively) off eastern Australia were explored through a single and a multi-phytoplankton class biogeochemical model. Seasonal climatologies of surface chlorophyll-*a* concentration (Chl-*a*) and mixed layer depth for both CE and ACE were obtained by combining remotely sensed sea surface height, remotely sensed ocean color and *in situ* profiles from Argo floats. Simulated phytoplankton responses to changes in nutrients and light were compared with a ship-based experiment. The experimental results were consistent with the model result, where the seasonal deepening of the mixed layer during winter produced a rapid increase in large phytoplankton. Although the Chl-*a* concentration in CE was larger than ACE, the primary production estimates obtained through the assimilation of the ocean colour product within different types of eddies were similar, showing an inconsistency with previously published studies that suggest CE are significantly more productive.

To explore the properties and relationship of the satellite ocean colour product and *in situ* observations, theoretical experiments were performed through a coupled biogeochemical-optical model. Specifically, an optical model was used to calculate the inherent optical properties (IOPs) of seawater from size dependent multi-phytoplankton

biogeochemical model simulations and convert them into remote-sensing reflectance (R_{rs}). Then, R_{rs} was used to produce a satellite-like estimate of the simulated surface Chl-*a* concentration through the OC3M algorithm. The information content of simulated *in situ* and simulated remotely-sensed data sources was investigated through theoretical experiments that suggested the OC3M algorithm underestimates the simulated Chl-*a* concentration because of the weak relationship between large-sized phytoplankton and R_{rs}.

Finally, this concept was tested with real data collected on a voyage in 2016, to investigate the relationship between the *in situ* sampled phytoplankton size structure and the corresponding satellite Chl-*a* product. Ocean colour match-up points confirmed the underestimation of *in situ* Chl-*a* concentrations when phytoplankton larger than 10 μm dominated the photosynthetic community. Furthermore, optical model simulations suggested that large phytoplankton cells cause a decrease in both the absorption and backscattering signals, which in turn affect the R_{rs} and cause the underestimation of Chl-*a* by the satellite Chl-*a* product.

To understand impacts of contemporary ocean change on regional primary productivity, we rely on biogeochemical models to scale up sparse *in situ* observations. Although ocean colour provides information at high spatial and temporal resolution, this information has limited accuracy. Results presented in this thesis show that a simultaneous assimilation of *in situ* and satellite remote sensing can provide additional information about the phytoplankton size structure, crucial data to progress our understanding of processes influencing regional primary productivity and elemental cycling. Therefore, parameter optimization through a combination of the information provided by two distinct observation platforms (*in situ* and satellite remote sensing) will lead to the development of next-generation biogeochemical models.

CHAPTER 1

General Introduction

Currently, our understanding of the global distribution and seasonal dynamics of phytoplankton depends largely on satellite observations. Specifically, thanks to their spatial and temporal resolution, remotely sensed observations are particularly suitable for modelling physical and biological ocean dynamics. Therefore, there is an increasing need to better understand the connections between satellite ocean colour radiometry and the quantities simulated by biogeochemical models. This PhD thesis explores these relationships through a multidisciplinary approach, integrating biogeochemical and optical modelling with satellites and *in situ* observations.

1.1 Phytoplankton

Microscopic, photosynthetic unicellular organisms comprise the phytoplankton; in oceans and fresh waters these organisms can be found in the euphotic zone and are assembled into communities characterised by enormous biodiversity. Significant changes in phytoplankton dynamics can have planetary-scale consequences (Falkowski, 2012). Phytoplankton are the dominant primary producers in the oceans and are therefore involved in many fundamental processes, from providing organic matter (directly or indirectly) for almost all marine life (Brussaard et al.,1996), including supporting fisheries (Pauly and Christensen, 1995), to biogeochemical cycles (Falkowski, 1994; Falkowski et al., 2008) and influencing the Earth's climate balance (Falkowski, 2012). Furthermore, all autotrophic and mixotrophic phytoplankton consume carbon dioxide (CO_2) to grow, regulating the ocean's pH and the planet's atmospheric composition (Falkowski et al., 2012). Thanks to the daily periodicity of the photosynthesis process, CO_2 is fixed during the day to draw down dissolved CO_2 while producing reserves of energy in the form of organic compounds, and releasing oxygen (O_2) (Doty and Oguri, 1957). Then, due to gas exchange across the sea surface, O_2 is released to the atmosphere (Kanwisher, 1963).

In addition to mediating the CO_2 and O_2 content of the ocean and

atmosphere, phytoplankton need to take up dissolved nutrients (e.g., nitrogen: NO_3, NH_4^+ and phosphorus: PO_4) from the water column to grow, affecting nutrient availability in the oceans and the elemental ratio of phytoplankton, contributing to the well known Redfield ratio 1:16:106 (P:N:C) (Redfield, 1934; Redfield, 1963). Due to their different nutrient requirements, phytoplankton have different roles and implications in biogeochemical cycles of different elements. Several major groups are discussed below.

Diatoms or Bacillariophyceae, are a class of silica shelled phytoplankton, with a key role in the regulation of the ocean's silica cycle (Yool and Tyrrell, 2003): it has been estimated this phytoplankton group take up ~240 Tmol Si yr^{-1} (Tréguer et al., 1995). Furthermore, this phytoplankton class is thought to play an important role in the export of carbon from ocean surface waters (Dugdale and Wilkerson, 1998), contributing to ~45% of total oceanic primary production (Mann et al., 1999).

Diazotrophs are nitrogen-fixing cyanobacteria (Postgate, 1998). The ability to fix atmospheric N_2 into different nitrogen forms (e.g., NH_4^+) results in this group of phytoplankton being considered an indirect source of biologically usable nitrogen in the ocean (Montoya et al., 2004). Due to their ability to fix nitrogen, this phytoplankton functional group prefers to grow in areas where nitrate concentrations are low (Montoya et al., 2004). The contribution to N_2 fixation of *Trichodesmium* (one of the dominant diazotrophs in the ocean) is estimated to be around 50% of the global marine N_2 fixation (Bergman et al., 2013).

The Coccolithophyceae is another class of unicellular phytoplankton. This class comprises coccolithophores, single celled organisms with calcareous plates (coccoliths) made through a biomineralization process, which form a type of exoskeleton (Moheimani et al., 2012). Coccolithophores act as a carbon sink due to the sinking of dead cells out of the euphotic zone (Moheimani et al., 2012). Evidence of this sedimentation process is found in the white cliffs of Dover (UK), which

are comprised of coccoliths accumulated over millennia (Witty, 2011). It is estimated that this phytoplankton group is the major contributor (up to 50%) to the open ocean carbonate pump (Iglesias-Rodriguez et al. 2008).

Prochlorococcus is a genus of the order Prochlorophyta characterized by submicron dimensions, usually around 0.6 μm (Morel et al., 1993). *Prochlorococcus* is considered the smallest known photosynthetic organism (Partensky et al., 1999). This genus is found almost everywhere in the ocean apart from polar waters, with a preference for oligotrophic environments (Partensky et al., 1999; Flombaum et al., 2013). The global net primary production of *Prochlorococcus* is around 9% of ocean primary production (Flombaum et al., 2013).

In modelling terms, these different phytoplankton (i.e., diatoms, diazotrophs, coccolithophores, picocyanobacteria) involved in various elemental transformations, may be considered a single phytoplankton group represented by the chlorophyll-*a* concentration (Chl-*a*) value. On the other hand, the advantage of considering multiple phytoplankton classes is to unlock additional information about phytoplankton impacts on different biogeochemical cycles and ecosystem services, giving an improved picture of the ecosystem.

1.2 Offshore Eastern Australian waters

1.2.1 Physical dynamics

The eastern Australian ocean region is significant for Australia's economy and marine ecology. This area is adjacent to major tourist destinations, major shipping lanes and includes regions of environmental significance (e.g., Great Barrier Reef World Heritage area). Pelagic offshore fisheries, including the valuable Bluefin tuna market, are influenced by physical processes that characterize the offshore eastern Australian waters (Hobday and Hartmann, 2006). Furthermore, the ocean circulation of this region has a crucial role in removing heat from the tropics and releasing it to the mid-latitude atmosphere (Roemmich et al., 2005).

Due to its importance, the area selected for this study is located in eastern Australian waters, between 30°S to 40°S and 150°E to 160°E. Its oceanographic characteristics are strongly influenced by the East Australian Current (EAC) (Figure 1.1).

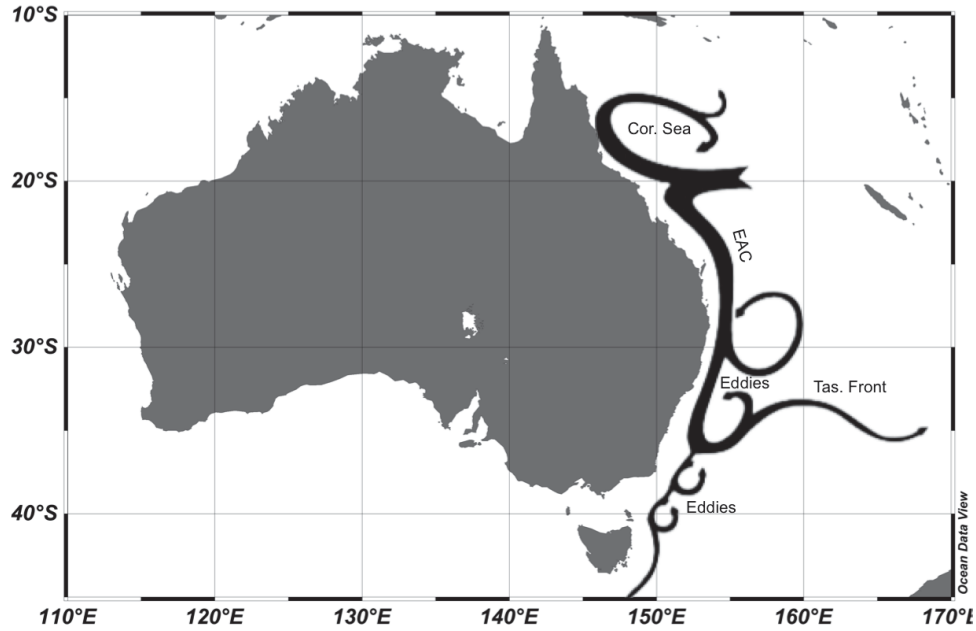

Figure 1.1: Representation of Australia with focus on eastern Australia offshore waters physical dynamics. This area is strongly influenced by the Eastern Australian Current (EAC) that originates from the warm oligotrophic waters of the Coral Sea (Cor. Sea) and flows southward forming eddies. In the figure is represented the Tasman Front as well (Tas. Front).

Typically more than 30 km wide, 200 m deep, flowing up to 2 m s^{-1}, the EAC is the major western boundary current of the South Pacific sub-tropical gyre (Mata et al., 2000; Ridgway and Dunn, 2003). It originates from the warm oligotrophic waters of the Coral Sea and flows southward along the New South Wales coast. At around 32°S the EAC separates from the coast, generating uplift of nutrient-rich water (Godfrey et al., 1980). Occasionally, the EAC forms meanders before flowing into the southwest Tasman Sea (Hamon, 1965; Tranter et al., 1986). These meanders move away from the EAC, forming eddies that drift in a southward direction, where they are usually engulfed by the next

southward surge of the EAC (Tranter et al., 1986). EAC waters are generally low in nutrients, due to their Coral Sea water source, and any subsurface nutrients are rarely upwelled to the euphotic zone (Oke and Griffin, 2011). Despite this, nutrient enrichment and algal blooms occur in NSW ocean waters as a response to occasional upwelling-favorable wind events, the separation of EAC from the shelf or the formation of cyclonic eddies (Tranter et al., 1986; Cresswell, 1994; Roughan and Middleton, 2002). In particular, eddies have a crucial role in stimulating phytoplankton growth and primary production in oligotrophic water (Falkowski et al., 1991).

Eddies are not just features of eastern Australia. They occur where major currents and oceanic fronts are present (Robinson, 1983). The direction of an eddy circulation can be categorized as cold core cyclonic or warm-core anticyclonic (Robinson, 1983, Yasuda et al., 2000). Eddys diameter can range from tens to hundreds of kilometres and they can persist for up to 3 years (Angel and Fasham, 1983). Eddies separate from the EAC or from a front meander and move into adjacent water, which has different physical, chemical and biological characteristics (Lochte and Pfannkuche, 1987). Cyclonic eddies (CEs) and anticyclonic eddies (ACEs) represent two distinct environments, characterized by different physical processes (Angel and Fasham, 1983). In south-eastern Australian waters it has been shown that CEs have almost double the Chl-*a* of ACEs (Everett et al., 2012). The formation and intensification of CEs create low sea level anomalies and upwelling; these processes in relation to CEs, are usually called ‘‘eddy pumping’’ (Dietze et al., 2009). Eddy pumping can cause uplift of high nutrient waters at depth into the euphotic zone, thereby stimulating new phytoplankton activity (Jenkins, 1988; Falkowski et al., 1991; McGillicuddy and Robinson, 1997). This primary production supports higher trophic levels, including zooplankton and larval fish (Froneman and Perissinotto, 1996). Phytoplankton usually have higher abundance (manifest as greater concentrations of Chl-*a*) in the centre of CEs (Oschlies and Garcon, 1998). For phytoplankton production to

manifest at the ocean's surface and hence be detectable by satellite, turbulent vertical mixing, driven by the surface wind and/or negative surface buoyancy flux is needed to transport phytoplankton and nutrients into the upper euphotic zone (Carder et al., 1986). In contrast, the formation and intensification of ACEs is accompanied by downwelling of nutrient-depleted surface waters, which deepens the surface mixed layer, leading to high sea level anomalies (Robinson, 1983). As this process does not drive transport of new nutrients to the euphotic zone, usually phytoplankton growth is not stimulated in these areas. In addition, ACEs reduce the average light level in the surface mixed layer (Tilburg et al., 2002). Figure 1.2 shows a snapshot of the sea surface height that gives a clear idea of the importance of both kinds of eddies in eastern Australian waters.

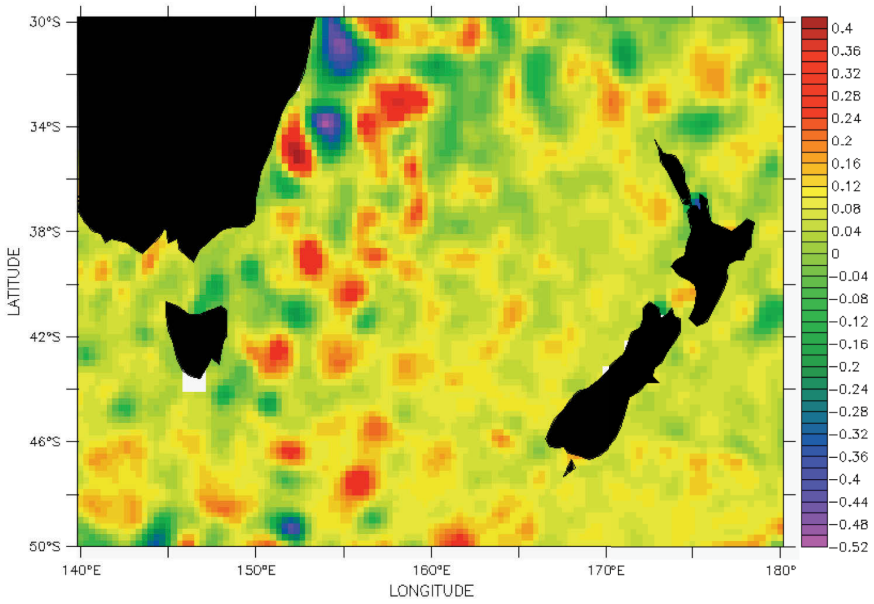

Figure 1.2: Sea surface height anomalies in a wide area off eastern Australia on a 8-day remotely sensed averaged dataset. Colours span from pink (representing -0.52 m low sea level anomalies) to red (representing +0.40 m high sea level anomalies).

Not all EAC eddies fit this general model however; different physical events can lead to different biological responses. For example, eddies can remain as an independent body of water or be reabsorbed into the parent current (Nilsson and Cresswell, 1981). They can also be subjected to

flooding (Tranter et al., 1982; Baird et al., 2011), overlie and coalesce with another eddy (Cresswell, 1982), or move to the south and die away. Furthermore, the timing of eddy formation is an important factor in the sequence of biological development within eddies (Angel and Fasham, 1983): cold core eddies developed in early winter can be less productive than similar cold core eddies developed during spring, because of low light levels (e.g., Crawford et al., 2007).

Due to their different physical characteristics, CEs and ACEs represent two natural laboratories that can lead to different phytoplankton concentration and composition. Given their influence on phytoplankton dynamics, it is therefore important to include these mesoscale features in circulation models if we are to advance our understanding of biogeochemical cycles and ecosystem services in the region.

1.2.2 Phytoplankton dynamics

Offshore eastern Australian waters can be compared to other open ocean oligotrophic systems, where phytoplankton concentration and composition are driven mainly by physical events (Levy and Klein, 2004). Different upwelling, downwelling and mixing phenomena (typical in eddies as well) can lead to a change in the nutrient concentration and the light available for photosynthesis, which in turn influences the Chl-*a* cells content and the phytoplankton abundance and community composition (Officier and Ryther, 1980; Pitcher et al., 1991; Tilburg et al., 2002). According to the Sverdrup hypothesis, phytoplankton growth is strongly stimulated only if the mixed layer depth (MLD) is shallower than the depth at which phytoplankton growth rate is equal to loss rate (Sverdrup, 1953). According to this theory, during wintertime the deepening of the MLD uplifts nutrients but this condition is not enough to make the phytoplankton abundance rise significantly (Sverdrup, 1953). Conversely, when the MLD shallows and the light increases, typically during spring, phytoplankton can easily grow (Behrenfeld and Boss, 2014).

High nutrient concentration is not the only factor that controls

phytoplankton growth; in particular irradiance and grazing pressure play a crucial role in determining phytoplankton dynamics (e.g., Frost, 1991; Irigoien, 2005; Behrenfeld, 2010). Since different phytoplankton species have distinctive growth preferences (e.g., optimum light value, nutrients), specific phytoplankton will grow under different conditions (e.g., Lancelot et al., 2000; Anderson et al., 2002; Paerl and Huisman, 2008).

Previous studies in eastern Australian waters were mainly focused on modelling the physics of the EAC and its eddies (e.g., Oke and Middleton, 2001; Tilburg et al., 2001). Investigations of phytoplankton community composition and blooms have been less frequent, and focused on coastal waters (e.g., Hallegraeff, 1981; Ajani et al., 2001; Pritchard et al., 2003; Lee et al., 2007; Thompson et al., 2009; Thompson et al., 2010), characterised by events such as riverine input or coastal upwelling, and are therefore not comparable to offshore eddy dynamics (Atkinson et al., 2004). Other works were focused on particular eddy processes, trying for example to understand the effect of a surface flooding event on an ACE, but have not characterized the phytoplankton community (e.g., Baird 2011). Only one study has characterized the phytoplankton composition of a typical ACE in offshore East Australia (i.e., Jeffrey and Hallegraeff 1980). There were small differences in the phytoplankton community and Chl-*a* concentration between the ACE center and the surrounding waters during the summer season (Jeffrey and Hallegraeff, 1980). These small differences include an increase in diatom abundance and a decrease in nanoplankton from the eddy edge to the eddy center (Jeffrey and Hallegraeff, 1980). Other studies, carried out in similar oligotrophic systems, confirm higher levels of Chl-*a* in the boundaries of warm core eddies rather than in the center, and phytoplankton communities comparable to the source waters (e.g., Huang et al. 2010, Haury, 1983). These results are consistent with the downwelling process that characterizes warm core eddies and attracts surrounding waters, making the center of warm core eddies nutrient depleted and thus low in Chl-*a* concentration (Robinson, 1983).

CEs of oligotrophic regions are characterized by a typical phytoplankton composition. Indeed, in the Bay of Biscay offshore waters (north of Spain), diatoms appeared almost entirely confined to the centre of cold core eddies and highest concentrations of cyanobacteria were located in the surrounding oligotrophic waters (e.g., Rodriguez et al., 2003). The same pattern has been found in oligotrophic offshore waters of Hawaii, where diatoms represented ~85% of photosynthetic biomass in the center of a CE (Brown et al., 2008). In the same region, Vaillancourt et al., (2003) determined that photosynthetic eukaryotes (i.e., diatoms) were significantly more abundant inside cold core eddies than outside, while cyanobacteria and smaller phytoplankton were more abundant outside.

All these studies underline that the physical and chemical environment that characterizes offshore CEs of oligotrophic oceans, drives the accumulation of relatively large phytoplankton taxa, while small phytoplankton taxa including cyanobacteria are characteristic of the surrounding waters and the center of ACEs (Olaizola et al., 1993; Vaillancourt et al., 2003; Rodriguez et al., 2003; Brown et al., 2008). ACEs and CEs off East Australia, as other eddies of similar oligotrophic systems, are characterized by different conditions (temperature, light, mixed layer and nutrients concentration) and it is reasonable to hypothesize that different phytoplankton communities can characterize these two environments in the East Australia region as well.

1.2.3 Climate change impacts to the ocean

To date, the global phenomenon of climate change, which includes ocean warming (Bindoff et al., 2007) and acidification (Doney et al., 2009) is likely related to the rising atmospheric CO_2 produced by the use of fossil fuels (Doney et al., 2012). These changes are having many different impacts, from changing weather patterns, sea level rise, increasing stratification, melting of sea-ice, changing ocean circulation and shifts in marine species distributions (Hobday et al., 2011; Doney et al., 2012). In particular, changes in phytoplankton concentration, composition and

distribution can significantly affect ecosystem functions such as primary productivity, export production, CO_2 uptake and sequestration (Dutkiewicz et al., 2009; Doney et al., 2012; Vallina et al., 2014).

The western boundary currents of the Southern Hemisphere (i.e Agulhas Current, Brazil Current and East Australian Current) are particularly affected by climate change, showing the greatest rate of surface warming over the twentieth century (Wu et al., 2012). In eastern Australia, projections for climate change show variations in water circulation that include a strengthening of the EAC (Cai et al., 2005). In particular, the change predicted for the EAC by 2085 is greater than in the other subtropical gyres, with its transport increasing up to 20% (Cai et al., 2005). Time series analyses of temperature, salinity, dissolved oxygen, nitrate, phosphate and silicate, from 1944 to 2002 are consistent with climate change projections, showing an increased EAC southward penetration (Ridgway, 2007). Furthermore, a recent modelling study shows that this predicted intensification of the EAC will cause an increase in eddy activity (Matear et al., 2013). In the same region, an eddy-resolving model forecast to 2060 shows a 10% increase in primary production, related to the projected increase of eddy activity that introduces nutrients into the upper ocean (Matear et al., 2013).

While these projections suggest the importance of mesoscale features (i.e., eddies) as a mechanism to stimulate regional production, the phytoplankton concentration and composition in CE and ACE off East Australia still need to be investigated. Biogeochemical models represent a powerful tool to explore phytoplankton dynamics in relation with these mesoscale features (e.g., Matear et al., 2013). Furthermore, biogeochemical models able to reproduce CE and ACE phytoplankton dynamics could provide an improved resolution of primary productivity estimates.

1.3 Modelling phytoplankton dynamics

1.3.1 Biogeochemical modelling approaches

Modelling is a tool that allows scientists to carry out, in just few

minutes, experiments that in the real world could last for many weeks, months or even years. Models do not represent reality perfectly, but they can be considered a simplification of it. For this reason, model simulations are a representation of the real world, not a fixed outcome. Complex mathematical models can be used to simulate phytoplankton diversity and dynamics, to explore different scenarios, also in relationship with biogeochemical cycles (Fennel and Neumann, 2004). Modelling phytoplankton dynamics ranges in complexity from a single phytoplankton compartment to multi-phytoplankton compartments that are separated into different functional groups and size (Fennel and Neumann, 2004). The choice of complexity is driven by the information desired from the model simulation and the available information to constrain the system.

A marine biogeochemical model can be defined as a mathematical tool that helps to understand, conceptualize and predict marine environmental processes using a series of differential equations (Fennel and Neumann, 2004). A classic, basic example is represented by the NPZD conceptual model (Nutrients, Phytoplankton, Zooplankton, Detritus) (Figure 1.3) (e.g., Fasham et al., 1990).

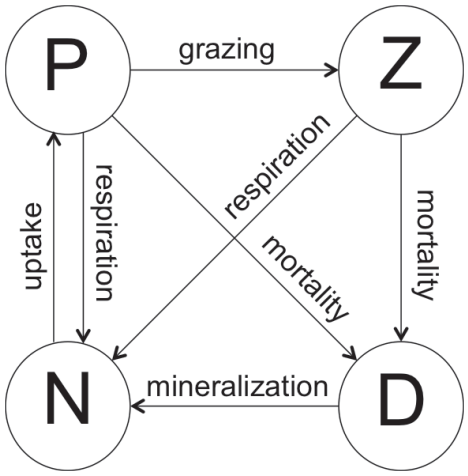

Figure 1.3: Conceptual diagram of a NPZD biogeochemical model structure.

Every compartment in Figure 1.3 represents an element in the model: N (nutrients), P (phytoplankton), Z (zooplankton) and D (detritus); each box represents a state variable. The variation of the state variable value can be expressed as the sum of “sources and sinks”, which are

represented by the arrows. In other words, every arrow represents a differential equation and the arrow direction indicates if this equation represents a source or a sink for every compartment. Starting from this simple conceptual model, many variations can be applied to set up a model that represents a marine ecosystem and an elemental cycle (Fennel and Neumann, 2004). Different phytoplankton types can be introduced by adding compartments (boxes) and links (arrows), as well as multiple nutrients or multiple zooplankton classes. Physical events such as mixing or upwelling can be inserted as forcing functions, to drive the system and hence the output of the selected state variable. The purpose of adding complexity is to achieve a better representation of the "real world system". On the other hand, complexity is not always a benefit and it has been shown that a simple and a complex model can lead to similar outputs (Friedrichs et al., 2007).

The classic and most common approach to model phytoplankton-mediated processes consists in resolving a single generic phytoplankton class, usually represented by Chl-*a* (Follows and Dutkiewicz, 2011). However, using only one phytoplankton class as a state variable limits the amount of information that can be extracted from the model (Finkel et al., 2009, Follows and Dutkiewicz, 2011). Biogeochemical models are increasingly considering phytoplankton composition to characterize biogeochemical cycles in the contemporary and future ocean (Finkel et al., 2009, Follows and Dutkiewicz, 2011). Unfortunately, when adding new elements to a system, the complexity levels of the model rise significantly: numbers of parameters and links between processes increase, resulting in an error accumulation that can lead to a decrease in the predictive power (Follows and Dutkiewicz, 2011). Increasing complexity also relies on having observations with which to help constrain the model. On the other hand, this new level of complexity is necessary to better understand biogeochemical cycles and their links with phytoplankton dynamics.

To model multi-phytoplankton dynamics, one strategy is to use phytoplankton functional groups (e.g., Iglesias-Rodríguez et al., 2002,

Becker et al., 2009). This approach is based on the concept of considering many phytoplankton species with similar biogeochemical function as part of the same functional group (Follows and Dutkiewicz, 2011). The addition of phytoplankton such as coccolithophores, diatoms and diazotrophs can give the model output more information about C, Si and N cycles in particular. Unfortunately, this approach does not consider differences in maximum growth rate, cell size, optimum light and mortality, that characterize every phytoplankton species incorporated into a phytoplankton functional group; these differences can lead to different phytoplankton dynamics and ecological strategies (Follows and Dutkiewicz, 2011). Furthermore, it has already been demonstrated that additional functional groups and system complexity may not always lead to a more powerful or believable model outcome (Anderson 2005, Friedrichs et al. 2007, Thingstad et al. 2010).

A different modelling approach utilizes phytoplankton diversity instead of functional groups (Follows and Dutkiewicz, 2011). This approach is based on the concept that “everything is everywhere but the environment selects” (Baas Becking, 1934). In this approach, phytoplankton taxa (i.e., phenotypes or taxonomic units) characterized by different physiology and ecology are initialized in the model and a minimum cell concentration is imposed for every class (Bruggeman and Kooijman, 2007). Environmental conditions vary in the model due to seasonal changes in temperature, nutrient limitation, light and grazing, and lead to selection of the most suitable phytoplankton to dominate the system (Follows and Dutkiewicz, 2011). At the same time, phytoplankton distribution shapes the local environment through feedback processes (e.g., Sunda and Huntsman, 1992; Timmermann and Jin, 2002; Sonntag and Hense, 2011). Similar to the functional group approach, incorporating phytoplankton taxa is not always useful for the question being asked (Salihoglu and Hofmann, 2007). Furthermore, the computational costs of inserting additional information in these models is significantly higher than the phytoplankton functional group models (Follows and Dutkiewicz,

2011).

A third “multi-box” approach consists of using phytoplankton cell size as the fulcrum of the model. This approach takes advantage of the well described relationships between cell size, metabolic rate (growth, nutrient uptake, respiration…) and biophysical processes (sinking rate, light absorption…). Different size classes of phytoplankton are initialized in the model and their dynamics are driven by ecosystem properties as light, temperature and mixing rate (e.g., Moloney and Field, 1991; Baird and Suthers, 2007; Stock et al., 2008). For example, thanks to the higher surface area to volume ratio of smaller size classes, which make nutrient uptake very efficient, picophytoplankton are favored in oligotrophic waters, rather than larger phytoplankton taxa (Raven, 1998). There are however disadvantages to this approach. Phytoplankton cell size is usually related with physiological rate and ecological function but there are “exceptions” that do not follow scaling relationships (Marañón, 2015). Dinoflagellates, for instance, have lower maximum growth rates than other phytoplankton with similar cell size (Follows and Dutkiewicz, 2011). Also diazotrophs usually grow slower than other phytoplankton cells with the same size (Follows and Dutkiewicz, 2011).

Although marine biogeochemical models represent a simplification of reality, their simulation outputs make it possible to gain insights into phytoplankton dynamics. The choice of representing phytoplankton as a single or multiple box, or between multiple functional groups, species and sizes depends on the scientific question as well as the amount of available information to constrain and calibrate the system.

1.3.2 Data assimilation: calibrating biogeochemical models

Data assimilation (DA) is a process that combines observations and models to estimate variables, providing more consistent simulations. Data assimilation can be performed to improve the predictive power of models, an approach particularly used for physical ocean modelling (e.g., Oke et al., 2008). In this case, parameter values are fixed and the model state is

updated to fit the observations and produce a more realistic evolution of the actual ocean state (e.g., Natvik and Evensen, 2003). In biogeochemical modelling, DA is mainly applied to optimize parameters and correct for model errors and non-linear processes (e.g., Laiolo et al. 2016). In this case, the model parameters are optimized to determine a range of acceptable solutions, that fit the data constraints (i.e., observations). The optimization of parameters usually involves three main steps: (1) running the model forward in time, (2) comparing simulation results with the observations through a cost function, (3) modifying the value of parameters accordingly until the best representation of the data fit is obtained.

State variable dynamics are directly related to the values of model parameters; a poor fit between simulations and observations can be the consequence of a wrong parameters value choice. The DA process can reduce the uncertainties associated with a parameter's value, reducing the spread of acceptable solutions, thus giving an improved simulation of the natural environment.

Observations useful to perform DA and optimize parameters value of marine biogeochemical models can be obtained from *in situ* or remotely sensed measurements. Although *in situ* observations can provide higher-quality data of physico-chemical and biological variables, they are usually limited by sparse coverage in time and space and the expense of collection and subsequent analyses of samples. Because of these reasons, such data are rarely used to calibrate marine biogeochemical models (e.g., Matear, 1995; Laiolo et al., 2014). On the other hand, phytoplankton dynamics in the surface ocean can be derived from remote sensing measurements in the form of ocean colour products such as Chl-*a*. Satellite data is commonly used to calibrate marine biogeochemical models, optimizing their biological parameters (e.g., Hemmings et al., 2003; Laiolo et al., 2016). These data are derived from the scattering and absorption properties of the water and all particulates in the water, including phytoplankton cells.

1.3.3 Satellite remote sensing of ocean colour

Photons that penetrate the ocean can be either absorbed or scattered. While scattering redirects the angle of the photon path, absorption removes the photons permanently from the path (Dickey et al., 2006). This latter process is fundamental for phytoplankton photosynthesis, allowing phytoplankton to synthesize organic compounds from inorganic CO_2. Together, scattering and absorption define the inherent optical properties (IOPs) of the water column, which are independent from the ambient light field. On the other hand, the apparent optical properties (AOPs) of the water column are derived from radiometric quantities such as the water-leaving radiance, which depend on both the medium (i.e., the IOPs) and the ambient light (Dickey et al., 2006). The water-leaving radiance is a function of incident solar irradiance, scattering and absorption properties of the water, as well as the dissolved and particulate matter in the water, including organic and inorganic components (e.g., Cherukuru et al., 2016).

Specifically, remote sensors are not able to measure directly Chl-*a* concentrations or water-leaving radiances; they can measure instead the total atmospheric radiance and the ocean-backscattered signal. The total atmospheric radiance, measured at the satellite sensor, comprises the sum of surface-reflected radiance, water-leaving radiance and atmospheric radiance (Robinson, 2004). Once the total radiance is measured, corrections are applied to remove atmospheric and surface-reflected radiance components from the signal (e.g., Schroeder et al., 2007), obtaining the water-leaving radiance. Then, the ratio between water-leaving radiance and downwelling irradiance defines the remote-sensing reflectance. Finally, with the use of algorithms derived from statistical relationships between *in situ* observations and remote-sensing reflectance, it is possible to obtain an estimation of the surface ocean Chl-*a* concentration (i.e., final Chl-*a* concentration product, Figure 1.4).

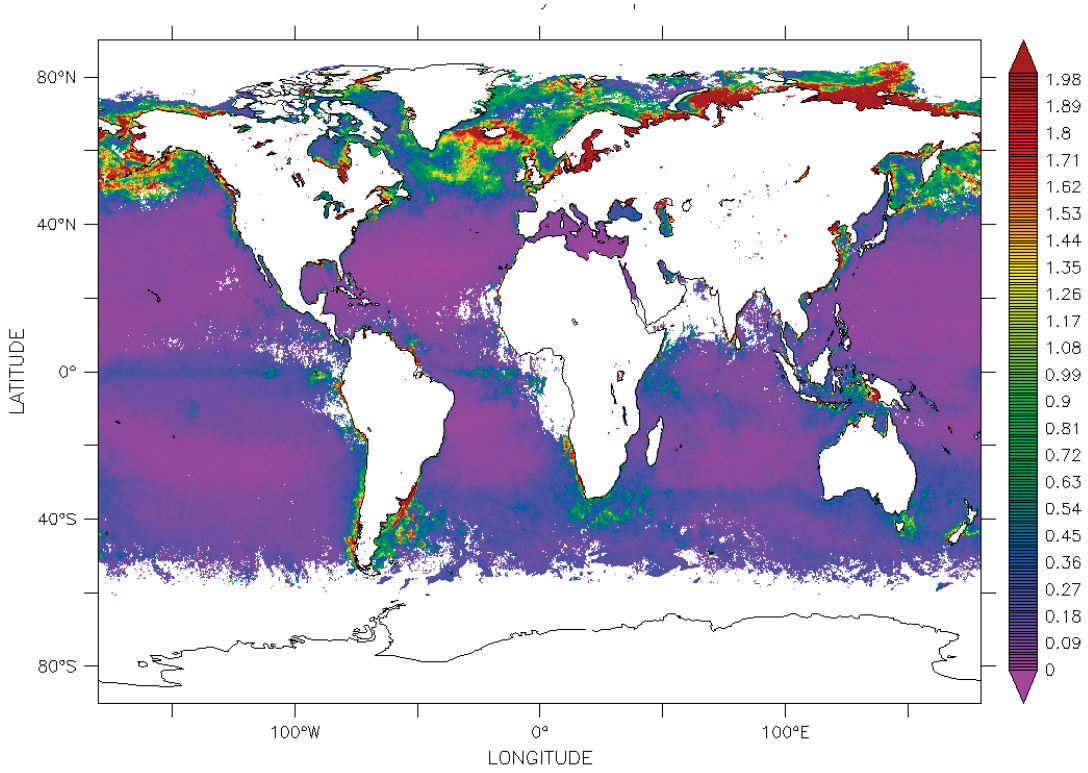

Figure 1.4: Global surface Chl-a concentration (mg m^{-3}) from GlobColour climatology (August 2014) computed from 8-day composite, 4-km resolution product.

Due to their spatial and temporal resolution and their easy access, ocean color observations are particularly appealing for assessing model simulations, validating models and performing DA analyses. On the other hand, cloud cover affects the view of satellite sensors and this results in a lower number or measurements that could affect the reliability of climatologies built on an ocean color dataset. Furthemore, it is essential to consider the complexity and variability associated with ocean color data (Babin et al., 2003; Oubelkheir et al., 2006). In open ocean waters (i.e., Case I waters), the complexity and variability of the bio-optical properties result in a ~5% uncertainity for water-leaving radiance and ~35% for the corresponding Chl-*a* product (McClain, 2009). In coastal waters (i.e., Case II waters) a significant error increase has been shown (Odermatt et al., 2012). Offshore waters of eastern Australia are classified as Case I waters; hence it seems appropriate to use remotely sensed data to investigate phytoplankton dynamics.

Marine biogeochemical models are a key factor in advancing our understanding of phytoplankton dynamics. Remotely sensed data can be used to calibrate parameters value of biogeochemical models (e.g., Hemmings et al., 2003), to estimate surface ocean circulation patterns (e.g., Barton, 2002; Pegau et al., 2002) or phytoplankton primary production (e.g., Longhurst et al., 1995; Carr et al., 2006). The goal of this PhD was to integrate remotely sensed DA with *in situ* observations and experiments, to advance the knowledge about the physical-biological interactions in eastern Australian waters and to reduce the uncertainty of current marine biogeochemical models.

1.4 Objectives of this thesis

Specifically, the goals of this thesis are to:

- Characterise phytoplankton concentration and composition in CE and ACE off East Australia, identifying the key drivers of their seasonal dynamics. This objective was addressed in Chapter 2 of this thesis, integrating *in situ* manipulation experiments and biogeochemical model simulations.

- Investigate the information content of *in situ* Chl-*a* and remotely sensed Chl-*a* product in relation with the optimisation of marine biogeochemical model parameters value. To address this goal, theoretical experiments were performed through a biogeochemical model coupled with a bio-optical model in the 3rd Chapter of this thesis.

- Assess the ocean colour product consistency in eastern Australian waters and its relationship with phytoplankton size structure. This aim was addressed in Chapter 4, comparing *in situ* size fractionated Chl-*a* with the corresponded remotely-sensed Chl-*a* product.

Results presented in this thesis contribute toward understanding the phytoplankton dynamics and size distribution in East Australian waters. Specifically, Chapter 2 describes phytoplankton dynamics in CE and ACE off East Australian waters, confirming the relation between seasonal increases in Chl-*a* concentration and increases in large-sized phytoplankton cells. Moreover, the biogeochemical model parameter values optimised in Chapter 2 can be used to improve primary productivity estimates in the region, considering two distinct size-dependent phytoplankton classes. Furthermore, thanks to a biogeochemical model that incorporates the optical characteristics of the state variables it was possible to explore the links between remotely sensed observations and quantities simulated by biogeochemical models. Specifically, results presented in Chapters 3 and 4 have significant implications for the assimilation of ocean colour products. First, they showed a relationship between the remotely-sensed Chl-*a* underestimation and the amount of Chl-*a* associated with large-sized phytoplankton. Second, they suggested that a combination of *in situ* and remotely-sensed observations could provide distinct information about the phytoplankton size structure. While there was a regional focus of the three main chapters of this thesis (i.e., Chapter 2, 3 and 4) the findings have a significant impact for satellite imagery interpretation in the selected area of study as well as other eddy-impacted offshore regions of the global ocean. Finally, Chapter 5 summarises the key results that have arisen from the thesis and discusses the potential directions for future research.

CHAPTER 2

Key drivers of seasonal plankton dynamics in cyclonic and anticyclonic eddies off East Australia

Leonardo Laiolo[1, 2], Allison S. McInnes[1], Richard Matear[2], Martina A. Doblin[1]

[1]Plant Functional Biology and Climate Change Cluster, University of Technology Sydney, 8-15 Broadway, Ultimo, NSW, 2007, Australia
[2]CSIRO Oceans and Atmosphere, Hobart, 3-4 Castray Esplanade, TAS, 7004, Australia

"This Chapter has been previously published in *Frontiers in Marine Science* on the 16th August 2016"

Citation:

Laiolo L., McInnes A. S., Matear R. J., Doblin M. A., 2016. Key Drivers of Seasonal Plankton Dynamics in Cyclonic and Anticyclonic Eddies off East Australia. Frontiers in Marine Science, 3: 155. doi:10.3389/fmars.2016.00155

2.1 Abstract

Mesoscale eddies in the south west Pacific region are prominent ocean features that represent distinctive environments for phytoplankton. Here we examine the seasonal plankton dynamics associated with averaged cyclonic and anticyclonic eddies (CE and ACE, respectively) off eastern Australia. We do this through building seasonal climatologies of mixed layer depth and surface chlorophyll-a for both CE and ACE by combining remotely sensed sea surface height (TOPEX/Poseidon, Envisat, Jason-1, and OSTM/Jason-2), remotely sensed ocean colour (GlobColour) and *in situ* profiles of temperature, salinity and pressure from Argo floats. Using the CE and ACE seasonal climatologies, we assimilate the surface chlorophyll-a data into both a single (WOMBAT), and multi-phytoplankton class (EMS) biogeochemical model to investigate the level of complexity required to simulate the phytoplankton chlorophyll-a. For the two eddy types, the data assimilation showed both biogeochemical models only needed one set of parameters to represent phytoplankton but needed different parameters for zooplankton. To assess the simulated phytoplankton behavior we compared EMS model simulations with a ship-based experiment that involved incubating a winter phytoplankton community sampled from below the mixed layer under ambient and two higher light intensities with and without nutrient enrichment. By the end of the 5-day field experiment, large diatom abundance was four times greater in all treatments compared to the initial community, with a corresponding decline in pico-cyanobacteria. The experimental results were consistent with the simulated behavior in CE and ACE, where the seasonal deepening of the mixed layer during winter produced a rapid increase in large phytoplankton. Our model simulations suggest that CE off East Australia are not only characterized by a higher chlorophyll-a concentration compared to ACE, but also by a higher concentration of large phytoplankton (i.e., diatoms) due to the shallower CE mixed layer. The model simulations also suggest the zooplankton community is different in the two eddy types and this behavior needs further

investigation.

2.2 Introduction

Mesoscale eddies play crucial roles in ocean circulation and dynamics, stimulating phytoplankton growth and enhancing the global primary production by ~20% (Falkowski et al., 1991; McWilliams, 2008). Usually, eddies occur where there are strong currents and oceanic fronts (Robinson, 1983) and hence are a common feature of western boundary currents (Chelton et al., 2011). The direction and resulting temperature of an eddy circulation can be categorized as either cyclonic cold core or anticyclonic warm-core (Robinson, 1983). The cyclonic eddies (CE) are associated with low sea level anomalies, doming of the isopycnals and shoaling of the nutricline (Falkowski et al., 1991; McGillicuddy, 2015). The shoaling of the nutricline helps supply nutrient-rich waters to the euphotic zone when mixed layer depth (MLD) undergoes seasonal deepening (Dufois et al., 2014; McGillicuddy, 2015) and, thereby stimulating phytoplankton growth (Jenkins, 1988; Falkowski et al., 1991; McGillicuddy and Robinson, 1997). In contrast, anticyclonic eddies (ACE) are associated with high sea level anomalies, depression of the isopycnals and deepening of the nutricline (McGillicuddy, 2015). The MLD of ACEs is generally deeper than CEs (Dufois et al., 2014) and this changes the supply of nutrients to the euphotic zone when the eddy undergoes seasonal deepening of the MLD with additional impacts to light levels (Dufois et al., 2014; McGillicuddy, 2015). While representing different physical and nutrient conditions, the characteristics of CE and ACE can also differ because of differences in how these eddies form. The process called “eddy trapping” (McGillicuddy, 2015) was used to describe how composition of the water trapped in an eddy depends on the process of eddy formation as well as on the local gradients in physical, chemical, and biological properties. One example is the formation of eddies off Western Australian where the Leeuwin Current generates ACE initialized with high Chl-a derived from the coastal water (Moore et al., 2007).

CE and ACE represent two distinct environments because of differences in their physical properties and in the physical processes that form them, which can lead to different phytoplankton abundance, biomass and composition (Angel and Fasham, 1983; Arístegui et al., 1997; Arístegui and Montero, 2005; Moore et al., 2007; Everett et al., 2012; Table 2.1). In addition, sub-mesoscale processes can affect phytoplankton dynamics in mesoscale eddies (Klein and Lapeyre, 2009); in particular small-scale upwellings and downwellings seem to have a significant impact on phytoplankton subduction and primary production (Levy et al., 2001).

Table 2.1: Schematic representation of main physical and biological differences between CE and ACE off East Australia.

	Eddy type	
Eddy properties	ACE (warm core)	CE (cold core)
Direction of circulation	Counter clockwise	Clockwise
Vertical structure	Downwelling	Upwelling
Sea surface height anomalies	Positive	Negative
Dissolved nutrient concentration	Lower	Higher
Mixed layer depth	Deeper	Shallower
Chlorophyll a concentration	Lower	Higher

Multiple processes can impact phytoplankton composition and growth in mesoscale eddies. Oceanographic studies show that large photosynthetic eukaryotes (>3 μm, diatoms in particular) appear confined to the center of CE (Rodriguez et al., 2003; Brown et al., 2008). In comparison, higher concentrations of cyanobacteria (<3 μm) are located in the surrounding oligotrophic waters (Olaizola et al., 1993; Rodriguez et al., 2003; Vaillancourt et al., 2003; Brown et al., 2008) and in adjacent ACEs (e.g., Haury, 1984; Huang et al., 2010). However, we still have very limited understanding about the phytoplankton communities that characterize eddy environments because they remain largely under-sampled.

Phytoplankton are limited by two primary resources in marine

environments: light and nutrients (Behrenfeld and Boss, 2014). Eddies represent an interesting resource paradox because, through physical processes, they influence light and nutrient concentrations simultaneously. Indeed, the seasonal deepening of the MLD can bring nutrient-rich water from depth into the euphotic zone but decrease the total photon flux to cells. Due to the differing nutrient requirements of phytoplankton, the water mass below the MLD could therefore play an important role in determining eddy phytoplankton concentration and composition (Dufois et al., 2016; Bibby and Moore, 2011). Furthermore, the shallower MLD that characterizes CE leads to higher light levels in the surface mixed layer, while ACE have lower light levels (Tilburg et al., 2002). Understanding what the primary driver of phytoplankton dynamics in these two environments is an important question, given the uncertainty in regional predictions of primary production under projected ocean change (Bopp et al., 2013).

Floristic shifts in phytoplankton at a regional level will play an important role in determining the marine ecosystem response to future climate change (Boyd and Doney, 2002). Representation of phytoplankton in biogeochemical models ranges in complexity from a single phytoplankton compartment to multi-phytoplankton compartments that can be separated into different functional groups and/or sizes (Fennel and Neumann, 2004). To advance knowledge about the physical-biological interactions in mesoscale features and reduce uncertainty, McGillicuddy (2015) suggests coupling *in situ* observations, remote sensing, and modeling. Here, we follow such an inter-disciplinary approach.

Our study area is eastern Australia (Fig. 2.1), a region strongly influenced by the southward flowing Eastern Australian Current (EAC), which forms both CE and ACE (Hamon, 1965; Tranter et al., 1986). EAC waters are low in nutrients and any subsurface nutrients are rarely upwelled to the euphotic zone (Oke and Griffin, 2011). However, increases in phytoplankton biomass occur in this region as a response to occasional upwelling-favorable wind events, the separation of the EAC from the shelf

or the formation of CE (Tranter et al., 1986; Cresswell, 1994; Roughan and Middleton, 2002). Both eddy types form from meanders in the EAC and move into adjacent water with different physical, chemical and biological characteristics (Lochte and Pfannkuche, 1987).

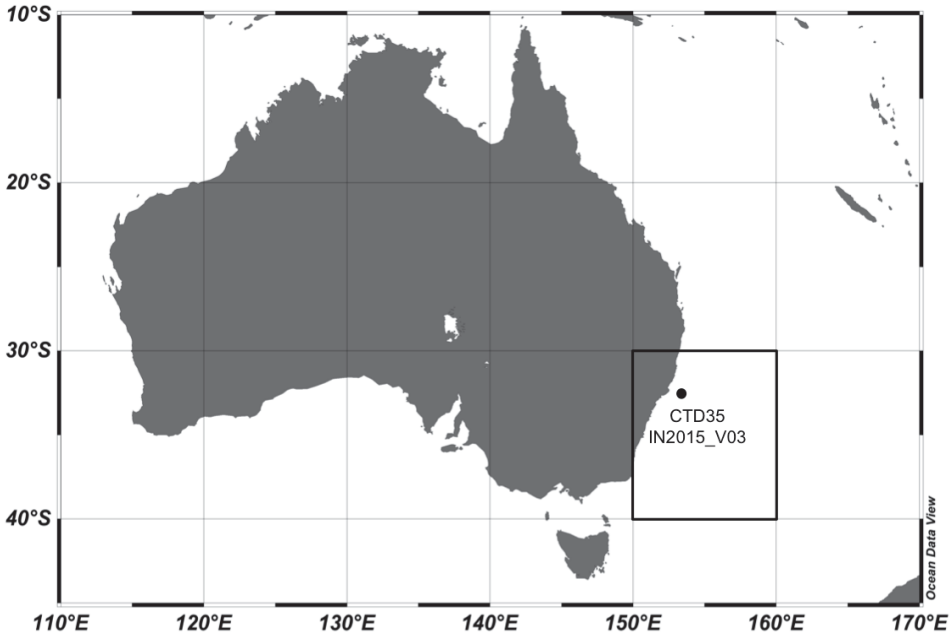

Figure 2.1: Map showing the study area, including the location of the where water was collected for the shipboard manipulation experiment (CTD35 IN2015_V03).

Here we characterize phytoplankton dynamics in CE and ACE off East Australia using a combination of *in situ* observations, remote sensing, and modeling. We firstly explore the level of phytoplankton complexity required to estimate the phytoplankton chlorophyll-a (Chl-a) for eddies in the East Australian system, using a single (WOMBAT) and a multi-phytoplankton class model (EMS). Models were used to simulate the observed Chl-a concentrations obtained from satellites (MERIS, SeaWiFS and MODIS-Aqua). Shifts in phytoplankton composition and size distribution were also examined using a manipulative ship-board experiment and comparing outcomes with simulations. Results show that CE and ACE off eastern Australia are not only characterized by a different Chl-a concentration but also by different phytoplankton composition. Both models suggest these differences are related to distinct zooplankton

dynamics. Furthermore, simulation results are consistent with the ship-based experiment, highlighting the important role of mixed layer depth and irradiance in driving eddy phytoplankton dynamics off eastern Australia.

2.3 Materials and Methods

2.3.1 Study region and location of voyage experiment

The eastern Australian ocean region is significant for Australia's economy and marine ecology (Hobday and Hartmann, 2006). This area is adjacent to capital cities, major shipping lanes and regions of environmental significance (e.g., Great Barrier Reef World Heritage area). Pelagic offshore fisheries, including the valuable Bluefin tuna, are strongly influenced by the Eastern Australian Current (EAC), the major western boundary current of the South Pacific sub-tropical gyre (Mata et al., 2000; Ridgway and Dunn, 2003; Hobday and Hartmann, 2006; Brieva et al., 2015). Furthermore, the ocean circulation of this region has a crucial role in removing heat from the tropics and releasing it to the mid-latitude atmosphere (Roemmich et al., 2005). In this region, climate change is projected to increase eddy activity and hence primary productivity (Matear et al., 2013). Due to its importance, the area selected for this study is located between 30°S and 40°S, and 150°E and160°E (Fig. 2.1).

2.3.2 Description of biogeochemical models

To explore the level of complexity required to represent seasonal phytoplankton dynamics associated with mean MLD variations in CE and ACE within the domain, two biogeochemical models were used. The first model, "WOMBAT" (Whole Ocean Model of Biogeochemistry And Trophic-dynamics) is a Nutrient, Phytoplankton, Zooplankton and Detritus (NPZD) model, with one zooplankton and one phytoplankton class (i.e., total Chl-a concentration) characterized by a fixed C:Chl-a ratio (Kidston et al., 2011; Fig. 2.2A). WOMBAT has a total of 14 different parameters. The second NPZD biogeochemical model, Environmental Modelling Suite (EMS), is a more complex size-dependent model characterized by a total of 104

parameters (CSIRO Coastal Environmental Modelling Team, 2014). EMS has been developed to model coupled physical, chemical and biological processes in marine and estuarine environments (CSIRO Coastal Environmental Modelling Team, 2014) and can be implemented in a wide range of configurations. We set it up with two phytoplankton and two zooplankton classes, characterized by different sizes, growth, mortality, and grazing rates (zooplankton only) (Fig. 2.2B). The two EMS phytoplankton classes can adjust their C:Chl-a ratio daily, to attain the ratio that allows optimal phytoplankton growth (Baird et al., 2013).

Both biogeochemical models are configured as 0D to represent a well mixed MLD with a prescribed seasonal cycle of nutrient levels below the MLD. Phytoplankton and zooplankton concentrations are uniformly distributed in the MLD. The MLD climatology was the only environmental factor differing between the CE and ACE systems. The time series of temperature in the MLD and nutrients below the MLD from the CSIRO Atlas of Regional Seas dataset (CARS; http://www.marine.csiro.au/~dunn/cars2009/; Ridgway et al. 2002) were used in the simulations, with no distinction between the eddy environments. The surface incident irradiance comes from seasonal climatology of the region (Large and Yeager, 2008). Because other physical phenomena, such as upwelling or downwelling were not explicitly represented, the only supply of nutrients to the MLD occurs with the deepening of the MLD (i.e., when the MLD is shoaling there is no new supply of nutrients to the MLD). In both models, when the MLD is deepening from a time step to the next one, the nutrient concentration (calculated from the nitrate dataset below the MLD obtained from CARS; Ridgway et al. 2002) is added to the MLD. Following Matear (1995) approach the nutrients concentration added in the MLD is calculated as:

$$N_{t+1} = \frac{\delta h \cdot N_b + h \cdot N_m}{h + \delta h} \quad (1)$$

where h represents the MLD, δh the difference in the MLD between the time t and t+1, N_b represent the nutrient concentration below the MLD, N_m the nutrient concentration in the MLD.

To evaluate the sensitivity of the model to higher-frequency variations in the MLD, we added Gaussian random noise to the CE and ACE daily MLD dataset, where the standard deviation of the random noise was estimated from the standard error of the CE and ACE MLDs (i.e., ACE 1.3m; CE 1.2m).

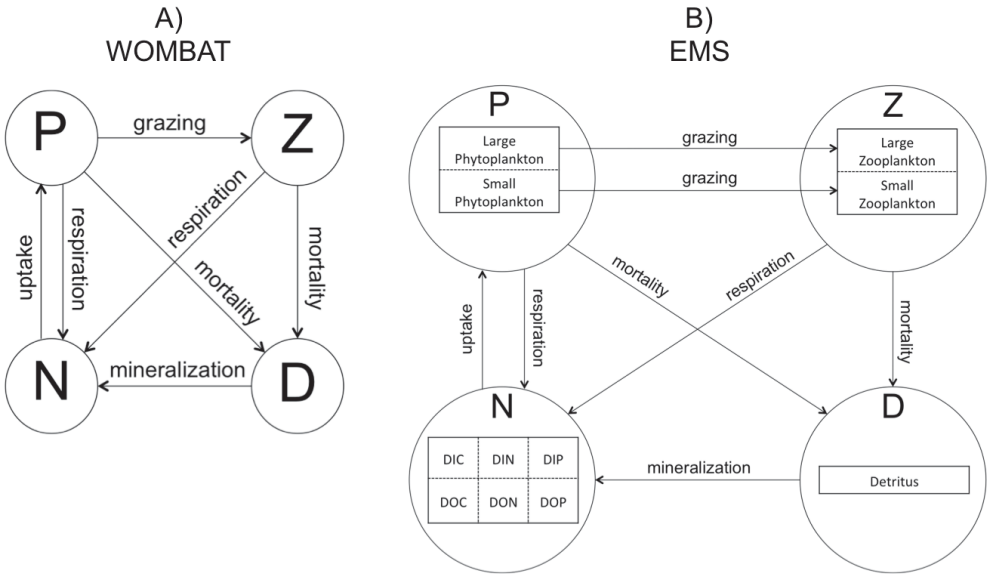

Figure 2.2: Structure of biogeochemical models used in this study. Arrows represent interactions and links between model compartments. A) WOMBAT (Whole Ocean Model of Biogeochemistry And Trophic-dynamics), which has one phytoplankton (P) and one zooplankton (Z) class, detritus (D) and one nutrient compartment (N). B) EMS (Environmental Modelling Suite), characterized by two phytoplankton (P) and zooplankton (Z) sized-based classes, detritus (D) and one nutrient compartment divided into dissolved inorganic carbon, nitrogen, phosphate (DIC, DIN, DIP) and dissolved organic carbon, nitrogen, phosphate (DOC, DON, DOP).

2.3.3 Input data and implementation to biogeochemical models

Because of their different dynamical balances, ACE and CE can be identified through sea surface height anomalies (SSH) detected by satellites (Lee-Lueng et al., 2010). A 17 year, 8-day composite dataset of SSH anomalies (2 September 1997 to 26 September 2014), was downloaded from AVISO (Delayed-Time Reference Mean Sea-Level Anomaly; http://www.aviso.altimetry.fr/en/data/products/sea-surface-height-products.html). Eddies were identified by prescribing ± 0.2 m SSH anomaly threshold that characterizes ACE and CE, respectively (Pilo et al.

2015). Satellite-derived Chl-a measurements (25 km spatial resolution, 8-day average) were downloaded from GlobColour (an ocean colour product that combines output from MERIS, SeaWIFS and MODIS; http://hermes.acri.fr/index.php?class=archive). Using this kind of product ensures data continuity, improves spatial and temporal coverage and reduces noise (ACRI-ST GlobColour Team et al. 2015). To obtain MLD measurements, Argo data (temperature, salinity, time, pressure, location for every Argo Float) were downloaded from the GODAE (Global Ocean Data Assimilation Experiment; http://www.usgodae.org/cgi-bin/argo_select.pl). The MLD value was defined as the depth where temperature changed by 1°C and density by 0.05 kg m^{-3} from the surface value (Brainerd and Gregg, 1995; de Boyer Montegut et al., 2004; Dong et al., 2008). The climatology of surface water (5m) temperature and nitrate concentration below the MLD was obtained from CARS (Fig. 2.3; Ridgway et al., 2002); while we obtained the irradiance from the seasonal climatology of the downward short wave radiation at the surface of the ocean (Large and Yeager, 2008). Before inputting to the models, all data were filtered to exclude locations shallower than 1000 m, to avoid including data from coastal systems.

The Chl-a and MLD datasets obtained from GlobColour and GODAE were mapped in time and space onto the 8-day averaged CE and ACE SSH fields. Thus, we obtained surface Chl-a concentrations and MLDs for CE and ACE off East Australia occurring from 1 December 2002 to 1 December 2014 in an 8-day averaged dataset (Argo data are not available before 2002 in our domain). Chl-a concentration and MLD were averaged over time periods (n=546) at their original resolution, obtaining a Chl-a and a MLD 8-day averaged seasonal climatology for an idealised CE an ACE of the selected East Australia region (Fig. 2.4). The datasets extracted from CARS (nitrogen, temperature and light) were used in the two biogeochemical models without any distinction between CE and ACE, as the available data from CARS are an average of the whole area of study.

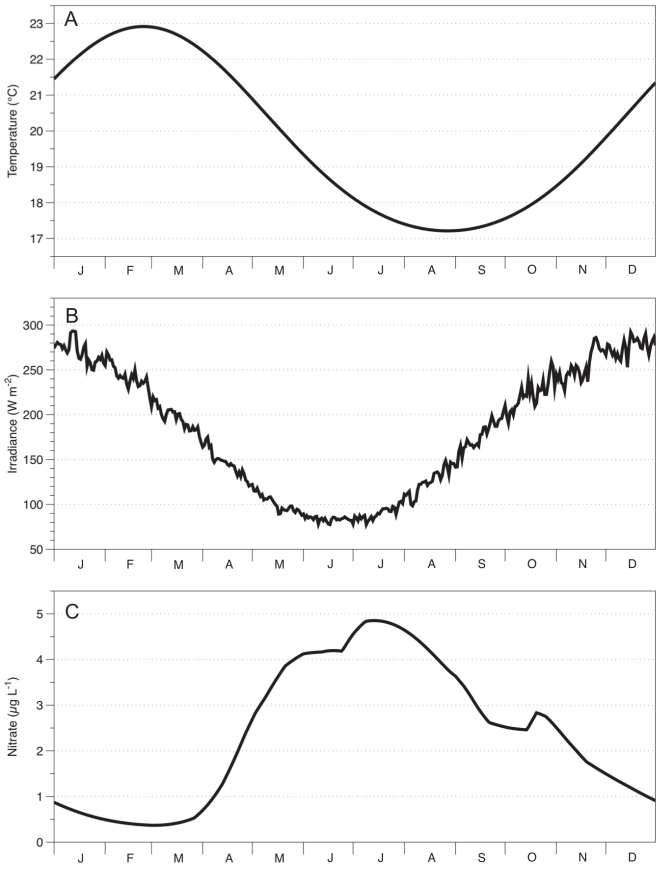

Figure 2.3: Seasonal climatology of the study area (-30°S -40°S, 150°W 160°E) for A) surface temperature; B) surface irradiance; C) nitrate concentration 5 m below seasonal mixed layer depth. Data for A and C come from the CSIRO Atlas of Regional Seas (CARS) available at http://www.marine.csiro.au/~dunn/cars2009/. Data for B comes from seasonal climatology of the downward short wave radiation at the surface of the ocean (Large and Yeager 2008).

2.3.4 Statistical analysis and goodness of the fit

The student-t test was performed to assess statistical differences between the CE and ACE Chl-a climatologies, calculated from the GlobColour dataset. The same approach was applied to the MLD climatology derived from the GODAE Argo dataset. The same test was used to asses if there were statistical differences between the average of the observed and modeled data (i.e., GlobColour Chl-*a* climatology vs

simulated Chl-a), with significance for all tests defined as $p<0.05$.

The goodness of the fit between simulated and observed seasonal climatology of Chl-a was assessed through the Chi-squared misfit (χ^2):

$$\chi^2 = \frac{1}{\nu}\sum_{t=1}^{T}\frac{(Q_m^t - Q_o^t)^2}{\sigma^t} \quad (2)$$

where $\mathrm{Q_m^t}$ is the value of the modeled data at time t and $\mathrm{Q_o^t}$ is the observed value of Chl-a at time t, while σ^t is the variance at time t of the Chl-a climatology. The degrees of freedom are represented by ν:

$$\nu = n_o - n_p \quad (3)$$

where $n_o$is the number of observations, and n_p is the number of fitted parameters. A χ^2 value of approximately 1 represents an acceptable model fit to the observations.

2.3.5 Data assimilation

The observed CE and ACE Chl-a seasonal climatologies were used for the data assimilation, with the purpose of finding parameter sets that best fitted the observations from the two environments (e.g., Matear 1995). The observed Chl-a climatology was assumed to represent the Chl-a concentration in the MLD (i.e., Chl-a uniformly distributed in the MLD). Although this assumption is commonly made, caution needs to be used when interpreting results because a chlorophyll maximum below the surface mixed layer may be not be detected by satellites (e.g., Salleé et al. 2015). To quantify the difference between the simulated and observed Chl-a concentrations we used a cost function (x) defined as:

$$x = \sum_{t=1}^{T}\frac{(\ln \mathrm{Q_m^t} - \ln \mathrm{Q_o^t})^2}{n} \quad (4)$$

where $\mathrm{Q_m^t}$ is the value of the modeled data (total Chl-a concentration) at time t, $\mathrm{Q_o^t}$ is the observed value of Chl-a at time t and n is the number of samples over time. The “ln” transformation was applied to achieve normal distribution of the Chl-a concentrations around the mean seasonal value, thus allowing us to employ statistical parametric methods.

To estimate the optimized parameter set for WOMBAT, we used a simulated annealing algorithm based on the likelihood cost metric (x). This

approach has been previously used in marine ecosystem models and can solve optimization problems with a small number of unknown parameters (e.g., Matear 1995, Kidston et al. 2013). The simulated annealing algorithm was run for 200 iterations to allow the algorithm to converge to the minimum cost function value. The data assimilation was performed with WOMBAT, fitting CE and ACE seasonal climatology independently by allowing 8 parameters that controlled plankton growth to vary. Data assimilation was also used to fit both the environments with one parameter set to determine if the one-phytoplankton class model was sufficiently complex to represent both eddy types.

The data assimilation was then performed with EMS, fitting the CE and ACE Chl-a seasonal climatology independently and fitting both the environments with one parameter set. Because the simulated annealing algorithm computational requirements are large and EMS is a much more complex model than WOMBAT, we estimated EMS parameters with the conjugate-gradient algorithm because it was more computationally efficient. Although this algorithm is sensitive to the choice of the initial model parameters, it is used to solve optimization problems with marine biogeochemical models as well (e.g., Fasham et al., 1995; Evans, 1999). Advantages and disadvantages of using simulated annealing or conjugate-gradient algorithms are discussed in Matear (1995). The phytoplankton size classes in EMS were fixed, with the purpose of representing two distinct phytoplankton types to examine if their abundance was different between CE and ACE: 2 μm diameter for small phytoplankton cells and 40 μm diameter for large phytoplankton cells. With EMS, the data assimilation was allowed to vary 12 parameters – like WOMBAT, they were the parameters controlling plankton growth.

To recognize that there was not one unique solution, rather a range of parameter values could produce acceptable solutions, we show a range of simulated behaviour to reflect the non-uniqueness of the solution. From data assimilation results, only acceptable solutions are shown, which were simulations where both $0 < \chi^2 < 2.5$ and there was no significant

difference between the annual mean simulated and observed Chl-a concentration (with 95% confidence in the equivalence test; Wellek 2010).

2.3.6 Shipboard manipulation experiment

To investigate the potential shift in phytoplankton size and abundance in a CE we examined phytoplankton responses to increased light and nutrients by performing an experiment during an oceanographic research voyage. The experiment was carried out on board the *RV Investigator* (voyage IN2015_V03), with water sampled from a station located in the Eastern Australian Current (32.7° S and 153.6° E), inside the modeling domain (Fig. 2.1). This site was representative of potential source water for eddies, allowing us to evaluate the effect of light and nutrients on the phytoplankton community prior to the seasonal shoaling of the MLD. Water was sampled a few meters below the MLD (~110m, water temperature ~20.9°C) and exposed to increased light and nutrients. Sampled seawater was transferred directly from the CTD-rosette into 15 acid-cleaned 4L polycarbonate vessels. Vessels were sealed, randomly assigned to three light treatments, with half the bottles being amended with inorganic nutrients and the other half remaining unamended, before they were all placed in a deck-board incubator which had continuous flow of surface seawater of approximately 21.5°C. The nutrient enrichment consisted of daily nutrient addition of dissolved inorganic Fe III 0.005 µmol L^{-1}, N as nitrate 1.2 µmol L^{-1}, Si as silicate 1.2 µmol L^{-1}, P as phosphate 0.075 µmol L^{-1}, in Redfield proportion (McAndrew et al., 2007; Ellwood et al., 2013). The experimental treatments included control (CON; ambient light i.e., ~1% incident light, no nutrient amendment), low light (LL; 20% incident light), high light (HL; 40% incident light), low light and nutrients (LL+N), high light and nutrients (HL+N) and were made in triplicate. Incident light was attenuated using shade cloth. Pigment samples for Ultra-High Performance Liquid Chromatography (UPLC) analysis were collected from each bottle at the end of the 5-day experiment, as well as the initial phytoplankton community.

Samples for UPLC analysis were filtered through 25mm glass fibre filters (Whatman GF/F), filters were placed in cryotubes, flash frozen in liquid nitrogen and stored in a -80°C freezer. The pigment extraction was carried out following a modified method used by Van Heukelem and Thomas, (2001). Each filter was placed into an individual 15 mL falcon tube with 1.5 mL of chilled 90% acetone. Each filter was then disrupted using a 40W ultrasonic probe for ~30 s, keeping the tube in ice; then the samples were stored at 4°C overnight. The sample slurry was vortexed for 10 s and clarified by passing through a 0.2µm PTFE 13mm syringe filter before storage in UPLC glass vials, followed by analysis. The dataset obtained from the UPLC analyses was analyzed following Barlow et al., (2004) formulae and Thompson et al. (2011) for the pigment quality control.

2.4 Results

2.4.1 Characterisation of CE and ACE

The physical environment of the CE and ACE show important differences in their seasonal climatologies. For ACE, the MLD is deeper than CE throughout the seasonal cycle (Fig. 2.4A; $n=365$ $p<0.01$, Table 2.2). Conversely, the surface Chl-a concentrations are higher in CE than ACE for most of the year (Fig. 2.4B, $n=365$ $p<0.001$, Table 2.2). Both Chl-a and MLD show the greatest differences between CE and ACE in the May and October period (austral winter/spring); while for the rest of the year (November to April) Chl-a concentrations and MLD are similar (Fig. 2.4).

Table 2.2: Results of the statistical comparisons (student-t test): Chl-a means (observed vs simulated, ACE observed vs CE observed) and MLD means (ACE observed vs CE observed). Results at significance values are highlighted: N.S. indicates not significant ($p > 0.05$); * indicates $p < 0.05$; ** $p < 0.01$; and *** $p < 0.001$. χ^2 indicates the Chi-squared misfit value: the closer χ^2 is to 1, the more accurate the simulation. In this table, "p" and "χ^2" intervals represent the minimum and the maximum value obtained from acceptable solutions. Simulations were considered acceptable when both $p > 0.05$ and $\chi^2 > 2.5$.

		Chl-a concentration	
	ACE observed vs CE observed	ACE model vs ACE observed	CE model vs CE observed
Chl-a climatology	*** p = 0.0002		
MLD climatology	** p = 0.006		
WOMBAT (CE and ACE, 2 distinct parameter set)		N.S. 0.12 < p < 0.49 0.8 < χ^2 < 1.6	N.S. 0.22 < p < 0.42 0.88 < χ^2 < 1.1
WOMBAT (CE and ACE, 1 equal parameter set)		*** p = 0.001 χ^2= 1.8	** p = 0.003 χ^2= 1.7
EMS (CE and ACE, 2 distinct parameter set)		N.S. 0.13 < p < 0.27 1.5 < χ^2 < 2.2	N.S. 0.24 < p < 0.43 0.6 < χ^2 < 1.6
EMS (CE and ACE, 1 equal parameter set)		*** p = 0. 0003 χ^2= 2.8	** p = 0.002 χ^2= 1.9

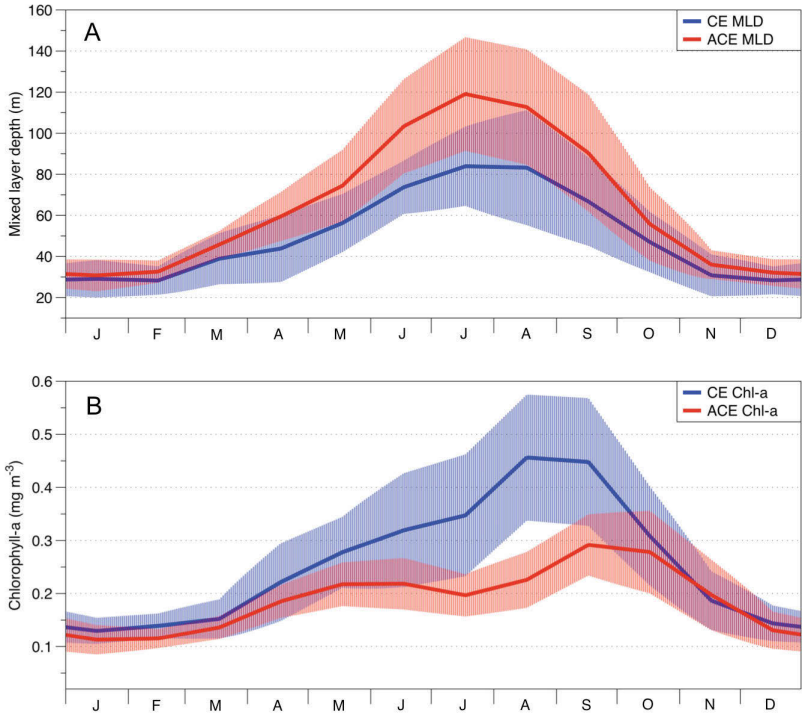

Figure 2.4: Seasonal climatology of cold core CE (solid blue lines) and warm core ACE (solid red lines) eddies for: A) mixed layer depth (MLD) (GODAE); B) surface chlorophyll-a concentration (GlobColour). The light blue and light red areas represent standard deviation for CE and ACE, respectively.

2.4.2 WOMBAT and EMS simulations

Data assimilation to independently determine WOMBAT parameter sets for the CE and ACE environments produced acceptable simulations of the Chl-a seasonal climatology (Fig. 2.5A, 2.5B). Acceptable simulations are demonstrated by the χ^2 values and the non-significant t-student test (ACE $p>0.12$; CE $p>0.22$, 95 % confidence that the two dataset are equivalent), confirming that there are no significant differences between the average of the modeled and observed data (Table 2.2).

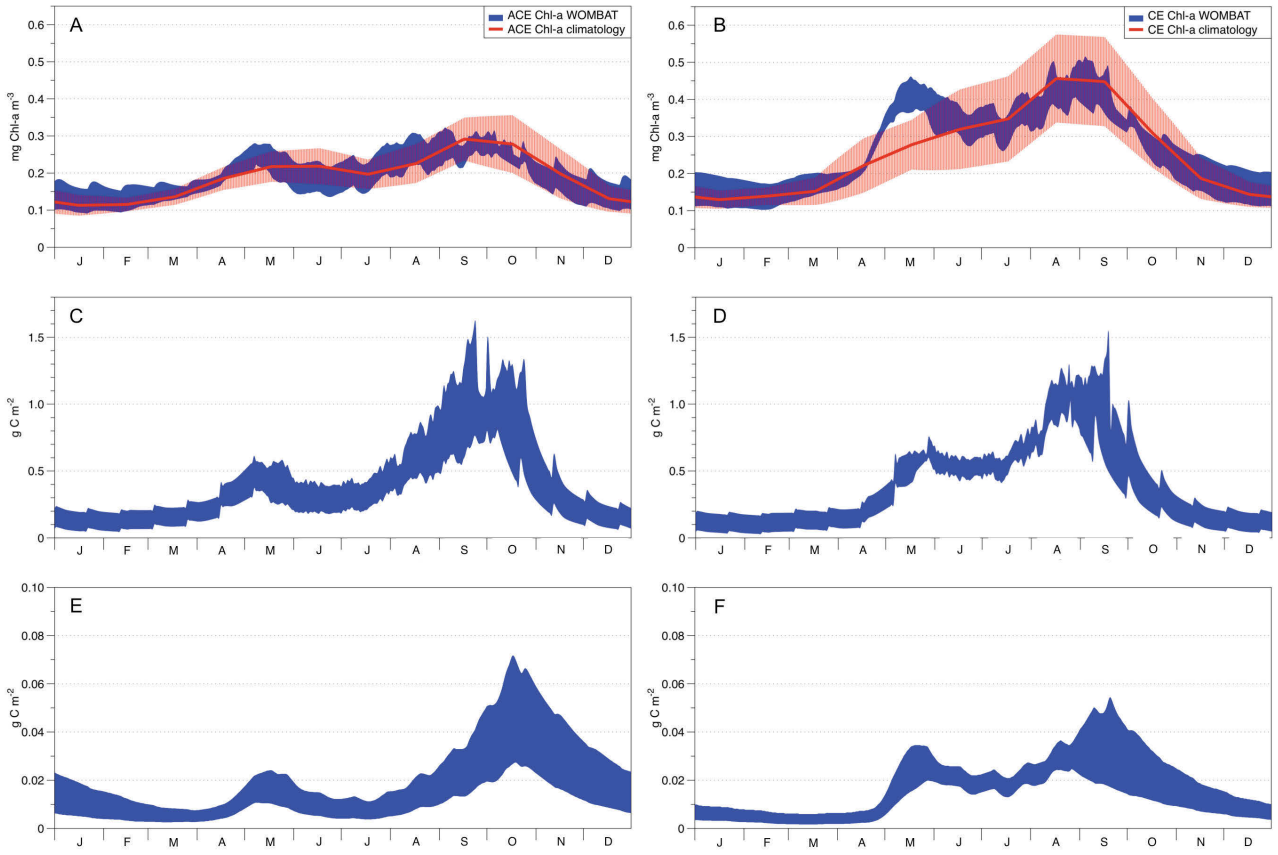

Figure 2.5: WOMBAT's acceptable solutions obtained from data assimilation. Left column shows ACE seasonality and right column CE seasonality. The red solid lines in plots A and B show the Chl-a observed seasonal climatology with the red shading denoting the standard deviation variability. In all remaining plots, the blue areas represent WOMBAT acceptable solutions. Plots C (ACE) and D (CE) represent primary production (g C m^{-2}) while plots E and F represent the zooplankton dynamics for the ACE and CE systems, respectively.

The data assimilation carried out with the single phytoplankton model WOMBAT for the two eddy environments yielded distinct parameter sets (Table 2.3). For acceptable solutions, the main difference between the parameter sets relate to zooplankton (quadratic) mortality, where CE shows ~130 % greater values than ACE (Table 2.3). From the acceptable solutions, we show the primary production and zooplankton concentrations for the two types of eddies (Fig. 2.5C-F). When the data assimilation tries to fit both the environments with a single parameter set there is a significant probability (ACE p=0.003; CE p=0.005, Table 2.2) the annual mean Chl-a differs between the observed and simulated value.

The data assimilation carried out with EMS for the two environments leads to acceptable simulation of Chl-a (Table 2.2), with the simulated annual mean Chl-a consistent with the observed value (ACE p>0.13; CE p>0.24, 95 % confidence that the two dataset are equivalent) (Fig. 2.6, Table 2.2). However, no acceptable solutions were found fitting both the environments with one parameter set (Table 2.2). The data assimilation with EMS produced distinct parameter sets for the CE and ACE environments, with main differences related to the large zooplankton parameters: large zooplankton quadratic mortality rate is ~1.8 times greater in CE and large zooplankton maximum growth rate is ~2.1 times greater in CE (Table 2.4). For the acceptable EMS solutions we show the primary production for large and small phytoplankton and the seasonal evolution of the small and large zooplankton concentrations (Fig. 6C-H). The development of the winter/spring (May – Oct) phytoplankton bloom is driven by increased production of large phytoplankton, that is considerably greater in the CEs than the ACEs.

Simulations carried out to evaluate higher-frequency variations in the MLD (i.e., with the inclusion of random noise), produce plankton dynamics within the range of the acceptable solutions (Fig. 2.5 and Fig. 2.6).

Table 2.3: WOMBAT parameter set for CE and ACE fitted independently, and the optimized parameter set fitting the two environments simultaneously (CE + ACE).

PARAMETER	CE	ACE	CE + ACE	Unit
Photosynthetic efficiency (initial slope of P–I curve)	0.020 ± 0.003	0.024 ± 0.006	0.024	day^{-1} ($W\ m^{-2}$)
Shortwave fraction of photosynthetically active radiation	0.43	0.43	0.43	
Half saturation constant for N uptake	1.2 ± 0.1	1.2 ± 0.1	1.23	$mmol\ m^{-3}$
Phytoplankton maximum growth rate parameters	a) 1.6 ± 0.2 b) 1.066 c) 1.0	1.7 ± 0.1 1.066 1.0	1.8 1.066 1.0	day^{-1}
Phytoplankton mortality	0.02 ± 0.01	0.02 ± 0.01	0.03	day^{-1}
Zooplankton assimilation efficiency	0.75 ± 0.1	0.6 ± 0.25	0.85	
Zooplankton maximum grazing rate	2.55 ± 1.05	2.0 ± 0.5	1.70	day^{-1}
Zooplankton prey capture rate	2.9 ± 1.1	3.1 ± 0.8	2.86	$(mmol\ N/m^2)^{-1}\ day^{-1}$
Zooplankton (quadratic) mortality	0.8 ± 0.1	0.3 ± 0.2	0.64	$(mmol\ N/m^3)^{-1}\ day^{-1}$
Zooplankton excretion	0.01	0.01	0.01	day^{-1}
Remineralization rate	0.10	0.10	0.10	day^{-1}
Sinking velocity	5.00	5.00	5.00	$m\ day^{-1}$

Table 2.4: EMS parameter set for CE and ACE. EMS contains a total of 104 different parameters, in this table are shown only the parameters that were allowed to vary during the data assimilation analyses (except large and small phytoplankton cells diameter, remineralization rate and sinking velocity).

PARAMETER	CE	ACE	CE + ACE	Unit
Large zooplankton growth efficiency	0.37 ± 0.03	0.29 ± 0.05	0.34	
Small zooplankton growth efficiency	0.33 ± 0.03	0.27 ± 0.02	0.30	
Large phytoplankton natural (linear) mortality rate	0.01 ± 0.003	0.01 ± 0.003	0.01	day^{-1}
Small phytoplankton natural (linear) mortality rate	0.02 ± 0.008	0.02 ± 0.01	0.02	day^{-1}
Large zooplankton natural (quadratic) mortality rate	0.76 ± 0.15	0.42 ± 0.08	0.55	$(mmol\ N/m^3)^{-1}\ day^{-1}$
Small zooplankton natural (quadratic) mortality rate	0.35 ± 0.02	0.42 ± 0.08	0.36	$(mmol\ N/m^3)^{-1}\ day^{-1}$
Large phytoplankton maximum growth rate at Tref	1.85 ± 0.25	1.7 ± 0.2	2.0	day^{-1}
Large phytoplankton cells diameter	40.0	40.0	40.0	μm
Small phytoplankton maximum growth rate at Tref	1.1 ± 0.1	1.1 ± 0.1	1.1	day^{-1}
Small phytoplankton cells diameter	2.0	2.0	2.0	μm
Small zooplankton maximum growth rate of at Tref	0.38 ± 0.02	0.4 ± 0.03	0.41	day^{-1}
Small zooplankton swimming velocity	0.002 ± 0.0005	0.0015 ± 0.0003	0.0022	m/s
Large zooplankton maximum growth rate at Tref	0.85 ± 0.25	0.4 ± 0.1	0.62	day^{-1}
Large zooplankton swimming velocity	0.052 ± 0.003	0.06 ± 0.005	0.058	m/s
Remineralization rate	0.10	0.10	0.10	day^{-1}
Sinking velocity	5.00	5.00	5.00	$m\ day^{-1}$

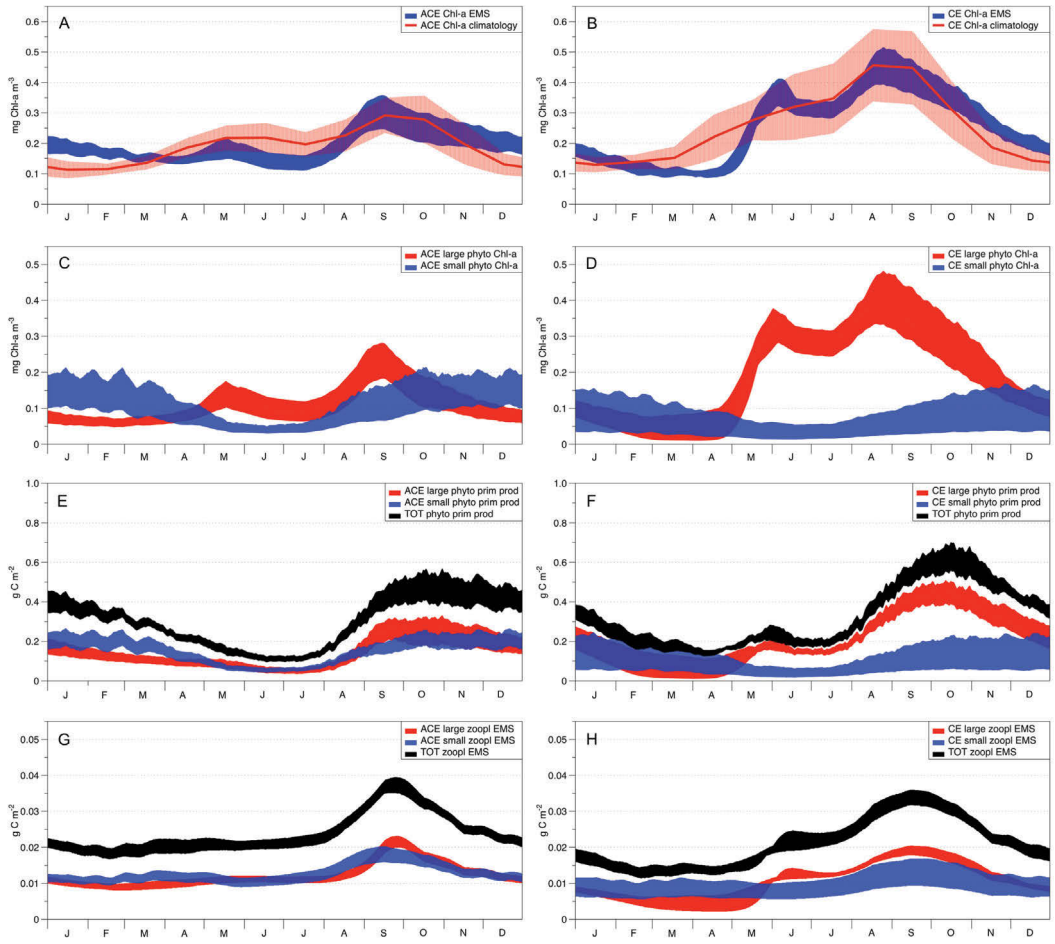

Figure 2.6: EMS acceptable solutions from the data assimilation. Left column shows ACE seasonality and right column CE seasonality. The red solid lines in plots A and B show the Chl-a observed seasonal climatology with the red shading denoting the standard deviation variability. Patterns of the two EMS phytoplankton classes (Chl-a) are represented in plot C (ACE) and D (CE), where red areas represent the large phytoplankton class (40 µm diameter) and blue areas represent the small phytoplankton class (2 µm diameter). Plots E (ACE) and F (CE) represent the total primary production (g C m^{-2}) in black and the primary production for small (blue) and large phytoplankton (red). The total zooplankton biomass (g C m^{-2}) is represented in black on plots G (ACE) and H (CE), while the small and large zooplankton biomass is represented in blue and red, respectively.

2.4.3 Shipboard manipulation experiment

The initial phytoplankton community sampled below the EAC MLD, at ~110 m in June was composed mainly of picophytoplankton (<2 µm) and nanophytoplankton (2-20 µm) while the microphytoplankton (>20 µm)

was the least abundant phytoplankton size class (Fig. 2.7A). *Prochlorococcus* (as indicated by the concentration of divinyl chlorophyll-a) and haptophytes (hex-fucoxanthin) were the dominant phytoplankton classes in the initial community (Fig. 2.7B). At the end of the shipboard experiment, the phytoplankton composition (as determined by pigment analyses) was similar in all treatments (Fig. 2.7). By the end of the experiment, there was a large change in the phytoplankton community, highlighting a shift from nano and picophytoplankton to the larger microphytoplankton (Fig. 2.7A) and from *Prochlorococcus* and haptophytes to diatoms (Fig. 2.7B). The pigment concentrations in the control vessels at the end of the experiment were below detection (>0.004 µg L^{-1}), and are hence shown as zero in Fig. 2.7.

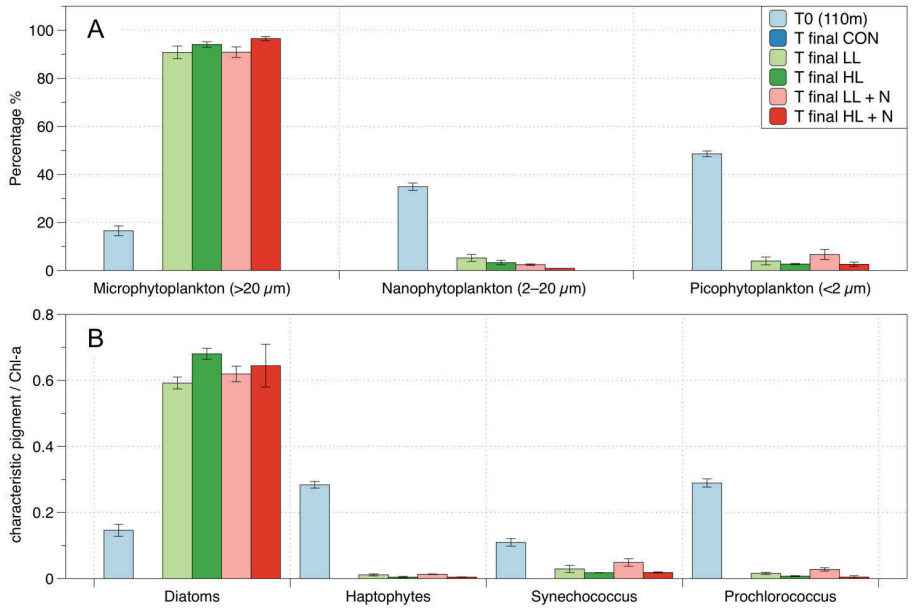

Figure 2.7: Pigment analysis of phytoplankton in different treatments (shipboard incubation experiment): A) size distribution at the initial and final time of the experiment; B) ratio between characteristic phytoplankton classes pigment and total Chl-*a* (Diatoms: Fucoxanthin, Haptophytes: 19-Hex-fucoxanthin, Synechococcus: Zeaxanthin, *Prochlorococcus*: DV Chlorophyll *a*, Barlow et al. (2004)). In all panels it is represented the "T0 (110m)" showing the initial condition and the "T final" showing the last day of the experiment (6th day). The treatments are labelled as: LL (20% surface irradiance), HL (40% surface irradiance), N (daily nutrients addition). The control (CON, ~1% incident light, no nutrient amendment). The CON is not represented at the end of the experiment (T final) because the pigment concentrations were below detection (>0.004 µg/L).

2.5 Discussion

2.5.1 The Role of Mixed Layer Depth and Light on Phytoplankton

Statistical analysis of the MLD and Chl-a seasonal climatologies clearly shows that CE and ACE off eastern Australia are two distinct environments (Fig. 2.4, Table 2.2). Similarities in the MLD and Chl-a seasonal climatology dynamics (Fig. 2.4) suggest the MLD could be a key environmental driver of differences in Chl-a between these two environments. The importance of MLD deepening to Chl-a seasonality in subtropical water is consistent with a recent study of Chl-a variability in eddies of the Indian Ocean (Dufois et al. 2016).

In both the single and multiple box phytoplankton models, the MLD seasonal climatology was enough to drive the phytoplankton dynamics and reflect the observed differences between the CE and ACE environments (Fig. 2.5A-B, 2.6A-B). Although our simulations did not take physical dynamics (i.e., sub-mesoscale events) directly into account, these processes are indirectly accounted for by the implementation of observed CE and ACE MLD.

WOMBAT and EMS simulations confirm that MLD dynamics play an important role in driving the Chl-a concentration in both eddy types. The evolution of the MLD leads to a change in both the nutrient concentration and the light available for photosynthesis, which in turn influences the phytoplankton abundance and community composition (Officier and Ryther, 1980; Pitcher et al., 1991; Tilburg et al., 2002). The differences in Chl-a and MLD between CE and ACE are greatest in the austral winter/spring when surface light irradiance are near their seasonal minimum (Fig. 2.3B). During the winter/spring period the MLD is deep and it has been shown to cause strong light limitation of phytoplankton growth (Behrenfeld and Boss 2014). McGillicuddy, (2015) hypothesized that in such a light-limited regime, the shallower MLD of the CE than ACE could lead to higher Chl-a concentration in CE.

The shipboard manipulation experiment clarifies the effect of light and nutrients on the phytoplankton community sampled in the same area as our modeling study. The water collected in austral winter from below the MLD (110 m) originally contained a low abundance of phytoplankton (total Chl-a concentration 0.068 ± 0.003 μg L^{-1}, mean ± standard deviation). After being exposed to 1 % surface light (ambient irradiance at the sampling depth) for 6 days, phytoplankton were undetectable (<0.004 μg Chl-a L^{-1}), confirming they did not have enough light to remain viable. The same phytoplankton community exposed to 20 % and 40 % surface irradiance resulted in growth and showed a similar shift in community structure whether nutrients were added or not (Fig. 2.7A). The shipboard experiment reveals that, in this region, during winter while the MLD is still deepening (Fig. 2.4A), the phytoplankton growth is limited by light rather than by nutrients.

2.5.2 Phytoplankton composition and size structure

During the shipboard experiment with elevated light, the phytoplankton community shifted from picophytoplankton (<2 μm; ~49 % of the initial community) and nanophytoplankton (2–20 μm; ~35 % of the initial community) to microphytoplankton (>20 μm; ~90 % of the final community) (Fig. 2.7A). The microphytoplankton appear most light-limited because they are initially in lowest abundance and then dominate the community when exposed to elevated light. The microphytoplankton are almost totally composed of fucoxanthin-containing cells, most likely reflecting diatoms (Fig. 2.7B).

Data assimilation with WOMBAT and EMS showed that both models could represent the seasonal evolution of Chl-a in the two types of eddies if the two environments had different parameter values (Table 2.2). The physical and chemical environment that characterizes the CE in oligotrophic oceans, generally drives the accumulation of large phytoplankton species such as diatoms, while small phytoplankton species and cyanobacteria are more characteristic of the surrounding waters and ACE (Jeffrey and Hallegraeff, 1980; Olaizola et al., 1993; Vaillancourt et

al., 2003; Rodriguez et al., 2003; Brown et al., 2008). EMS simulations are consistent with such behavior where different phytoplankton dominate CE and ACE (Fig. 2.6). In particular, EMS simulations show the differences between CE and ACE Chl-a concentrations are attributed to the large phytoplankton class, while the small phytoplankton class has similar dynamics in both the systems (Fig. 2.6C, 2.6D). The greatest difference in the EMS simulated large phytoplankton occurs between May and October when observed Chl-a shows the greatest differences between the ACE and CE Chl-a (Fig. 2.6).

Trying to get WOMBAT to use one parameter set to represent both CE and ACE failed to satisfactorily represent Chl-a observations (Table 2.2). WOMBAT's failure to represent the two environments with a unique parameter set may be expected for a model that does not resolve different plankton sizes. However, the parameter values from fitting the two environments separately are very similar. Furthermore, EMS with its two sizes of phytoplankton shows a similar pattern to WOMBAT, where model simulations are unable to produce an acceptable Chl-a simulation using one parameter set to represent both ACE and CE. This suggests that it is more than phytoplankton size that is driving differences between Chl-*a* in CEs and ACEs.

2.5.3 Zooplankton

For both WOMBAT and EMS, the optimized parameter sets suggest that the zooplankton in CE have twice the mortality rate and nearly double the growth rate compared to the ACE (Tables 2.3 and 2.4). Hence, in both models, the phytoplankton grow better in CE than in ACE, because of the higher mortality of their grazers which reduces top-down grazing pressure. Bakun (2006) suggests that an enhanced primary production (typical of CEs) improves zooplankton growth but comes at a cost of increased zooplankton predator abundance; this concept is consistent with the higher zooplankton mortality and growth rate obtained from the parameter optimization in the CE system (Table 2.3 and 2.4). Another possible explanation is that two distinct zooplankton communities

characterize CE and ACE, with higher grazing pressure in CE environments. Such behavior is consistent with the water in CEs from this region tending to have more coastal organisms than ACEs (Macdonald et al., 2016). However, the interpretation of the difference in zooplankton behavior requires some caution because it may be related to eddy dynamics not directly considered in our simulations (i.e., sub-mesoscale interactions). While the differences in zooplankton properties between CE and ACE is a robust feature of the model simulations, additional observations are needed to confirm this result and determine the mechanism responsible.

2.6 Conclusion

Biogeochemical models are increasingly considering phytoplankton composition to characterize elemental cycles in the contemporary and future ocean (Finkel et al., 2009; Follows and Dutkiewicz, 2011). This study shows that inclusion of multiple phytoplankton groups provides useful, and potentially unexpected, insights about ecosystem dynamics, demonstrating divergent accumulation of biomass in different phytoplankton and zooplankton size classes in CE and ACE.

To put the impact and relevance of these mesoscale features in eastern Australian waters into perspective, an average of 13 CE and 15 ACE with a lifetime equal to or greater than 10 weeks occur annually in the study region (obtained from Chelton et al., 2011 eddy database, yearly average from 1 December 2002 to 4 April 2012). Given that the primary productivity in East Australia is projected to increase 10% by the 2060s due to an increase in eddy activity (Matear et al., 2013), it is therefore critical to quantify plankton concentration, composition and functioning within eddies and adjacent water masses to advance our understanding of their ecological and trophic roles and impacts to regional fisheries and biogeochemical cycling.

2.7 Acknowledgments

Leonardo Laiolo would like to thank Mark Baird, Farhan Rizwi and Mathieu Mongin (CSIRO) for their useful suggestions and explanations about the Environmental Modelling Suite (EMS), Olivier Laczka (UTS) for his assistance with setting up the experiment aboard the RV Investigator and Gabriela Semolini Pilo (UTAS) for the useful conversations about eddy dynamics. This research was supported by the Australian Research Council Discovery Projects funding scheme (DP140101340 awarded to MD and RM), the Marine National Facility, and the School of Life Science, University of Technology Sydney (postgraduate scholarship to LL) and the Climate Change Cluster research institute (operational support). The authors would like to acknowledge the captain and crew of the IN2015_V03 voyage, as well as the chief scientist, Prof. Iain Suthers. Furthermore, we would like to thank GlobColour, AVISO and the International Argo Program for the production and distribution of the dataset used in this study.

CHAPTER 3

Information content of *in situ* and remotely sensed chlorophyll-*a*: learning from size-structured phytoplankton model

Leonardo Laiolo[1, 2], Richard Matear[2], Mark E. Baird[2], Monika Soja-Woźniak[2], Martina A. Doblin[1]

[1]Climate Change Cluster, University of Technology Sydney, 8-15 Broadway, Ultimo, NSW, 2007, Australia

[2]CSIRO Oceans and Atmosphere, Hobart, 3-4 Castray Esplanade, TAS, 7004, Australia

"This Chapter has been previously published in the *Journal of Marine Systems* on the 22nd March 2018"

Citation:

Laiolo L., Matear R., Soja-Woźniak M., Doblin M. A., 2018. Information content of in situ and remotely sensed chlorophyll-a: learning from size-structured phytoplankton model. Journal of Marine Systems, 183: 1-12. https://doi.org/10.1016/j.jmarsys.2018.03.005

3.1 Abstract

Chlorophyll-*a* measurements in the form of *in situ* observations and satellite ocean colour products are commonly used in data assimilation to calibrate marine biogeochemical models. Here, a two size-class phytoplankton biogeochemical model, with a 0D configuration, was used to simulate the surface chlorophyll-*a* dynamics (simulated surface Chl-*a*) for cyclonic and anticyclonic eddies off East Australia. An optical model was then used to calculate the inherent optical properties from the simulation and convert them into remote-sensing reflectance (R_{rs}). Subsequently, R_{rs} was used to produce a satellite-like estimate of the simulated surface Chl-*a* concentrations through the MODIS OC3M algorithm (simulated OC3M Chl-*a*). Identical parameter optimisation experiments were performed through the assimilation of the two separate datasets (simulated surface Chl-*a* and simulated OC3M Chl-*a*), with the purpose of investigating the contrasting information content of simulated surface Chl-*a* and remotely-sensed data sources. The results we present are based on the analysis of the distribution of a cost function, varying four parameters of the biogeochemical model. In our idealised experiments the simulated OC3M Chl-*a* product is a poor proxy for the total simulated surface Chl-*a* concentration. Furthermore, our result show the OC3M algorithm can underestimate the simulated chlorophyll-*a* concentration in offshore eddies off East Australia (Case I waters), because of the weak relationship between large-sized phytoplankton and remote-sensing reflectance. Although Case I waters are usually characteristic of oligotrophic environments, with a photosynthetic community typically represented by relatively small-sized phytoplankton, mesoscale features such as eddies can generate seasonally favourable conditions for a photosynthetic community with a greater proportion of large phytoplankton cells. Furthermore, our results show that in mesoscale features such as eddies, *in situ* chlorophyll-*a* observations and the ocean colour products can carry different information related to phytoplankton sizes. Assimilating both remote-sensing reflectance and measurements of *in situ* chlorophyll-

a concentration reduces the uncertainty of the parameter values more than either data set alone, thus reducing the spread of acceptable solutions, giving an improved simulation of the natural environment.

3.2 Introduction

Satellite sensors measuring radiance in the visible range such as MERIS, OLCI, SeaWiFS and MODIS provide useful ocean color data to support the marine sciences community (McClain, 2009; Antoine et al., 2014). Such datasets can be used to estimate surface ocean circulation patterns (Barton, 2002; Pegau et al., 2002), phytoplankton primary production (Longhurst et al., 1995; Carr et al., 2006) and to investigate upwelling regions (Poulain et al., 2004; Farikou et al., 2015). Furthermore, the satellite ocean color data can be used to estimate chlorophyll-*a* concentrations (Chl-*a*), which is often used to calibrate biogeochemical models, optimizing their biological parameters (Hemmings et al., 2003; Laiolo et al., 2016).

Radiance measured at the satellite sensor comprises the combination of surface-reflected radiance, water-leaving radiance and atmospheric radiance (Robinson, 2004). The only component that provides information on ocean properties, such as Chl-*a* concentration, is the water-leaving radiance; therefore corrections are applied to remove atmospheric and surface-reflected radiance components from the water upwelled signal (e.g. Schroeder et al., 2007). The intensity and spectral characteristics of the water-leaving radiance are determined by the scattering and absorption properties of the water, dissolved matter, and particulates in the water, including organic and inorganic components (e.g. Kirk, 1983; Gordon et al., 1988; IOCCG, 2006). The optical properties of all these elements define the inherent optical properties (IOPs) of the water column (Dickey et al., 2006). Specifically, light can be absorbed or scattered: while scattering is the physical process that deviates the angle of the photon path, absorption removes photons permanently from their path (Dickey et al., 2006). The absorption process is fundamental for

phytoplankton photosynthesis, allowing phytoplankton to synthesize organic compounds from inorganic carbon dioxide (CO_2) and nutrients, providing organic matter, directly or indirectly, for almost all marine life (Falkowski, 2012). The measures of absorption and scattering processes are commonly defined as absorption (*a*) and scattering (*b*) coefficients. The relationship between the scattering coefficient in a backward direction (backscattering coefficient, b_b) and absorption coefficient is used to estimate remote-sensing reflectance (R_{rs}) (i.e., $R_{\mathrm{rs}} \propto \frac{b_b}{a + b_b}$).

Phytoplankton absorption spectra vary in magnitude and shape due to the different pigment composition and packaging (Bidigare et al., 1990; Bricaud and Stramski, 1990; Hoepffner and Sathyendranath, 1991; Ciotti et al., 2002; Lewis, and Cullen, 2002; A. Bricaud et al., 2004). The increase in cellular pigment concentration and cell size, i.e. packaging effect, flattens the specific absorption spectra (Duysens, 1956; Kirk, 1976; Morel and Bricaud, 1981). Due to strong absorptive properties and high water content in phytoplankton cells, their scattering coefficients are relatively low (Aas, 1996). Phytoplankton cell dimensions are significantly larger than wavelengths of visible light (micrometers compared to nanometers), therefore forward scattering (up to 90°) dominates over scattering in the backward direction (between 90° and 180°) (Volten et al., 1998). Scattering and backscattering coefficients of phytoplankton are highly dependent on size, shape and refractive index of components of the phytoplankton cell (Jonasz and Fournier, 2007; Sullivan and Twardowski, 2009; Volten et al., 1998; Witkowski et al., 1998).

Marine biogeochemical models are useful tools that help to understand, conceptualize and predict marine environmental processes, including phytoplankton dynamics, represented in the basic Nutrient, Phytoplankton, Zooplankton and Detritus (NPZD) structure of these models (Fennel and Neumann, 2004). Marine biogeochemical models usually comprise numerous parameters and estimating their values is a non-linear problem (Matear, 1995; Athias et al., 2000; Jones et al., 2016). Thanks to their continuous acquisition and spatial coverage, ocean color

data are particularly suitable for data assimilation in marine biogeochemical models, with most studies using remotely-sensed Chl-*a* as the product to assimilate.

Data assimilation (DA) is a useful process that combines observations and models to estimate variables. In the biogeochemical modelling space there are two uses of DA, state estimation and parameter estimation. In state estimation, DA is performed to improve the predictive power of models. In this approach the state variables are modified to fit the observations and produce a more realistic evolution of the ocean state (e.g. Shulman et al., 2013; Teruzzi et al., 2014; Ciavatta et al., 2016). Another application of DA in biogeochemical modeling is related to optimization of parameters. In this case the model parameters are modified to fit the observations (e.g. Doron et al., 2013; Laiolo et al., 2016; Gharamti et al., 2017). The parameter optimization involves usually three main steps: (1) running the model forward in time, (2) comparing simulation results with the observations through a cost function to quantify the differences between the two datasets, and (3) modifying the parameter values accordingly until the best fit to the data is obtained (i.e. minimize the cost function value). Ocean color DA is a field in development that can improve the accuracy of biological variables in marine biogeochemical models. While analyzing or assimilating ocean color data is feasible, it is essential to consider the complexity and variability of the bio-optical properties that comprise the water-leaving radiance and the derived Chl-*a* data (Babin et al., 2003; Oubelkheir et al., 2006). Indeed, in open ocean waters (i.e. Case I waters), the complexity and variability of bio-optical properties decrease the accuracy of satellite data products of up to ± 5% for water-leaving radiance and ± 35% for the corresponding Chl-*a* product (McClain, 2009). Furthermore, on a global scale, there is a non-uniform distribution of accuracy in the derived Chl-*a* concentration, with a significant error increase in coastal waters (i.e. Case II waters, Odermatt et al., 2012). Marine biogeochemical DA is now moving beyond the assimilation of Chl-*a* derived from remotely sensed ocean colour. Jones et

al. (2016) have already shown that in a coastal domain (Case II water), assimilating a combination of remote-sensing reflectance wavebands leads to a significant improvement over assimilating ocean colour derived Chl-*a*.

3.2.1. Model simulations to understand observation platforms

In this study, we exploit the recent development of optical models linked to phytoplankton dynamics (e.g. Dutkiewicz et al., 2015; Baird et al., 2016; Jones et al., 2016), presenting an idealized study for East Australia open ocean (Case I) waters. Specifically, we used a two phytoplankton size class dependent biogeochemical model (Environmental Modeling Suite, EMS), with a 0D configuration, to simulate Chl-*a* dynamics from a published set of parameter values (hereafter 'original parameter set', Table 3.2; Laiolo et al., 2016) in cyclonic and anticyclonic eddies off East Australia. We called the obtained synthetic dataset "simulated surface Chl-*a*" (Fig. 3.1a). We then use the same output from EMS to obtain the IOPs and the corresponding R_{rs} through an optical model (Appendix; Baird et al., 2016). R_{rs} was converted to Chl-*a* concentration through the OC3M algorithm (Moderate Resolution Imaging Spectroradiometer or MODIS, three band Chl-*a* algorithm; https://oceancolor.gsfc.nasa.gov/atbd/chlor_a/#sec_2; O'Reilly et al., 1998), obtaining a satellite-like Chl-*a* product that we called "simulated OC3M Chl-*a*" (Fig. 3.1a). Therefore, the two synthetic datasets obtained are related, and to explore their properties we evaluated a defined cost function in a DA parameter optimization problem. Twin experiments were performed (Fig. 3.1b) in which, with perturbed parameter values, we investigated the ability of the DA system to recover the parameter values from an unperturbed EMS simulation.

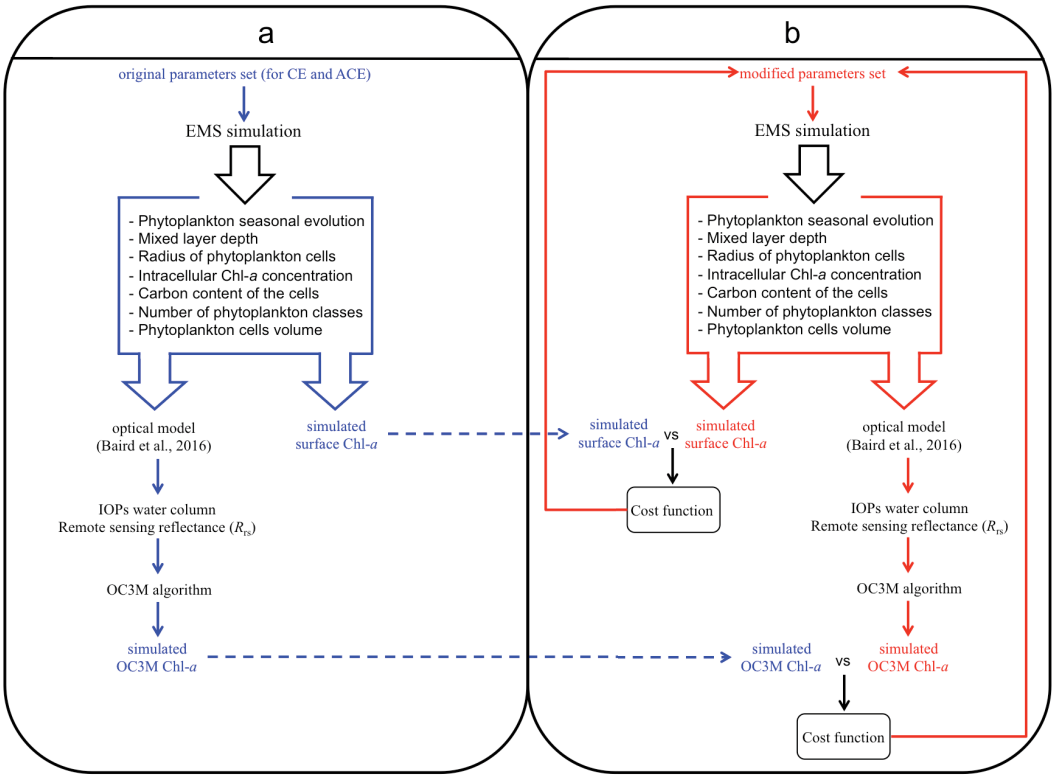

Figure 3.1 Diagrams representing how the two synthetic datasets were created (panel a) and how the twin experiments were conducted (panel b).

3.3 Materials and Methods

3.3.1 Study Region and Biogeochemical Model Description

The region selected for this study is located in the eastern Australian ocean, between 30° and 40°S and 150° and 160°E (Fig. 3.2). This area is crucial for Australia's marine ecology and economy, fisheries and tourism (Hobday and Hartmann, 2006; Brieva et al., 2015). Furthermore, it is strongly influenced by the major western boundary current of the South Pacific, the Eastern Australian Current (EAC) (Mata et al., 2000; Ridgway and Dunn 2003). The EAC originates from the warm oligotrophic waters of the Coral Sea and during its southward flow forms eddies that stimulate phytoplankton growth and enhance primary production (Falkowski et al., 1991; Hassler et al., 2010; Doblin et al., 2016). These phenomena are particularly intense in the area we selected (Ridgway and Dunn, 2003).

A marine Nutrient, Phytoplankton, Zooplankton and Detritus

(NPZD) biogeochemical model, EMS, was used in this study. It was developed to couple physical, chemical, and biological processes (CSIRO Coastal Environmental Modelling Team, 2014; http://www.emg.cmar.csiro.au/www/en/emg/software/EMS.html). For this study, EMS was set up with the same structure as used in Laiolo et al. (2016), with a 0D configuration, two phytoplankton and zooplankton size dependent classes characterized by a variable C:Chl-*a* ratio (Baird et al., 2013). Forcing functions driving the phytoplankton dynamics, and therefore the total Chl-*a*, were the temperature within the mixed layer and nutrients below the mixed layer, both acquired from the CSIRO Atlas of Regional Seas dataset (CARS; http://www.marine.csiro.au/~dunn/cars2009/; Ridgway et al., 2002). Surface incident irradiance was obtained from the seasonal climatology of the selected study area (Large and Yeager, 2008). EMS was configured as 0D, representing a well-mixed mixed layer depth; therefore, biological components were considered as concentrations equally distributed within this layer.

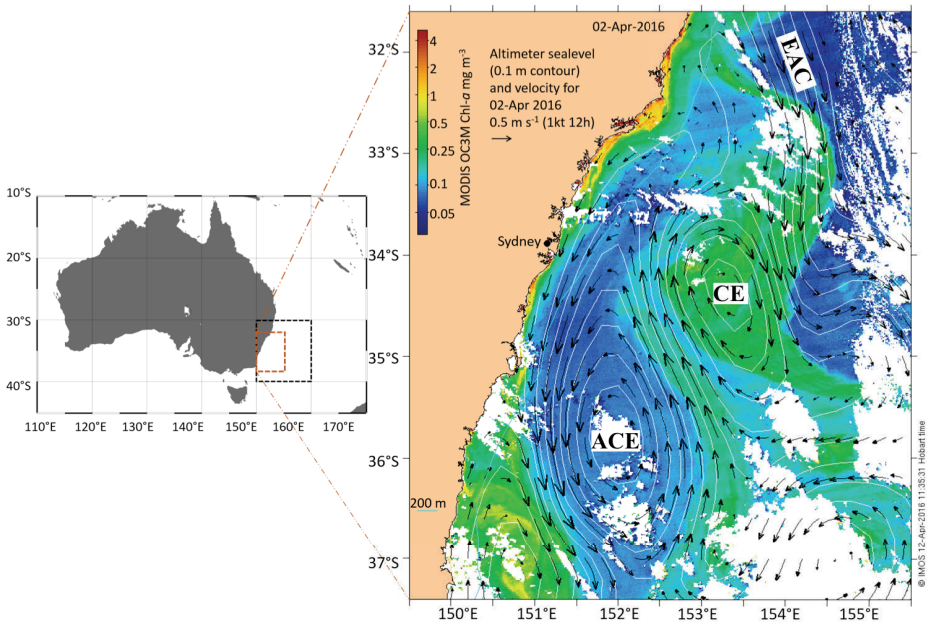

Figure 3.2 Australian region and the study area highlighted by the dashed line (150° E – 160° E; 30° S – 40° S). To illustrate the main features (cyclonic eddy CE, anticyclonic ACE, East Australian Current EAC) occurring in the study area, the satellite image of surface Chl-*a* calculated with OC3M algorithm using reflectance acquired with the MODIS

radiometer (2nd April 2016) and the current pattern based on altimeter data is shown. Data source: Australia's Integrated Marine Observing System (http://oceancurrent.imos.org.au/oceancolour.php).

3.3.2 Simulated surface Chlorophyll-*a* and simulated OC3M Chlorophyll-*a* synthetic dataset

To obtain the simulated surface Chl-*a* synthetic dataset two distinct EMS simulations were carried out. Following Laiolo et al. (2016), EMS was configured with two phytoplankton size classes (2 µm and 40 µm diameter), to simulate the typical Chl-*a* seasonal dynamics in a cyclonic (CE) and anticyclonic eddy (ACE) off East Australia (Table 3.2; Fig. 3.1a, b). CE and ACE are two ideal case studies as they represent two distinct environments with different phytoplankton dynamics and concentrations (Fig. 3.1a, b; Angel and Fasham, 1983; Moore et al., 2007; Laiolo et al., 2016). Once the CE and ACE Chl-*a* time-series were extracted from the EMS simulations, it was possible to calculate the corresponding R_{rs}, based on optical model presented in Baird et al. (2016). The optical model performance has been previously assessed with MODIS R_{rs} in an area adjacent to the East Australia study region (i.e., Great Barrier Reef; Baird et al., 2016). First, the IOPs were computed from the state variables (e.g. Chl-*a* concentration) and model parameters (e.g. cell dimension). Then the apparent optical properties (AOPs) including R_{rs} were calculated through the relationship with backscattering and absorption coefficients (i.e., $R_{\mathrm{rs}} \propto \frac{b_b}{a + b_b}$) (Fig. 3.1b; Baird et al., 2016). Additional details about the optical model calculations of IOPs and R_{rs} are given in the Appendix. To explore the relationship between EMS phytoplankton biomass and corresponding R_{rs}, we set up the optical model to take into account both absorption and scattering for pure seawater and phytoplankton cells. Because our study area covers only Case I waters, where phytoplankton is the main component responsible for variations in optical properties (Gordon and Morel 1983; Morel and Prieur 1977; Mobley et al., 2004), other optically significant seawater constituents such as coloured

dissolved organic matter (CDOM), non-algal particulates (NAP) and benthic reflectance were not considered.

The R_{rs} time-series was then used to obtain the simulated OC3M Chl-*a* product, following the OC3M algorithm (https://oceancolor.gsfc.nasa.gov/atbd/chlor_a/#sec_2; O'Reilly et al., 1998). The NASA OC3M algorithm consists of a fourth-order polynomial relationship between logarithms of R_{rs} ratios and Chl-*a*:

$$\log_{10}(\text{Chl-}a) = a_0 + \sum_{i=1}^{4} a_i \left(\log_{10}\left(\frac{\max(R_{rs}(443),\ R_{rs}(488))}{R_{rs}(551)}\right)\right)^i \qquad (1)$$

where a_i is a sensor specific coefficient (MODIS: a_0= 0.2424, a_1=-2.7423, a_2=1.8017, a_3=0.0015, a_4=-1.2280), $R_{rs}(443)$, $R_{rs}(488)$ and $R_{rs}(551)$ represent remote sensing reflectance at 443 nm, 488 nm and 551 nm respectively.

Table 3.1 EMS 'original parameter set' for cyclonic eddy (CE) and anticyclonic eddy (ACE) used to obtain the simulated surface Chl-*a* dataset; T_{ref} refers to reference temperature (Laiolo et al., 2016). The sub-set of parameters included in this study is composed of large phytoplankton natural (linear) mortality, small phytoplankton natural (linear) mortality rate, large zooplankton natural (quadratic) mortality and small zooplankton natural (quadratic) mortality.

Parameter	CE	ACE	Unit
Large zooplankton growth efficiency	0.34	0.34	
Small zooplankton growth efficiency	0.30	0.29	
Large phytoplankton natural (linear) mortality rate	0.01	0.01	day^{-1}
Small phytoplankton natural (linear) mortality rate	0.02	0.02	day^{-1}
Large zooplankton natural (quadratic) mortality rate	0.8	0.35	$(mmol\ N/m^3)^{-1}\ day^{-1}$
Small zooplankton natural (quadratic) mortality rate	0.35	0.35	$(mmol\ N/m^3)^{-1}\ day^{-1}$
Large phytoplankton maximum growth rate at T_{ref}	1.8	1.8	day^{-1}
Large phytoplankton cells diameter	40	40	µm
Small phytoplankton maximum growth rate at T_{ref}	1.0	1.0	day^{-1}
Small phytoplankton cells diameter	2	2	µm
Small zooplankton maximum growth rate of at T_{ref}	0.4	0.4	day^{-1}
Small zooplankton swimming velocity	0.0015	0.0016	m/s
Large zooplankton maximum growth rate at T_{ref}	0.90	0.4	day^{-1}
Large zooplankton swimming velocity	0.053	0.055	m/s
Remineralization rate	0.10	0.10	day^{-1}
Sinking velocity	5.00	5.00	m/day

3.3.3 Settings of the twin experiments

Twin experiments are used to assess the ability of a data assimilation system to recover model parameter values from model output (e.g. Kidston et al., 2011). In this study we conducted four twin experiments in total. For both ACE and CE, we recover the original parameter values from (1) the simulated surface Chl-*a* and (2) from the simulated OC3M Chl-*a* dataset (Fig. 3.1b). To recover the model parameter values we used a conjugate gradient algorithm, used to solve optimization problems with marine biogeochemical models (Fasham et al., 1995; Evans, 1999). The simulated surface Chl-*a* and simulated OC3M Chl-*a* datasets were assimilated in separate experiments changing two parameters simultaneously for each experiment. The purpose of these experiments was to investigate the information content of the two synthetic datasets in relation with the optimized parameters.

As Laiolo et al. (2016) showed, the information content of the Chl-*a* data is insufficient to constrain all parameters in EMS (104 in total), so we chose a sub-set of parameters to test the ability to recover the solution when uncertainty is included in the input dataset (i.e. ± 10% for simulated OC3M Chl-*a*, as we are using two wavelengths, equation (1), McClain, 2009; and ± 5% for simulated surface Chl-*a* based on estimates of uncertainty for in situ Chl-a measurements following Hooker et al., 2012). The key processes that control the evolution of phytoplankton concentration are phytoplankton growth, mortality and zooplankton grazing. Phytoplankton growth is generally determined from the availability of light and nutrients while the two biological parameters that largely determine the phytoplankton dynamics are the phytoplankton mortality and grazing rate (Laiolo et al., 2016). Therefore, the sub-set of parameters included phytoplankton natural mortality rate and zooplankton prey capture rate for both small and large size classes (i.e. four parameters in total). Furthermore, selecting parameters that affect the two phytoplankton size classes dynamics allowed us to explore the relation between

phytoplankton sizes with simulated surface Chl-*a* and the simulated OC3M Chl-*a*.

To quantify the difference between the Chl-*a* synthetic dataset obtained with the 'original parameter set' and the Chl-*a* dynamics from the twin experiments (Fig. 3.1b), a cost function (*x*) was defined as:

$$x = \frac{1}{N}\sum_{t=1}^{T} \frac{(\ln TRUE\_MOD_t - \ln DA\_MOD_t)^2}{(\ln DA\_MOD_t \cdot (err\ \%/100))^2} \quad (2)$$

where $TRUE\_MOD_t$ represents the Chl-*a* value at day *t* of Chl-*a* dataset obtained with the 'original parameter set' which ranged from 1 to 365 (number of days in a year), DA_MOD_t the Chl-*a* value of the DA simulated data at day *t*, *err%* is the accuracy of the selected dataset and *N* represents the degrees of freedom (i.e. *N* = 364). The logarithmic transformation was applied to achieve normal distribution of the Chl-*a* concentrations around the mean seasonal value. Furthermore, to assess that the mean of the Chl-*a* dataset obtained with the 'original parameter set' and the mean of the Chl-*a* dynamics from the DA experiments were consistent, we defined (α) as:

$$\alpha = \frac{(\ln \overline{TRUE\_MOD} - \ln \overline{DA\_MOD})^2}{\frac{\delta^2}{N}} \quad (3)$$

where $\overline{TRUE\_MOD}$ and $\overline{DA\_MOD}$ represent the mean of the Chl-*a* dataset obtained with the 'original parameter set' and the mean of the DA simulated Chl-*a* dataset; *N* represents the degrees of freedom (i.e. *N* = 364) and; δ is a measure of the dataset accuracy:

$$\delta = \ln \overline{DA\_MOD} \cdot (\mathrm{err}\ \%/100) \quad (4)$$

An acceptable fit to the dataset was considered when both (2) and (3) have values of approximately equal to one or less. To illustrate the relationship between the two datasets and the selected parameters, we plot our results in the form of cost function distribution diagrams (e.g. Dowd, 2011), with a final cost function value calculated as the sum of the quantities defined in equation (2) and (3):

$$COST = x + \alpha \quad (5)$$

To produce these diagrams, the analyzed parameters were subjected to a range of perturbations (i.e. ± 40% from the 'original parameter set' value).

3.4 Results

3.4.1. Simulated surface Chlorophyll-*a* and simulated OC3M Chlorophyll-*a* dataset

Simulations were undertaken with environments (temperature, mixed layer depth) characteristic of cold-core eddies (CE) and warm-core eddies (ACE). As expected, the simulations produced higher total Chl-*a* in the CE compared to the ACE environment, with a generally greater Chl-*a* in the large phytoplankton class than the small size class (Fig. 3.1a, b). In our idealized experiment, the comparison of the simulated surface Chl-*a* with the simulated OC3M Chl-*a* showed significant differences in their seasonal cycle: for both CE and ACE the OC3M algorithm underestimated the simulated surface Chl-*a* concentration throughout the entire year (Fig. 3.3a – d). To separate large and small phytoplankton signals in the simulated OC3M Chl-*a* (Fig. 3.3c and d) we first removed all optical factors related to only one phytoplankton size class from the EMS simulation. Then we calculate the optical properties and the R_{rs} related to the second phytoplankton class through the optical model. In the CE environment, the OC3M algorithm underestimated the mean simulated surface Chl-*a* by about a factor of three (mean simulated surface Chl-*a* = 0.27 mg m^{-3}; mean simulated OC3M Chl-*a* = 0.083 mg m^{-3}), while in the ACE environment the OC3M algorithm underestimated the mean simulated surface Chl-*a* by a factor of two (mean simulated surface Chl-*a* = 0.20 mg m^{-3}; mean simulated OC3M Chl-*a* = 0.077 mg m^{-3}). Because the simulated OC3M Chl-*a* is a poor representation of the simulated surface Chl-*a* we did not perform twin experiments between these two synthetic datasets. When contrasting simulated OC3M Chl-*a* with simulated surface Chl-*a* we determined that they are linearly correlated for the small phytoplankton but uncorrelated for the large phytoplankton (Fig. 3.3e and f).

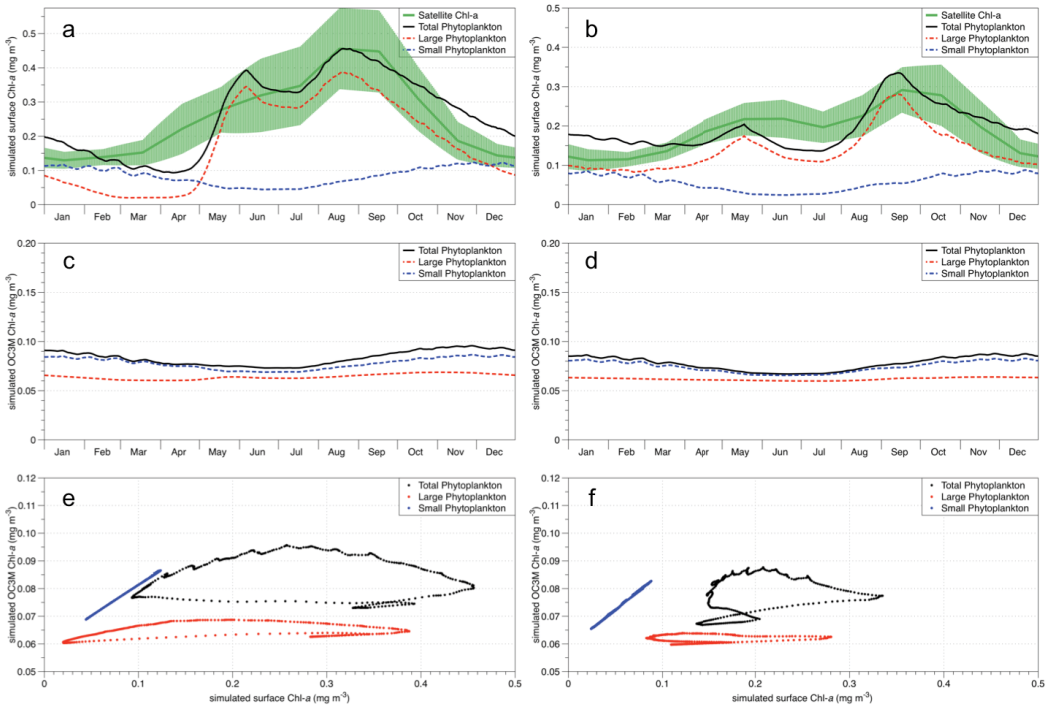

Figure 3.3 Simulated seasonal climatology of total Chl-*a* concentration (solid black line), Chl-*a* in small phytoplankton (blue dotted) and Chl-*a* in large phytoplankton (red dashed line) for CE (a) and ACE (b) off East Australia. The green line represents seasonal climatology for CE (a) and ACE (b) off East Australia (Laiolo et al. 2016) calculated from GlobColour (25 km spatial resolution, 8-day average; http://hermes.acri.fr/index.php?class=archive), while the shaded green areas represent the corresponding standard deviation. The middle panel shows for the same simulations, the corresponding simulated OC3M Chl-*a* obtained from the R_{rs} calculated from the simulated surface Chl-*a* for the two phytoplankton classes (panels a and b) for CE (c) and ACE (d). Note there is a different scale on the Chl-*a* concentration between panel a - c and b - d. The lower panel compares the simulated surface Chl-*a*, with the corresponding simulated OC3M Chl-*a* for CE (e) and ACE (f).

3.4.2. Twin experiments

To assess the information content of the simulated surface Chl-*a* and simulated OC3M Chl-*a* datasets we show how the cost function (Eq. 5) varied as parameter values changed. The visualization of the cost function spread around the global minimum (i.e. cost function equal to zero, using the prescribed parameter values in Table 3.1) allowed us to better understand the relationship between parameters as well as the

information content of the two different datasets that could be used to constrain the model.

In Figure 3.4, as stated in the methods section 2.3, the acceptable region is based on a cost function value (5). The magnitude of the cost function was assessed in relation to several different parameter combinations. In Figure 3.4 the red and blue shaded areas shows the acceptable parameter values for simulated surface Chl-*a* and simulated OC3M Chl-*a* respectively; within this area, light blue and red show a cost function equal to one, highlighting local minima. Blue and red dashed lines show the simulated OC3M Chl-*a* and simulated surface Chl-*a* cost values respectively. An acceptable solution should have a cost value that meets both (x)<1 and (α)<1, represented in the figures by values less than two for both simulated surface Chl-*a* and simulated OC3M Chl-*a* (shaded areas). The diagram axes show the parameters selected for the simulation used to evaluate the cost function and the perturbation applied to their original values (Table 3.2). The black circle in the centre of each panel shows the global minimum (i.e. parameter values used to generate the synthetic dataset to constrain the system, thus here the cost function equals zero).

First, the large phytoplankton mortality and large zooplankton prey capture rate show similar patterns in the cost function values for simulated surface Chl-*a* and simulated OC3M Chl-*a* (Fig. 3.4a). Specifically, the simulated surface Chl-*a* region of acceptable parameter values is totally included inside the simulated OC3M Chl-*a* acceptable region, showing a tighter relationship between simulated surface Chl-*a* and parameters affecting large phytoplankton growth (Fig. 3.4a). Second, with small phytoplankton mortality and small zooplankton prey capture rate, the two different data constraints produce overlapping regions of acceptable parameter values (Fig. 3.4b) for both datasets (i.e. simulated surface Chl-*a* and simulated OC3M Chl-*a*). In this case, the simulated OC3M Chl-*a* region of acceptable parameter values is included inside the simulated surface Chl-*a* region, showing the OC3M Chl-*a* better constrains

parameters affecting small phytoplankton growth (Fig. 3.4b). The region of acceptable parameter values span similar regions and the DA would not be able to determine unique values for both parameters (Fig. 3.4a and b). In summary, for large phytoplankton and zooplankton parameter combinations, simulated surface Chl-*a* more tightly constrains the acceptable parameter values than simulated OC3M Chl-*a* (compare size of red shaded area to blue shaded area; Fig. 3.4a). In contrast, for the small plankton parameters, simulated OC3M Chl-*a* more tightly constrains the acceptable parameter spread than the simulated surface Chl-*a* data (Fig. 3.4b). As both eddy environments show similar cost function distribution diagrams, here we show results related to CE only.

We then explored cases where a combination of large and small plankton parameter values varied. First, we considered the case where small zooplankton prey capture rate and large phytoplankton natural mortality rate varied (Fig. 3.4c). The regions of acceptable parameters were different for the two datasets, with a small area of overlap that includes the global minimum (central area of Fig. 3.4c). Second, we considered the case where small phytoplankton natural mortality and large zooplankton prey capture rate varied (Fig. 3.4d). Again the region of acceptable parameter values was different for simulated surface Chl-*a* and simulated OC3M Chl-*a* (red versus blue shaded areas, respectively), with a small region of overlap matching the global minimum (Fig. 3.4c and d).

In Figure 3.4c, to produce acceptable results that fit the simulated surface Chl-*a* (i.e. red area), the large phytoplankton natural mortality parameter value (Y axis) has to be tightly constrained (i.e. between -10% and +10%), while the parameter in the X axis (i.e. small zooplankton prey capture rate) does not have an impact on the cost function spread (its value can vary between -40% and +40% producing acceptable results). In the same subplot (Fig. 3.4c), if we consider the simulated OC3M Chl-*a* acceptable solution area instead (i.e. blue area), the small zooplankton prey capture rate (X axis) is more tightly constrained (between -40% and +10%) than the large phytoplankton natural mortality parameter (Y axis,

between -40% and +40%). These features are consistent with all the subplots in Figure 3.4, suggesting that the simulated OC3M Chl-*a* better constrains the parameters affecting small phytoplankton dynamics while simulated surface Chl-*a* better constrains the parameters affecting large phytoplankton dynamics. This is consistent with the regions of acceptable parameters evident in Figure 3.4a and b.

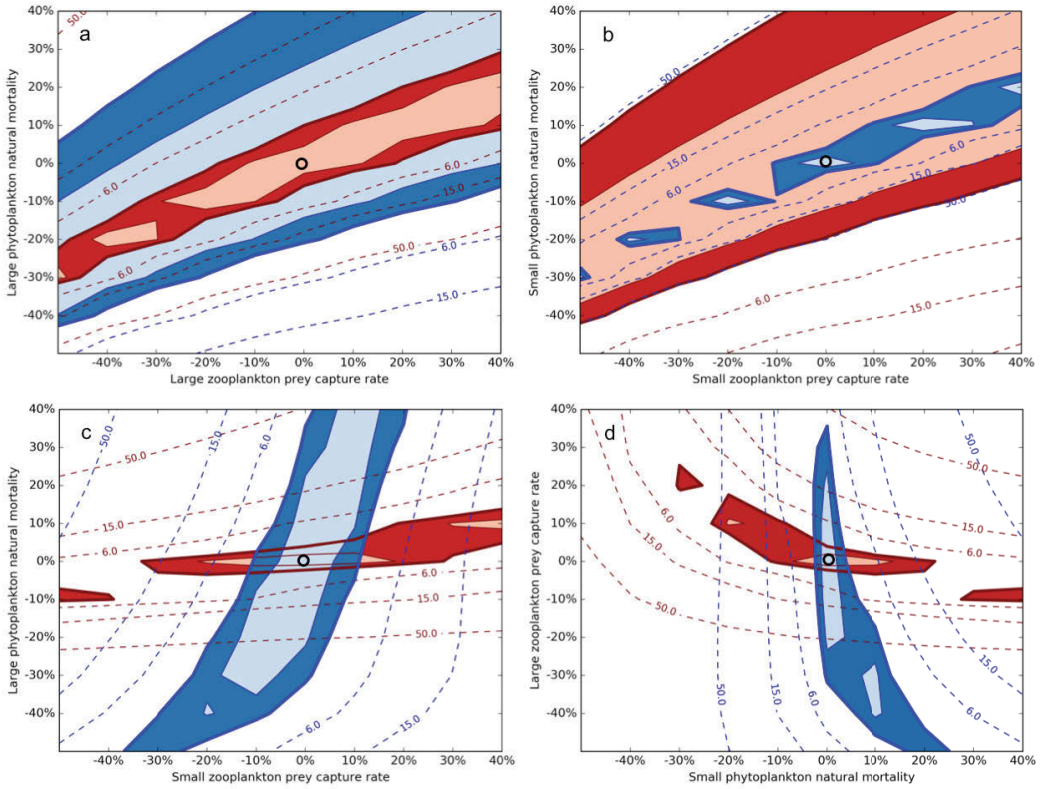

Figure 3.4 For various pairs of parameters, the region of parameter values that produced acceptable fits to the data. Here we show results for CE as similar plots were obtained for ACE. Black circles represent the global minimum, where the cost function is equal to zero. Red shaded areas represent acceptable solutions for the simulated surface Chl-*a* assimilation; within this area, light red shows cost function equal to one highlighting local minima. Red dashed lines show the simulated surface Chl-*a* cost values. Blue dashed lines and blue shaded areas show the simulated OC3M Chl-*a* cost values. Shaded blue areas represent acceptable solutions; within this area, light blue shows a cost function equal to one, highlighting local minima. Acceptable solutions (i.e., (x)<1 and (α)<1) are represented by values less than two.

3.5 Discussion

The idealised twin experiments allowed us to investigate information content of two key data streams – *in situ* Chl-*a* and Chl-*a* derived from water leaving radiances. By comparing the model derived Chl-*a* with Chl-*a* computed from satellite water leaving radiances, we could investigate the resulting impact on key parameters in a biogeochemical model, and how it would impact parameter optimization using DA. By working with model simulations, as well as simulated in-water IOPs from which it was possible to calculate R_{rs} and the corresponding OC3M Chl-*a* product, the phytoplankton dynamics in two different oceanic environments (CE and ACE) could be generated in a consistent manner.

The first key point to emerge from our theoretical study was that, despite the two synthetic datasets being related, the simulated OC3M Chl-*a* product was a poor proxy for the total simulated surface Chl-*a* concentration (Fig. 3.3a - d), suggesting that existing biogeochemical models that assimilate Chl-*a* from ocean colour data could have relatively large inaccuracies. For both CE and ACE simulations, the relationship between large phytoplankton Chl-*a* and simulated OC3M Chl-*a* was poor, with the simulated OC3M Chl-*a* showing little sensitivity to the amount of simulated Chl-*a* in the large phytoplankton (Fig. 3.3c and d). The simulated OC3M Chl-*a* was unable to detect our large phytoplankton cells and this caused a large (up to 3 times) under-estimate of total Chl-*a*. In contrast, for the small phytoplankton cells the OC3M Chl-*a* was good estimator of simulated surface Chl-*a*.

The second key point was that the simulated surface Chl-*a* better constrained parameters affecting large phytoplankton growth while simulated OC3M Chl-*a* better constrained parameters related to small phytoplankton dynamics (Fig. 3.4a and b). This suggests important features about the information that could be extracted from the two data streams, highlighting a stronger relationship between simulated surface Chl-*a* with parameters affecting large phytoplankton dynamics, and

simulated OC3M Chl-*a* with parameters affecting small phytoplankton dynamics.

The third key point to emerge when we tried to determine both small and large plankton parameters (Fig. 3.4c and d) was that simulated surface Chl-*a* and simulated OC3M Chl-*a* contained independent information and if applied together they could dramatically reduce the region of acceptable parameter solutions. Specifically, in a real world scenario, a combination between ocean colour data and *in situ* Chl-*a* concentration measurements could provide enough information for the DA to reduce the spread of acceptable solutions for both small and large plankton parameters. Indeed, for the cases considered here, the DA would find the global minimum, rejecting wide areas that could include several local minima (Fig. 3.4c and d).

For our model setup we chose two phytoplankton size classes, where the radius of the large phytoplankton class was 20 times greater than the small phytoplankton class (2 and 40 μm diameter, respectively). Our choice of the size phytoplankton classes was based on eddies off East Australia (Laiolo et al., 2016). Furthermore, observations of phytoplankton concentrations in similar oligotrophic regions are consistent with this study, showing large phytoplankton (mainly diatoms) occurring within CE and higher concentrations of small phytoplankton including picocyanobacteria located in the surrounding oligotrophic waters (e.g. Jeffrey and Hallengraeff, 1980; Rodriguez et al., 2003; Vaillancourt et al., 2003; Brown et al., 2008).

While use of two size classes with 20 times difference in radius may accentuate the distinctive information carried by simulated surface Chl-*a* and simulated OC3M Chl-*a*, it is known that phytoplankton size influences the IOPs of the water column (Bricaud et al., 1995; Ciotti et al., 2002; Volten et al., 1998; Jonasz and Fournier, 2007; Mouw et al., 2012). Our theoretical study suggests a weak relationship between large sized phytoplankton (e.g., chain forming diatoms, dinoflagellates and colonial cyanobacteria) and R_{rs}, leading to an under-estimation of the satellite

derived Chl-*a* concentration when large phytoplankton dominate the photosynthetic community (Fig. 3.3). The detected R_{rs} is a consequence of the IOPs of the water column or, in other words, the result of either light absorption and/or scattering in the water column (Dickey et al., 2006). To explore these properties in our study, we used the optical model of Baird et al. (2016) to assess how absorption and backscattering were responding to different Chl-*a* and carbon (C) ratios, while maintaining a constant Chl-*a* concentration (0.3 mg m^{-3}) for both phytoplankton size classes (small = 2 µm and large = 40 µm) (Fig. 3.5).

These analyses highlighted that for the small phytoplankton class, as C increases (i.e. increasing number of cells but same amount of total Chl-*a* concentration), there is a corresponding increase in both absorption (Fig. 3.5a) and backscatter (Fig. 3.5c) signals. While the increase in the backscatter signal is related to the higher C concentration (Fig. 3.5c), the slight increase in the absorption (Fig. 3.5a) is related to the packaging of pigments relative to the energy impinging on the geometric cross-section of the cell (i.e. package effect; Ciotti et al., 2002; Bricaud et al., 2004; Ciotti and Bricaud 2006; Astoreca et al., 2012). Therefore, due to the dimension of the phytoplankton cells the packing effect is less evident in the small phytoplankton class for different C:Chl-*a* concentrations. Conversely, for the large phytoplankton class different C:Chl-*a* have a smaller impact on the backscatter signal (Fig. 3.5d), due to the greater dimension of the phytoplankton cells, but a higher impact on the absorption coefficient (Fig. 3.5b), due to the reduced package effect caused by an higher number of larger phytoplankton cells. Because R_{rs} is derived from the relationship between absorption and backscatter ($R_{\mathrm{rs}} \propto \frac{b_b}{a + b_b}$), R_{rs} for large phytoplankton was nearly independent of the C:Chl-*a* (Fig. 3.5f), while variable C:Chl-*a* strongly influenced the R_{rs} for small phytoplankton, particularly in the blue region of the spectrum (Fig. 3.5e).

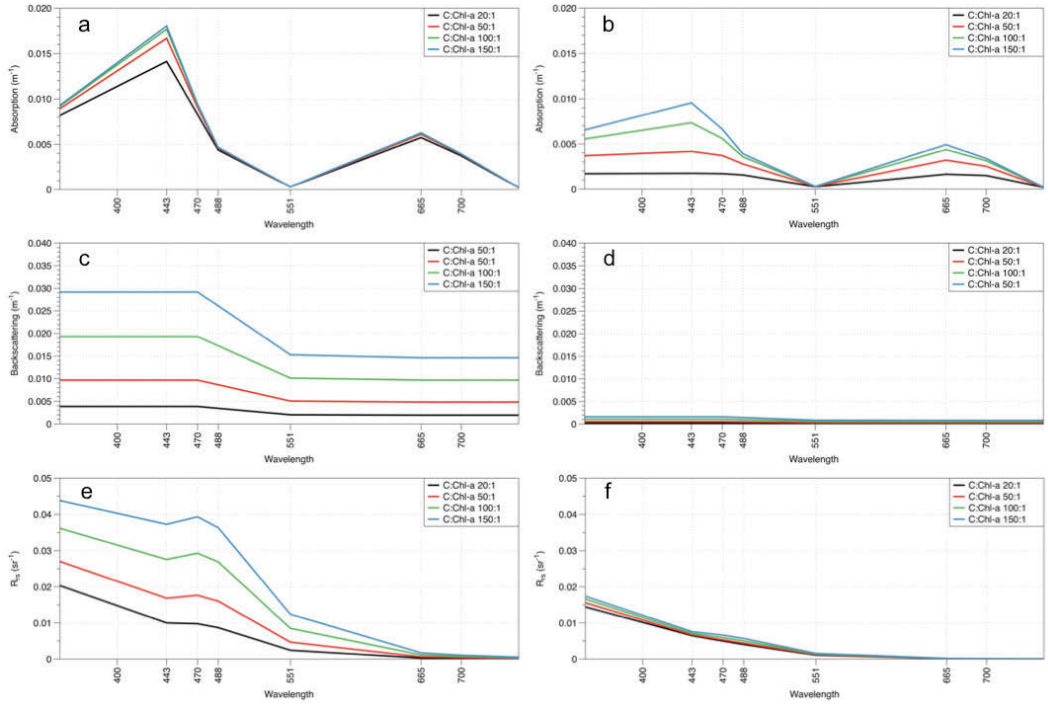

Figure 3.5 Absorption, backscattering and R_{rs} spectra of small (2 µm) (left column) and large (40 µm) (right column) phytoplankton classes for different ratios of phytoplankton Carbon (C) to Chl-*a*. The black lines represent a scenario with 0.3 mg m^{-3} of Chl-*a* and 6 mg m^{-3} C (C:Chl-*a* 20:1); the red lines represent a scenario with 0.3 mg m^{-3} of Chl-*a* and 15 mg m^{-3} C (C:Chl-*a* 50:1); the green lines represent a scenario with 0.3 mg m^{-3} of Chl-*a* and 30 mg m^{-3} C (C:Chl-*a* 100:1); and the blue lines represent a scenario with 0.3 mg m^{-3} of Chl-*a* and 45 mg m^{-3} C (C:Chl-*a* 150:1). The amount of Chl-*a* and C in the left and right columns are equal and entirely distributed in the small phytoplankton class (left) or large phytoplankton class (right). Panels a and b show absorption spectra, panels c and d backscattering and panels e and f the R_{rs} for the two phytoplankton classes.

As phytoplankton abundance increases, usually the proportion of larger phytoplankton cells rises (e.g. Fig. 3.3a and b) and both absorption and scattering spectra are affected. Previous studies show the size of photosynthetic cells has a direct impact on the light absorption efficiency: bigger cells have a lower and spectrally flatter absorption coefficient when compared to smaller phytoplankton cells due to the packaging effect (Ciotti et al., 2002; Bricaud et al., 2004; Ciotti and Bricaud, 2006; Astoreca et al., 2012; Bricaud et al., 1995). This is consistent with results presented in Figure 3.5a and 3.5b. The package effect reduces absorption and can therefore increase the error of estimated Chl-*a* concentration from

observed remote-sensing reflectance (Marra et al., 2007; Mouw et al., 2012). Much less is known about the backscattering of oceanic particles (portion of scattered photons that leave the water column and hence can be measured by satellite sensors) and its relationship with phytoplankton size (Morel and Maritorena, 2001). Factors such as cell shape and internal structure rather than cell size seem to have a bigger impact on backscattering efficiency than size alone (Vaillancourt et al., 2004). Our backscattering analyses are consistent with Stramski and Kiefer (1991), who demonstrated backscattering from Case I waters is dominated by small particles (less than 1 μm), with a much smaller backscattering contribution from cells larger than 8 μm. Our analyses therefore suggest that both absorption and scattering are involved in the weak R_{rs} signal generated from large phytoplankton cells. Lack of the other optically significant components (e.g. NAP and CDOM) in our model can also affect the results, however their influence on optical properties in the study region is minimal.

Results presented in this study suggest that Chl-*a* concentration within open ocean mesoscale features, CE in particular, could be higher than the estimated concentration from the ocean colour product calculated through the OC3M algorithm. Nevertheless, all open ocean waters are categorised as Case I waters and the current MODIS OC3M algorithm converts R_{rs} from these waters to the Chl-*a* concentration product. However, simulation and observational studies are consistent in showing that in oligotrophic waters, seasonal increases in Chl-*a* concentration are generally related to large-sized phytoplankton cells increasing within a background of smaller phytoplankton (e.g., McAndrew et al., 2007; Mouw et al., 2012), suggesting that there could be an underestimation by the OC3M Chl-*a* concentration product across the global ocean (Case I waters) related to local and regional increases in the abundance of large sized phytoplankton abundance. In the East Australia offshore waters, picophytoplankton (e.g., *Prochlorococcus*; Partensky et al., 1999) are often an important component of the phytoplankton community, however,

eddies (CE in particular) can provide a favourable environment for the growth of larger phytoplankton (e.g., diatoms) (McGillicuddy and Robinson, 1997; Rodriguez et al., 2003; Vaillancourt et al., 2003; Brown et al., 2008; Doblin et al., 2016; Laiolo et al., 2016). Indeed, eddies are hot spots of biological activity, with cyclonic eddies alone enhancing the global primary production by 20% (Falkowski et al., 1991; McWilliams, 2008). The area we selected for this study is strongly influenced by eddies that originate from the EAC: an average of 28 eddies with a minimum lifetime of 10 weeks occur every year in our study domain (calculated from Chelton et al., 2011 eddies database). Furthermore, in the same region, climate change projections reveal a strengthening of the EAC with a consequent increase in eddy phenomena (Matear et al., 2013). Surprisingly, recent studies show similar primary production (CE= 337 mg C m^{-2} d^{-1}, ACE=272 mg C m^{-2} d^{-1}, calculated from Laiolo et al., 2016) and average Chl-*a* concentration (CE=0.30 mg m^{-3}, ACE=0.25 mg m^{-3}; Everett et al., 2012; calculated from Chelton et al., 2011 dataset) in eddies located in eastern Australian waters and the adjacent Tasman Sea, respectively. Both these studies (i.e., Everett et al., 2012 and Laiolo et al., 2016) used ocean colour data, therefore the similarities found in CE and ACE could be related to an underestimation of the Chl-*a* concentration in CE, associated with the typical higher abundance of large sized phytoplankton in these mesoscale features. Although it is well known that CE on their own enhance the global primary production by ~20% (Falkowski et al., 1991; McWilliams, 2008), published observations that compare East Australia CE and ACE *in situ* primary productivity are not available yet.

3.6 Conclusion

Ocean colour data play a key role in informing and calibrating marine biogeochemical models through DA methods (Hemmings et al., 2003). For this study, the development of optical models linked to marine biogeochemical models (e.g. Baird et al., 2016; Jones et al., 2016), made it possible to explore properties of MODIS ocean colour data used for DA

purposes. Our idealised experiments showed that the simulated OC3M Chl-*a* product is a poor proxy for the total simulated surface Chl-*a* concentration. Indeed, the OC3M algorithm can underestimate the Chl-*a* concentration in open ocean mesoscale features such as cyclonic (cold core) eddies, because of the weak reflectance signal from large sized phytoplankton classes such as diatoms, that are typically found within CE boundaries. For our idealized model setup where we consider two phytoplankton groups that have contrasting size (2 and 40 μm), the simulated surface Chl-*a* and simulated OC3M Chl-*a* data streams provide distinct information for the large and small phytoplankton dynamics respectively. Indeed, whereas the simulated surface Chl-*a* better constrains parameters affecting the large phytoplankton dynamics, simulated OC3M Chl-*a* better constrains parameters affecting the small phytoplankton. While our model setup may be simplified compared to natural systems in that we only have two sizes of phytoplankton, it raises an important issue about the role of size on the conversion of remotely sensed reflectance to a chlorophyll-*a* product.

3.7 Acknowledgments

This research was supported under the Australian Research Council's Discovery Projects funding scheme (DP140101340 to MD and RM). Furthermore, we would like to thank NASA for the production and distribution of the chlorophyll-*a* product as well as the OC3M algorithm. Data presented in Figure 3.2 were sourced from the Integrated Marine Observing System (IMOS), an initiative of the Australian Government being conducted as part of the National Collaborative Research Infrastructure Strategy and the Super Science Initiative. Finally, we would like to acknowledge the valuable reviews provide by the four anonymous reviewers, which has helped improve the clarity and focus of the manuscript.

CHAPTER 4

Comparing size fractionated *in situ* chlorophyll-*a* measurements with a satellite ocean colour product in Eastern Australian open ocean waters

Leonardo Laiolo[1, 2], Richard Matear[2], Monika Soja-Woźniak[2], David Suggett[1], David Hughes[1], Mark E. Baird[2], Martina A. Doblin[1]

[1]Climate Change Cluster, University of Technology Sydney, 8-15 Broadway, Ultimo, NSW, 2007, Australia

[2]CSIRO Oceans and Atmosphere, Hobart, 3-4 Castray Esplanade, TAS, 7004, Australia

4.1 Abstract

The distribution of phytoplankton shows high spatial and temporal variability. Chlorophyll-*a* concentration (Chl-*a*) derived from satellite remote sensing reflects both real phytoplankton variability and inherent uncertainties. Ocean colour data are commonly used to calibrate marine biogeochemical models; therefore, understanding the distribution of errors in the remotely sensed Chl-*a* product is critical. Here, we explore the relationship between phytoplankton size structure and an ocean colour product (GlobColour) using both *in situ* observations and model simulation scenarios. We focused on the offshore eastern Australian ocean region, largely characterised by oligotrophic waters in which phytoplankton primarily define the optical properties of the water column. In this region, size-fractionated Chl-*a* samples were collected from several water masses to investigate the phytoplankton size contribution (i.e., < 2 μm, 2 - 10 μm and > 10 μm) to the total Chl-*a*. Of the 36 stations sampled, a total of ten *in situ* size fractionated Chl-*a* measurements were matched-up with the corresponding clear-sky satellite Chl-*a* product. Weighted linear regression analyses were performed to relate the *in situ* sampled phytoplankton size structure to the corresponding ocean colour product. The matched-up points revealed a systematic underestimation of *in situ* Chl-*a*, which appeared to be related to the abundance phytoplankton bigger than 10 μm. Using an optical model, we explore how phytoplankton cell size influences the absorption and backscattering coefficients and the implication this has for water leaving radiance and the estimated Chl-*a* derived from satellite ocean colour. Consistent with the linear regression analyses, the optical model shows phytoplankton cell size has a significant impact on the remote-sensing reflectance with a 10 μm cell producing about half the ocean colour Chl-*a* as the 1 μm cell. Thus, increases in the abundance of large sized phytoplankton cause a significant increase in uncertainty in ocean colour products, with obvious implications for accurate estimates of regional primary productivity.

4.2 Introduction

The modern understanding of the global distribution and seasonal dynamics of phytoplankton comes largely from satellite observations. The spatial and temporal resolutions of remotely-sensed observations make these data particularly suitable for modelling physical and biological ocean dynamics. Specifically, chlorophyll-*a* concentration (Chl-*a*) is the most commonly derived product used to understand bio-physical interactions, exploring surface ocean circulation patterns (Barton, 2002; Pegau et al., 2002) and phytoplankton seasonal dynamics through data assimilation analyses (Hemmings et al., 2003; Laiolo et al., 2016). Furthermore, remotely sensed Chl-*a* products represent the key element to quantify ocean primary production (Behrenfeld, 2001; Campbell et al., 2002; Carr et al., 2006; Longhurst et al., 1995).

Remote sensors are not able to measure Chl-*a* directly (Robinson, 2004). Instead, they measure the total atmospheric radiance and the water-leaving radiances that contains information about the phytoplankton community (e.g., Schroeder et al., 2007). Scattering and absorption properties of water, dissolved matter, and suspended particles (that collectively comprise seawater) determine the inherent optical properties (IOPs) of the water column, which in turn define the apparent optical properties (AOPs) (e.g., Cherukuru et al., 2016; Dickey et al., 2006). Then, algorithms derived from empirical relationships between *in situ* observations and *in situ* reflectances are applyied to the remote-sensing reflectance (R_{rs}) measured by the satellite sensors. Thanks to this relationships it is possible to estimate the Chl-*a* in the upper ocean (O'Reilly et al., 1998).

In open ocean waters, as classified by Morel and Prieur (1977), the suspended matter that influences the water leaving radiance is mainly composed of phytoplankton, heterotrophic organisms, viruses and organic detritus (Mobley et al., 2004). In these waters, absorption and scattering/backscattering are mainly functions of the total abundance, morphology, size and pigment composition of the microbial community

(Gordon and Morel, 1983; Morel and Prieur, 1977; Mobley et al., 2004). Therefore, the IOPs of Case I waters are primarily related to phytoplankton concentration and composition (Mobley et al., 2004). Specifically, the phytoplankton cell size has a crucial impact on the light absorption efficiency and consequently on the IOPs of the water column in Case I waters. Bigger photosynthetic cells show a lower absorption coefficient due to the packaging of pigments relative to the energy impinging on the geometric cross-section of the cell (Astoreca et al., 2012; Bricaud, 2004; Ciotti and Bricaud, 2006; Ciotti et al., 2002). Therefore, this phenomenon (referred to as the packaging effect) can increase the error of estimated Chl-*a* concentration from remote-sensing reflectance (Marra et al., 2007; Mouw et al., 2012; Chapter 3).

Oligotrophic ecosystems are representative of Case I waters with a phytoplankton community typically composed of small photosynthetic cells (Partensky et al., 1999). In open ocean, as well as coastal waters, phytoplankton concentration and composition are largely driven by physical events (Levy and Klein, 2004). Different upwelling, downwelling and mixing phenomena can lead to changes in resources needed for phytoplankton growth, which in turn influences Chl-*a* concentration, phytoplankton abundance and composition (Officer and Ryther, 1980; Pitcher et al., 1991; Tilburg et al., 2002). Specifically, even in oligotrophic offshore waters, mesoscale features such as cyclonic eddies can provide favourable conditions for the growth of larger phytoplankton (e.g., diatoms) in regions usually dominated by small photosynthetic cells (e.g., as *Prochlorococcus* and *Synechococcus*) (Brown et al., 2008; Doblin et al., 2016; Laiolo et al., 2016; McGillicuddy and Robinson, 1998; Rodriguez et al., 2003; Vaillancourt et al., 2003). Large phytoplankton cells (such as some diatoms) prefer low light environments, utilise new nutrients efficiently and sink rapidly (Finkel et al., 2009). Therefore, phytoplankton communities dominated by large phytoplankton cells are usually characterized by high export efficiency (Mouw et al., 2016). In contrast, small sized phytoplankton like *Prochlorococcus* and *Synechococcus* do

not have significant sinking rates and prefer stratified waters with high light conditions. Thus, they are mostly involved in regeneration and recycling processes (Falkowski et al., 1998). This results in a lower export efficiency (Mouw et al., 2016). Hence, information about the size distribution of phytoplankton and its dynamics is crucial for understanding the biogeochemistry and ecology of open ocean waters (Guidi et al., 2015; Mouw et al., 2016). Increases in Chl-*a* are usually related to enhanced phytoplankton biomass. The conceptual model in Figure 4.1 represents a range of different scenarios for increases in Chl-*a* concentration. Indeed, increased Chl-*a* concentrations can be related to higher abundance of the identical phytoplankton cells (Fig. 4.1a), or can involve a shift in the size structure of the phytoplankton community while maintaining the same intracellular Chl-*a* (Fig. 4.1b). Furthermore, phytoplankton can regulate the intracellular pigment amounts (e.g., Chl-*a*) as a response to changes in irradiance conditions, through a process called 'photoacclimation', a short-term response to changes in light intensity (Moore et al., 2006; Dubinsky and Stambler, 2009). For instance, a decline in the light intensity can cause an increase in the intracellular Chl-*a*, an effect that is sometimes referred to as 'greening' (Fig. 4.1c)". In oligotrophic waters, nutrient injections into the euphotic zone cause increases in Chl-*a*, normally associated with an increased proportion of larger phytoplankton cells (e.g., Mouw et al., 2012; Doblin et al. 2016). Hence, the lower absorption coefficients that characterize large photosynthetic cells (due to the packaging effect) could cause a greater uncertainty in the remotely sensed Chl-*a* product (e.g., Marra et al., 2007; Mouw et al., 2012).

In this study we compare *in situ* size fractionated Chl-*a* observations (hereafter referred to as *in situ* Chl-*a*) with the GlobColour Chl-*a* product (hereafter referred to as satellite Chl-*a*), to explore the uncertainty associated with the remotely sensed Chl-*a* and the phytoplankton size structure. GlobColour is an ocean color product particularly suitable for data assimilation, because it combines outputs from SeaWiFS (NASA), MODIS (NASA), MERIS (ESA), OLCI (ESA) and

VIIRS (NOAA/NASA) to create a continuous time series from 1997 to the present (http://hermes.acri.fr/index.php?class=archive).

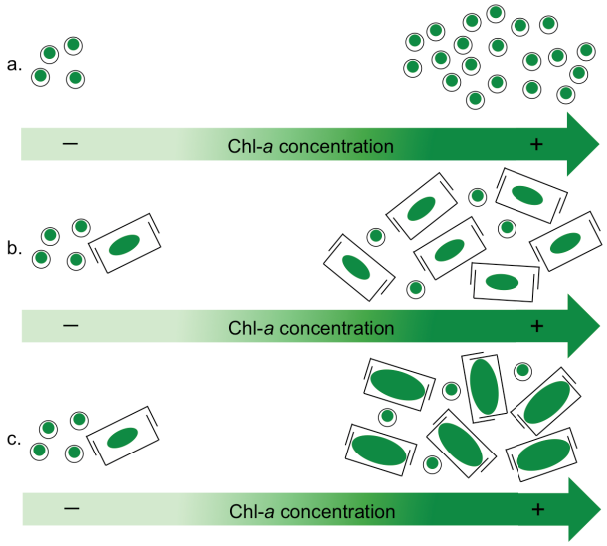

Figure 4.1 Different scenarios showing phytoplankton abundance (a), size structure (b) and pigment content changes (c) related to increased Chl-*a*.

4.3 Materials and Methods

4.3.1 Area of the study

The area selected for this study is located in the south western Pacific, between 30°S to 40°S and 150°E to 160°E (Fig. 4.2a). The physical and biological characteristics of this area are strongly influenced by the East Australian Current (EAC), which represents the major western boundary current of the South Pacific sub-tropical gyre (Mata et al., 2000; Ridgway and Dunn, 2003). The EAC originates from the warm oligotrophic waters of the Coral Sea and flows southward along the East Australian coast. The open ocean waters in this area are usually characterised by low nutrient concentrations and low phytoplankton biomass (Oke and Griffin, 2011). Despite this, nutrient enrichment and consequent phytoplankton growth occur as a response to occasional upwelling-favourable wind events, the formation of cyclonic eddies, the separation of the EAC from the shelf and the flow of the EAC along the Tasman Front, uplifting nutrient-rich water (Godfrey et al., 1980; Roughan and Middleton, 2002; Tranter et al., 1986).

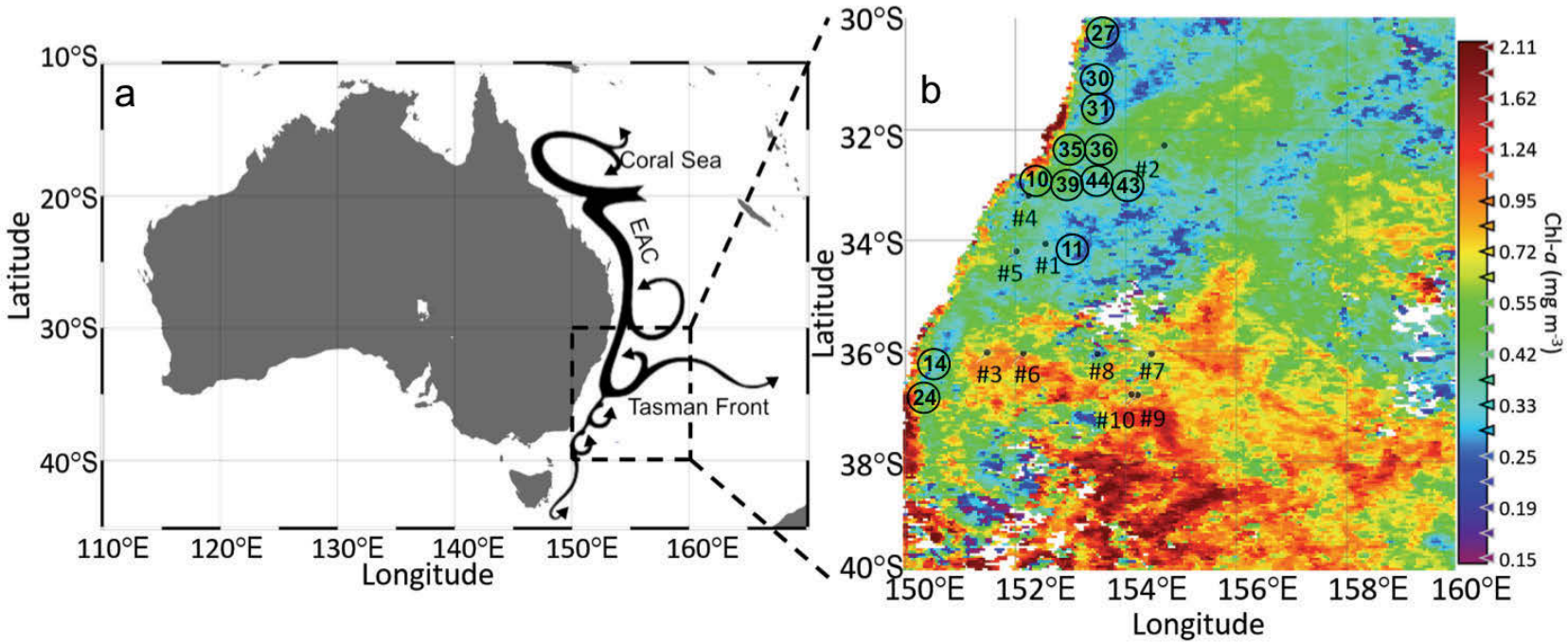

Figure 4.2 (a) The Australian region and physical features that characterise eastern Australian waters. The study area is highlighted by the dashed line (150° E – 160° E; 30° S – 40° S). **(b)** Location of the match-up points # (Table 4.1) are represented by #, while non match-up points are represented by CTD # (Table 4.2) inside circles. The background is a Globcolour Chl-*a* (mg m^{-3}) satellite field averaged from the 31st August to 16th September 2016. White areas indicate land or no data.

When these physical events occur in oligotrophic regions, as in the east Australian domain selected for this study, they usually cause a shift from a phytoplankton community dominated by small cells to a community dominated by large cells (Brown et al., 2008; Olaizola et al., 1993; Rodriguez et al., 2003; Vaillancourt et al., 2003). This trend is evident in Figure 4.2. Indeed, the highest Chl-*a* concentrations are generally located in proximity of the Tasman front (i.e., match-up points # 7, 8, 9 and 10) or close to the East Australian coast (i.e., CTD # 10, 14 and 24). Furthermore, these match-up and CTD # points correspond to the highest large phytoplankton cells contributions to the total *in situ* chlorophyll-*a* (Table 4.2 and Fig. 4.3a).

4.3.2 *In situ* size fractionated chlorophyll-*a* measurements

To explore the impact of phytoplankton size on the uncertainty in the Chl-*a* satellite product, *in situ* size fractionated Chl-*a* measurements were collected on board the *RV Investigator* during austral spring (voyage IN2016_V04). Water collection sites (i.e., CTD locations) and dates are shown in Table 4.1.

Table 4.1 Details about the match-up points, CTD number (CTD #), *in situ* sampling time, location and total Chl-*a* (TChl-*a in situ*). The averaged Chl-*a* from satellite measurements (Avg Chl-*a* satellite), the corresponding standard deviation (SD), the coefficient of variation (CV) and number of satellite observations (i.e., pixels averaged) are shown in the last columns.

Match-up point #	CTD #	Date dd/mm/yyyy	Time hr:min	Lat	Long	TChl-*a in situ* (mg m^{-3})	Avg Chl-*a* satellite (mg m^{-3})	SD	CV	n
1	3	31/08/2016	23:06	-34.265	152.326	0.45	0.3801	0.0223	0.06	6
2	42	16/09/2016	19:56	-32.477	154.480	0.55	0.2748	0.1012	0.37	5
3	15	6/09/2016	01:26	-36.227	151.267	0.57	0.4758	0.0598	0.13	9
4	9	1/09/2016	19:54	-33.391	152.023	0.61	0.3615	0.0243	0.07	9
5	5	1/09/2016	05:37	-34.400	151.803	1.04	0.5868	0.0215	0.04	6
6	16	6/09/2016	09:21	-36.247	151.928	1.11	0.8839	0.087	0.10	4
7	18	7/09/2016	02:48	-36.251	154.249	1.42	0.9781	-	-	1
8	17	6/09/2016	18:37	-36.251	153.268	1.52	0.5668	0.0605	0.11	6
9	19	7/09/2016	10:03	-37.000	153.998	2.23	1.56	0.0749	0.05	4
10	22	8/09/2016	01:05	-36.986	153.885	3.5	1.89	-	-	1

Table 4.2 Details about the stations sampled that have no corresponding satellite match-up measurements. The table shows CTD number (CTD #), *in situ* sampling time, location, site and total Chl-*a* (TChl-*a in situ*). The contribution to the TChl-*a in situ* from the three different phytoplankton size classes (i.e., Small <2, Medium between 2 µm and 10 µm and Large >10 µm) is represented in percentages in the last columns. The "Site" column indicates stations near the continental shelf (c.s.) and off-shore stations (o.s.).

							Phytoplankton composition		
CTD #	Date dd/mm/yyyy	Time hr:m	Lat	Long	Site	TChl-*a in situ* (mg m^{-3})	Small	Medium	Large
30	14/09/2016	7:00	-31.502	153.328	o.s.	0.24	63%	29%	8%
11	4/09/2016	8:50	-34.123	153.235	o.s.	0.38	13%	71%	16%
35	15/09/2016	7:00	-32.475	153.164	o.s.	0.43	42%	44%	14%
39	16/09/2016	6:15	-32.999	152.913	o.s.	0.43	42%	39%	19%
36	15/09/2016	12:00	-32.566	153.118	o.s.	0.47	30%	38%	32%
14	6/09/2016	6:00	-36.255	150.291	c.s.	0.48	8%	29%	63%
43	17/09/2016	9:45	-32.472	154.102	o.s.	0.54	19%	72%	9%
27	13/09/2016	10:45	-30.628	153.627	c.s.	0.68	24%	20%	56%
44	17/09/2016	14:30	-32.464	153.704	o.s.	0.69	13%	30%	57%
31	14/09/2016	11:45	-31.643	153.319	c.s.	0.86	12%	22%	66%
10	2/09/2016	13:30	-33.005	152.458	c.s.	1.51	5%	53%	42%
24	10/09/2016	8:30	-36.482	150.288	c.s.	3.81	4%	20%	76%

Surface water (i.e., 5 to 10 m depth) was sampled from the CTD-rosette and transferred into acid-cleaned 20 L polycarbonate vessels. Directly on board, 250 mL of water per sample was then filtered in parallel through three independent filters: (1) 25 mm glass fiber filters with nominal pore size of 0.3 µm (Sterlitech, USA) and (2) 2.0 µm (Microanalytix, Australia); as well as (3) a 25 mm polycarbonate membrane with pore size of 10 µm (Merck Millipore, USA). Each of three filters was then placed into an individual 20 mL glass scintillation vial containing 1.5 mL of 90% acetone. Pigments were extracted at 4°C overnight in the dark. Chlorophyll-*a* concentrations were determined on board using a calibrated fluorometer (Chlorophyll-*a* Non Acidified module; Trilogy, Turner Design, USA). Assuming the Chl-*a* determined from the 0.3 µm filter represented the total Chl-*a*, the proportion of three phytoplankton size classes (0.3 to 2.0, 2.0 to 10, > 10 µm) were estimated using the following approach:

$$\text{Chl-}a_{sml} = \frac{\text{TChl}a - \text{Chl}a_{2.0}}{\text{TChl}a} \cdot 100 \quad (1)$$

$$\text{Chl-}a_{med} = \frac{\text{Chl}a_{2.0} - \text{Chl}a_{10.0}}{\text{TChl}a} \cdot 100 \quad (2)$$

$$\text{Chl-}a_{lrg} = 100 - \left(\text{Chl-}a_{sml} + \text{Chl-}a_{med}\right) \quad (3)$$

where Chl-a_{sml}, Chl-a_{med} and Chl-a_{lrg} represent the percentage of Chl-*a* concentration in the small (< 2 µm), medium (between 2 and 10 µm) and large (> 10 µm) phytoplankton classes for every surface water sample. TChl*a* is the total Chl-*a*, Chl-$a_{2.0}$ is Chl-*a* of phytoplankton cells larger than 2 µm and Chl$a_{10.0}$ is Chl-*a* of phytoplankton cells larger than 10 µm. Hereafter the three phytoplankton classes will be referred as “small phytoplankton” (< 2 µm), “medium phytoplankton” (between 2 µm and 10 µm) and “large phytoplankton” (> 10 µm).

4.3.3 Ocean colour observations

Satellite-derived Chl-*a* estimates downloaded from GlobColour (http://hermes.acri.fr/index.php?class=archive) were used. The GlobColour merged Chl-*a* product was generated by the use of the GSM model (see Maritorena and Siegel, 2005) from only MODIS and VIIRS data for the selected period (i.e., 31st August 2016 – 8th September 2016). It is a daily

product with a spatial resolution of 4 km.

We have chosen the GlobColour Chl-*a* product because it ensures data continuity, improves spatial and temporal coverage and reduces noise relative to other ocean colour products derived from one radiometer (ACRI- ST GlobColour Team et al., 2015). *In situ* size fractionated Chl-a measurements were compared with co-located satellite data collected 24 hours either side of the *in situ* sample. While the temporal match up comprised a 1-day window, the spatial matchup involved averaging the Chl-*a* satellite observations from the area of 9 pixels around the CTD location (3x3 window size).

4.3.4 Satellite Chl-*a* product and *in situ* Chl-*a* measurements comparison

The number of match-up points between satellite and *in situ* data was limited to ten due to cloud cover over the study region during the oceanographic voyage. The match-up points were ranked according to the total *in situ* Chl-*a*, from the lowest to the highest concentration (Table 4.1). To assess the accuracy of satellite Chl-*a* estimates, the satellite Chl-*a* product was directly compared with the TChl*a* measurements (i.e., total *in situ* Chl-*a*) through a linear regression analysis, defined as “regression model A”. Furthermore, to investigate the relationship between phytoplankton < 10 µm with the satellite Chl-*a* product, the *in situ* Chl-*a* associated with the large phytoplankton class (> 10 µm) was excluded from the linear regression analysis, defined as “regression model B”. Then, the relationship between satellite Chl-*a* and size fractionated *in situ* Chl-*a* values was explored. Weighted linear regression analyses were performed with the purpose of optimising the values of *in situ* size fractionated Chl-*a*, to obtain the least squares best fit with the satellite Chl-*a*. First, this analysis was used to determine the weights for the small (< 2 µm), medium (between 2 µm and 10 µm) and large (> 10 µm) phytoplankton class (regression model C). Then, the weighted linear regression was used to determine the relationship between phytoplankton smaller than 10 µm with the satellite Chl-*a* product, thus excluding the

large (> 10 μm) phytoplankton class (regression model D). To perform the linear regression analyses described above, we used the 'numpy.linalg.svd' function from the software Python (i.e., singular values decomposition analysis). Then, we used the 'scipy.stats.linregress' Python function to calculate the linear least-squares regression for the two sets of measurements. Statistical significance was tested against a slope of 1:

$$t\text{-}statistic = \frac{(RS-1)}{SE} \quad (5)$$

where SE represents the standard error and RS represents the regression slope, the degrees of freedom were equal to 8 (i.e. match-up points – 2) .

4.3.5 Optical model

To explore the impact of phytoplankton size and cell abundance on absorption, backscattering and consequent R_{rs}, we used the optical model proposed by Baird et al. (2016). The performance of this optical model has been previously assessed with MODIS R_{rs} in the Great Barrier Reef region (Baird et al., 2016). The optical model first, based on variables and parameters (Chl-*a* concentration and cells dimension), solves for the IOPs (absorption, scattering and backscattering) of seawater and constituent phytoplankton cells. Then, based on IOPs, the optical model solves for the R_{rs}, calculated through the relationship with scattering coefficient in a backward direction (backscattering coefficient, b_b) and the absorption coefficient (a) (i.e., $R_{rs} \propto \frac{b_b}{a+b_b}$) (Baird et al., 2016). Details about the optical model calculations of IOPs and R_{rs} are given in Appendix 1. We did not consider absorption and backscattering of coloured dissolved organic matter (CDOM) or non-algal particulates (NAP) because we focussed on Case 1 water, where phytoplankton is the main constituent responsible for variations in optical properties, apart from water itself (Gordon and Morel 1983; Mobley et al., 2004; Morel and Prieur, 1977). Experiments were performed to explore a range of possible scenarios consistent with real world scenarios, involving different Chl-*a* concentrations (0.2, 1 and 3 mg m^{-3}), phytoplankton sizes (from 1 to 50 μm), phytoplankton cell abundance (from 5 x 10^2 to 7 x 10^9 cells L^{-1}) and four different C:Chl-*a* (from 20:1 to 150:1).

The R_{rs} obtained from the optical simulations was then used to produce a satellite-like estimate of Chl-*a*, following the OC3M algorithm (https://oceancolor.gsfc.nasa.gov/atbd/chlor_a/#sec_2; O'Reilly et al., 1998). The product we obtained was used to explore the simulated impact of phytoplankton size and cell abundance on a widely used satellite Chl-*a* product (i.e., MODIS OC3). The NASA OC3M algorithm consists of a fourth-order polynomial relationship between the logarithms of R_{rs} ratios and Chl-*a*:

$$\log_{10}(\text{Chl-}a) = a_0 + \sum_{i=1}^{4} a_i \left(\log_{10}\left(\frac{\max(R_{rs}(443),\ R_{rs}(488))}{R_{rs}(551)}\right)\right)^i \qquad (6)$$

where a_i is a sensor specific coefficient (MODIS: a_0= 0.2424, a_1=-2.7423, a_2=1.8017, a_3=0.0015, a_4=-1.2280), $R_{rs}(443)$, $R_{rs}(488)$ and $R_{rs}(551)$ represent remote sensing reflectance at 443 nm, 488 nm and 551 nm respectively.

4.4. Results

4.4.1 Comparison between satellite Chl-*a* product and *in situ* Chl-*a* measurements

From a total of 52 *in situ* Chl-*a* samples, there were ten stations for which there was cloud-free satellite ocean colour data. The ten match-up points are representative of different Chl-*a* concentrations and distinct phytoplankton community size structures. Specifically, match-up points include low *in situ* Chl-*a* concentrations, ranging from 0.4 to 0.6 μg L^{-1} (points 1-4), intermediate values, from 1.0 to 1.4 μg L^{-1} (points 5-7), to high *in situ* Chl-*a* concentration measurements, ranging from 1.5 to 3.5 μg L^{-1} (points 8-10) (Fig. 4.3). While match-up points 1 to 7 were dominated by phytoplankton smaller than 10 μm (i.e., 79% to 98% of the total *in situ* Chl-*a* concentration), large phytoplankton made a significant contribution to the total Chl-*a* (i.e., 48% to 77%) for match-up points 8, 9 and 10. The direct comparison between satellite and *in situ* Chl-*a* reveals a consistent satellite Chl-*a* product underestimation of *in situ* Chl-*a* concentrations - all ten match-up points are located below the 1:1 line (Fig. 4.3b). From the points that occurred outside the uncertainty interval, points 8 and 10 correspond to those with the highest error and the largest amount of Chl-*a*

associated with the large phytoplankton class (Fig. 4.3a and b; 77% and 55% respectively).

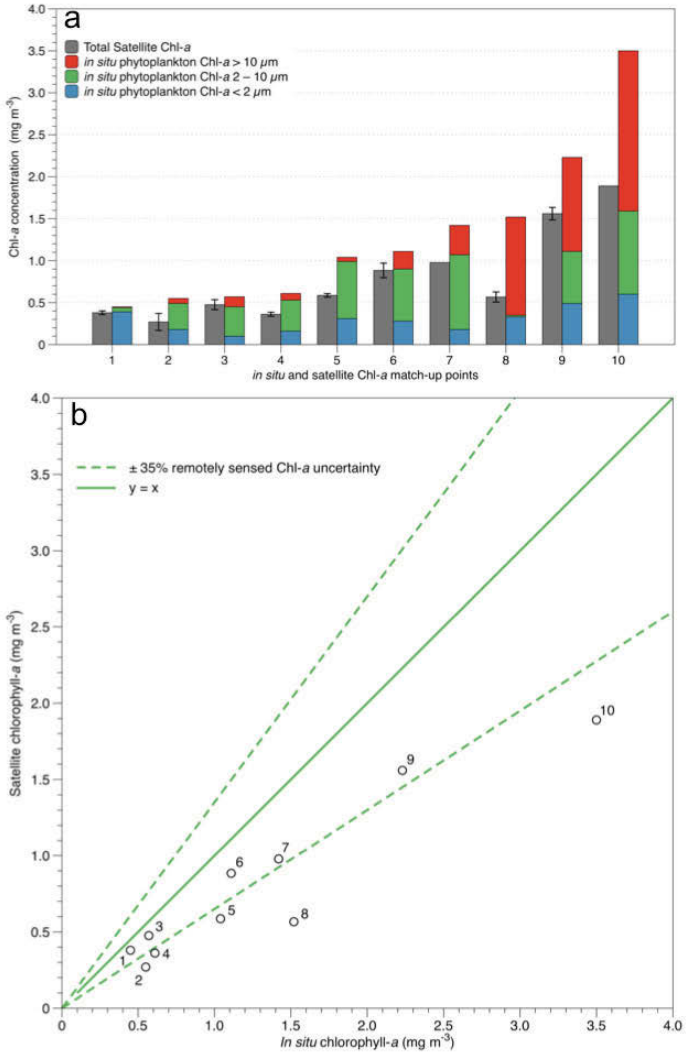

Figure 4.3 Comparison between *in situ* and satellite Chl-*a* match-up points. (a) Comparison between the size fractionated Chl-*a* and the satellite Chl-*a* through bar charts. While grey bars represent the satellite Chl-*a*, the narrow blue, green and red bars show the *in situ* Chl-*a* for the small (< 2 µm), medium (between 2 to 10 µm) and large (> 10 µm) phytoplankton class respectively. Errors bars represent the standard deviation in the 3x3 pixel box that has been used for the matchup with the *in situ* Chl-*a*. (b) Relationship between total *in situ* Chl-*a* and satellite Chl-*a*. The green solid line indicates a 1:1 relationship and dashed green lines show the ± 35% uncertainty interval.

First, we compare the total *in situ* Chl-*a* to satellite Chl-*a* (i.e., regression model A; Fig. 4.4a, red dots and regression line). This analysis

resulted in a linear relationship (R^2 = 0.87) with the satellite Chl-*a* only detecting 0.55 of total *in situ* Chl-*a* (Table 4.3). Significant differences where found between a slope of 1 and the data points of the regression model A (Table 4.3, $P < 0.001$). After weighted values were given to all three phytoplankton classes, regression model C improved the fit of regression model A, from R^2 = 0.87 to R^2 = 0.93 (Fig. 4.4a; Table 4.3). In this case, the large phytoplankton class needed the most significant correction (i.e., weighted value = 0.35, where 1.00 indicates the *in situ* Chl-*a* is consistent with the satellite estimate) to fit to the satellite Chl-*a* (Table 4.3).

Then, the regression analyses were performed excluding the Chl-*a* concentration values associated with the large phytoplankton class (i.e., red bars in Fig. 4c; regression analyse represented in Fig. 4.4b). The direct comparison between *in situ* Chl-*a* values and satellite Chl-*a* showed the linear relationship improved slightly from regression model A (from R^2 = 0.87 to R^2 = 0.89) (Table 4.3). In this case, the slope of the regression line obtained was already close to 1 before weights were given to the *in situ* Chl-*a* associated with the small and large phytoplankton classes (i.e., $y = 1.2x – 0.17$; $P > 0.05$; Fig 4.4b, Table 4.3). After weighted values were given to the small and medium phytoplankton classes (regression model D) the linear regression showed a slight improvement from R^2 = 0.89 (i.e., regression model B) to R^2 = 0.91 (Fig. 4.4b, Table 4.3). No significant differences were found between data points from regression model B, C and D and a slope of 1 (Table 4.3).

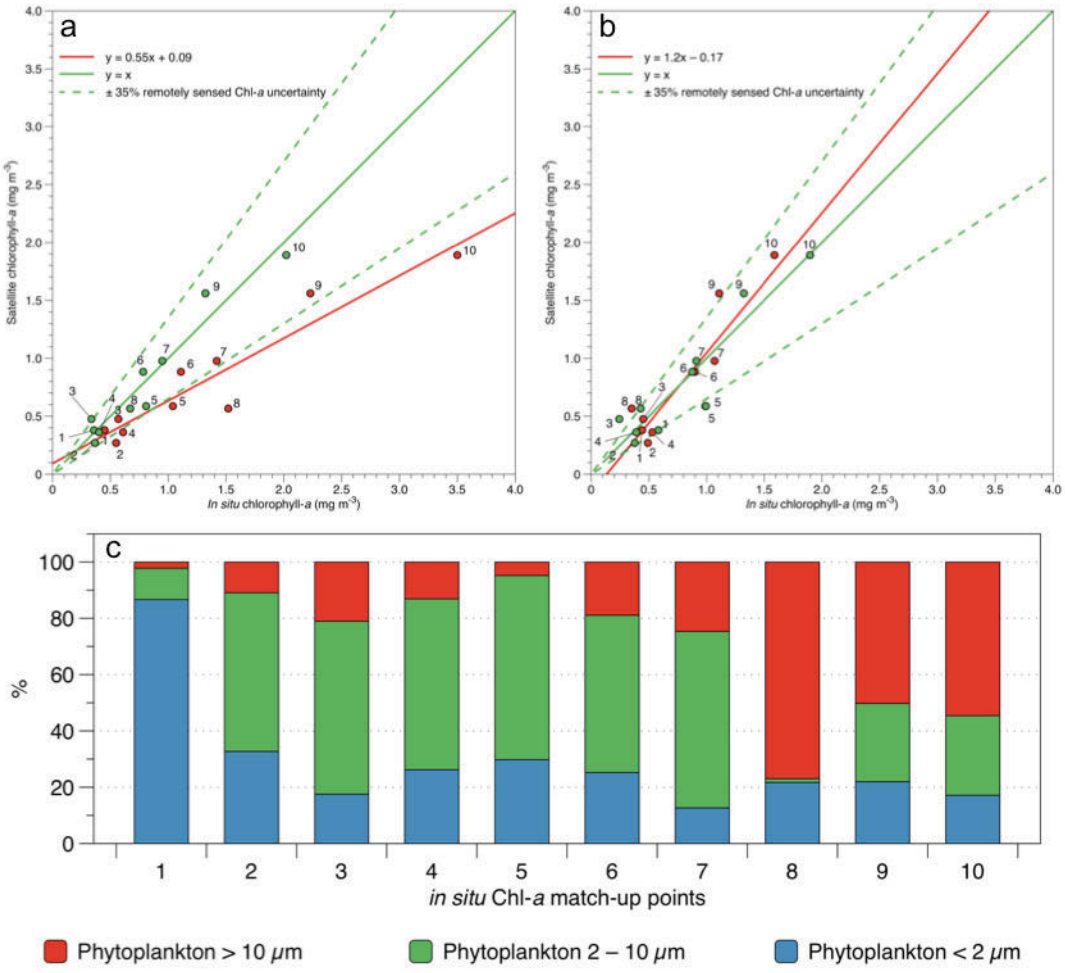

Figure 4.4 Relationship between *in situ* Chl-*a* and satellite Chl-*a*. Red dots and corresponding red linear regression lines represent the direct comparison between *in situ* Chl-*a* vs satellites Chl-*a*. The green dots and lines show the linear fit to the remotely sensed Chl-*a* where a different weighting is given for the *in situ* Chl-*a* associated with small, medium and large phytoplankton. Panel (a) shows regression model A in red font and regression model C in green font. The regression model B (in red) and regression model D (in green) are represented in panel (b). (c) The bar chart shows the size distribution (%) of the phytoplankton community for every match-up point. Match-up point's numbers correspond to numbers in Table 4.1 and Fig. 4.2.

Table 4.3

Weighting applied to the *in situ* size-fractionated Chl-*a* to produce the least squares best fit to the satellite Chl-*a* values. A measure of the fit is given by R^2 values. While x corresponds to the in situ observations and y to the corresponding satellite Chl-*a*. P represents *p*-values obtained testing the data against a slope of 1, Eq. (5).

Regression model #	Weighted values			Regr. line equation	R^2	*p*-values
	Small phytoplankton	Medium phytoplankton	Large phytoplankton			
A	-	-	-	y = 0.55x + 0.09	0.87	< 0.001
B	-	-	-	y = 1.2x – 0.17	0.89	> 0.05
C	1.07	0.83	0.35	y = x	0.93	> 0.05
D	1.78	0.92	-	y = x	0.91	> 0.05

4.4.2 Optical model simulations

Several scenarios involving different Chl-*a* concentrations, phytoplankton abundances and sizes were used to assess their effect on absorption (*a*), backscattering (b_b) and remote sensing reflectance (R_{rs}). Figure 4.5 shows the optical model results associated with these simulated scenarios. The three columns of the figure represent scenarios characterised by 0.2, 1.0 and 3.0 mg m^{-3} of Chl-*a* in pure sea water (i.e., no CDOM or NAP). The rows show bio-optical properties as a function of increasing phytoplankton cell dimensions (Fig. 4.5). Specifically, the first and the second row represents *a* and b_b coefficients at 443 nm, respectively, the third and fourth row shows the R_{rs} at 443 nm and 551 nm respectively (Fig. 4.5). The last row is showing the corresponding satellite-like estimate of Chl-*a*, calculated using Eq. (5). In every plot, different ratios of total phytoplankton Carbon (C) to Chl-*a* are represented by the black (20:1), red (50:1), green (100:1) and blue (150:1) lines; the corresponding phytoplankton abundances (cells L^{-1}) are shown at the bottom of the figure with the same colour scheme. The cell concentration is increasing gradually for the same phytoplankton dimensions, from the C:Chl-*a* 20:1 (lowest abundance of cells) to 150:1 (highest abundance of cells). Furthermore, to highlight the phytoplankton size impact on the simulated satellite-like Chl-*a*, the results from Figure 4.5q were normalised by the smaller phytoplankton class Chl-*a* values (Fig. 4.6).

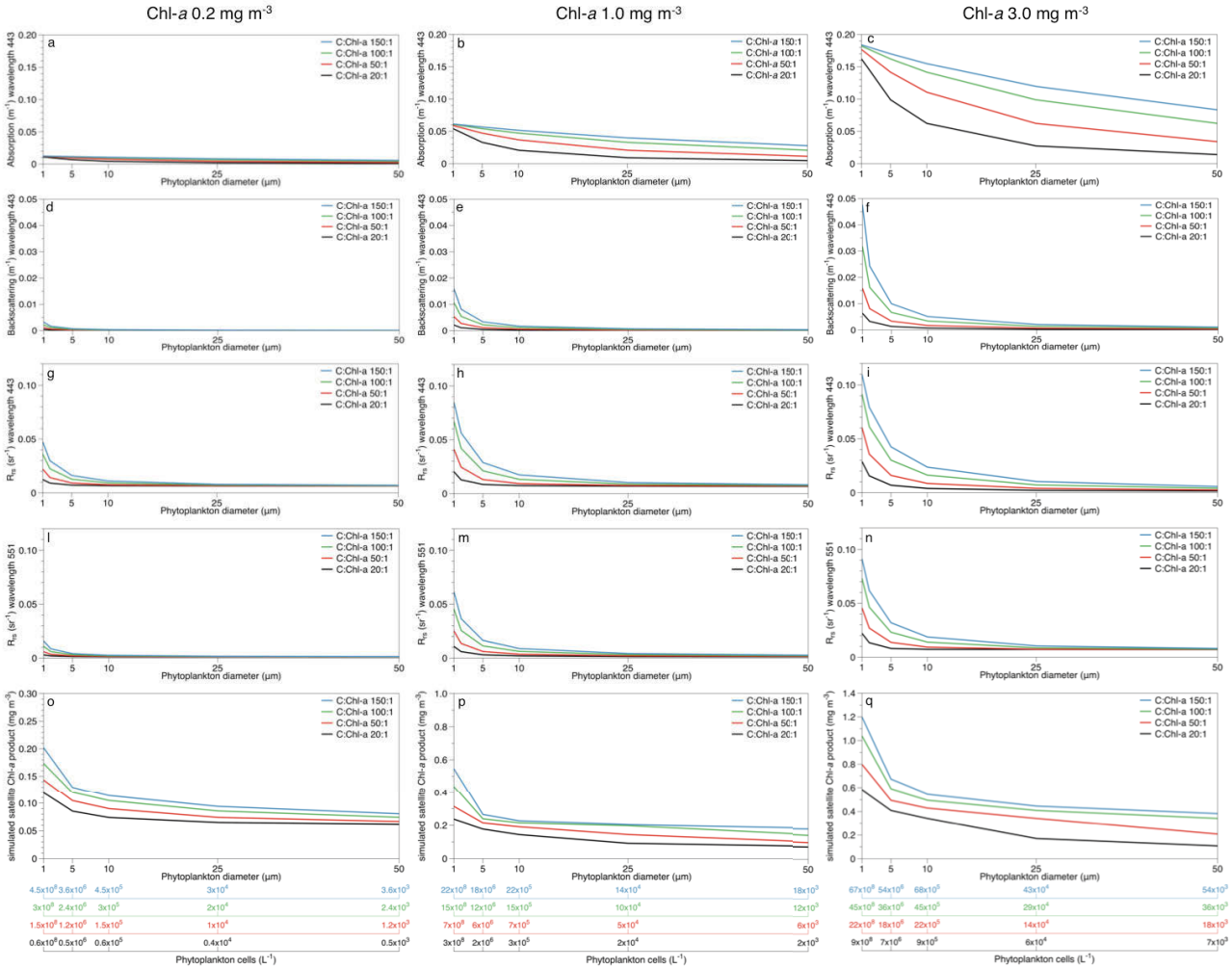

Figure 4.5 Bio-optical properties in different simulated scenarios obtained through the optical model (Baird et al., 2016). The three columns represent three different Chl-*a* concentration, 0.2, 1.0 and 3.0 mg m^{-3} respectively. The first three rows show the corresponding absorption, backscattering and R_{rs} for the wavelength 443 nm in function of increasing phytoplankton sizes, while the fourth row shows the R_{rs} for the wavelength 551 nm. The last row is showing the simulated satellite-like Chl-*a* product. Different ratios of phytoplankton Carbon (C) to Chl-*a* are represented in black (20:1), red (50:1), green (100:1) and blue (150:1) lines. Correspondent phytoplankton abundances (cells L^{-1}) are shown at the bottom of the figure with the same colour scheme.

Results from optical simulations show increased absorption coefficients for higher Chl-*a* and phytoplankton abundance (i.e., comparing different cell abundance with same diameter of phytoplankton cells, Fig. 4.5a – c). In the optical model, the backscattering coefficient only depends on phytoplankton cell dimension and abundance (e.g., backscattering coefficient of 0.19 m^{-1} for either 1 or 3 mg m^{-3} Chl-*a*, computed from 22 x 10^8 phytoplankton cells per L^{-1} with 1 µm cell diameter; Fig. 4.5e and f). Indeed, for the same size of phytoplankton, higher cell concentrations caused an increased backscattering coefficient (Fig. 4.5d – f). On the other hand, the absorption and backscattering coefficients decrease with increasing phytoplankton cell dimension (Fig. 4.5a – f, evident in panel c and f). In particular, the optical model simulations suggest phytoplankton cells between 1 to 10 µm diameter cause an exponential decrease in the backscattering coefficient at 443 nm (Fig. 4.5d – f, evident in in panel f).

In the optical simulations, the R_{rs} at 443 and 551 nm varies accordingly to the absorption and backscattering coefficients. Specifically, the R_{rs} signal increases with higher Chl-*a* concentrations and phytoplankton cell abundance (Fig. 4.5g – n). Conversely, larger phytoplankton cells between 1 to 10 µm in diameter cause an exponential drop of the R_{rs} signal at both 443 nm (Fig. 4.5g – i) and 551 nm (Fig. 4.5l – n) wavelengths, consistent with the backscattering pattern (Fig. 5d – f). Simulations show that increases in the R_{rs} signal are not proportional to the increasing Chl-*a* scenarios considered (Fig. 4.5g – i) and vary between considered wavelengths. The calculation of the satellite-like estimate of Chl-*a* using the OC3M algorithm Eq. (6), produced a stronger underestimation of Chl-*a* concentration for scenarios with higher values of Chl-*a* (Fig. 4.5o – q).

4.5 Discussion

The comparison between *in situ* size fractionated Chl-*a* measurements and remotely sensed Chl-*a*, allowed us to assess the satellite Chl-*a* product in open ocean water of East Australia and investigate relationships between three phytoplankton size classes and

the satellite Chl-*a* product. Furthermore, the impact of phytoplankton size and abundance on a, b_b, R_{rs} and a satellite-like estimate of the Chl-*a* product (MODIS) was explored through the optical model simulations (Baird et al. 2016).

The direct comparison between *in situ* and satellite Chl-*a* observations revealed an underestimation of the ocean colour product for all ten match-up points (Fig. 4.3). This inconsistency appears to be greater for higher Chl-*a* concentrations, between 1.5 and 3 mg m^{-3} (Fig. 4.3a). The size fractionated Chl-*a* measurements highlight that higher Chl-*a* values are related to an increased contribution of large phytoplankton cells to the total Chl-*a* (Fig. 4.3a) – i.e., the size classes don't scale linearly. This behaviour is consistent with phytoplankton dynamics typical of oligotrophic environments, where seasonal increases in Chl-*a* concentration are usually related to large phytoplankton cells growing within a background of smaller phytoplankton (e.g., McAndrew et al., 2007; Mouw et al., 2012). In our study, the highest satellite Chl-*a* underestimations were found when phytoplankton larger than 10 µm represented more than 50% of the phytoplankton community (match-up points 8 and 10; Fig. 4.3). Furthermore, for half of the match-up points, the satellite Chl-*a* mismatch is greater than 35%, suggesting the ocean colour product in the selected area for this study, may not be as accurate as expected. The satellite Chl-*a* underestimation for lower *in situ* Chl-*a* (match-up points 2, 4 and 5; Fig. 4.3) can be attributed to the standard deviation of the averaged satellite Chl-*a* observations (Table 4.1) or to the presence of optical components as CDOM or NAP that are usually not significant in open ocean waters characterised by a low Chl-*a* (Mobley et al., 2004).

For the ten match-up points considered in this study, phytoplankton smaller than 10 µm were accurately detected by the satellite sensors and properly processed by the algorithms to derive a reliable Chl-*a* product (Table 4.1). Indeed, weighted values associated with the small and medium phytoplankton show that the Chl-*a* associated with these two phytoplankton classes do not need significant corrections (Table 4.3). This is also confirmed by the analysis performed when the large phytoplankton

class was excluded (Fig. 4.4b; Table 4.3), which produced similar linear regression slopes before (regression model B) and after (regression model C) weights were given to the medium and small phytoplankton. In this case, it is important to notice that the Chl-*a* satellite product is consistent with the sum of *in situ* Chl-*a* for small and medium phytoplankton, without including the large phytoplankton Chl-*a* contribution.

Phytoplankton larger than 10 μm seem to be the only size class to be strongly underestimated by the satellite Chl-*a*. Indeed, when considering all three phytoplankton size classes (regression model C; Fig. 4.4a), the weighting associated with the large phytoplankton class shows that satellite Chl-*a* estimates less than half of the *in situ* Chl-*a* associated with the large phytoplankton class (Table 4.3). These results suggest that the Chl-*a* associated with the large phytoplankton class was poorly detected by the remote sensing radiometers. Inconsistencies between *in situ* and estimated Chl-*a* concentration from observed remote-sensing reflectance can be related to a stronger package effect, that reduces absorption coefficients, causing an increased error in the final ocean colour product (Marra et al., 2007; Mouw et al., 2012).

Consistent with this concept, the first key point to emerge from our optical model simulations is that larger phytoplankton cell dimensions cause a decrease in the absorption coefficient for all Chl-*a* concentrations considered (Fig. 4.5a – c). In this case, the absorption decrease is related to the packaging of Chl-*a* relative to the energy impinging on the geometric cross-section of the cell (Fig. 4.1c; Astoreca et al., 2012; Bricaud, 2004; Ciotti et al., 2002; Ciotti and Bricaud, 2006). Indeed, it is known that an increased intracellular Chl-*a* concentration flattens the specific absorption spectra and decrease its magnitude (Duysens, 1956; Kirk, 1976; Morel and Bricaud, 1981). This is particularly evident in Figure 4.5c, where the same amount of Chl-*a* is distributed in a smaller number of bigger cells, causing an increased intracellular Chl-*a* concentration and thus an increased package effect. Similarly, the same Chl-*a* concentration distributed between a smaller number of similar size cells cells causes a decrease in the absorption signal. This is again related to the intracellular

Chl-*a* concentration that, while increasing, is causing a stronger package effect and thus a weaker absorption signal. Conversely, a higher number of cells allow the intracellular Chl-*a* concentration to be lower (i.e., less Chl-*a* per cell), causing a decreased package effect and a stronger absorption signal. Therefore, our simulations suggest the packaging effect is involved in the satellite Chl-*a* underestimation.

Changes in backscattering are only related to the particulate material in the water, thus, in our simulations, they arise from phytoplankton cells. Indeed, if we compare the scenarios in Figure 4.5e and 4.5f, the same number and dimension of phytoplankton cells produces equal backscattering coefficients regardless of the amount of intracellular Chl-*a* (C:Chl-*a* 150:1 Fig. 4.5e and C:Chl-*a* 50:1 Fig. 4.5f). Compared to the absorption process, the backscattering of oceanic particles and its relationship with phytoplankton size is not well characterised (Morel and Maritorena, 2001). Vaillancourt et al., (2004) showed that cell shape and internal structure rather than cell size have a bigger impact on backscattering efficiency than size alone. On the other hand, the second key point to emerge from our optical model simulations is that backscattering changes are almost not detectable for phytoplankton bigger than 10 µm (Fig. 4.5d – f). This is consistent with Stramski and Kiefer (1991) who showed backscattering of Case I waters is dominated by small particles (< 1 µm), with a non-significant backscattering contribution from particles larger than 8 µm. The low contribution of larger cells to backscattering could represent the second factor, combined with the packing effect, which causes the large phytoplankton to be barely detected by remote sensors. Moreover, our simulated scenarios show the greater impact on the backscattering signal caused by the abundance of phytoplankton cells rather than the phytoplankton cell dimension (Fig. 4.5d – f).

To highlight the phytoplankton size impact on the simulated satellite-like Chl-*a*, the results from Figure 4.5q were normalised by the smaller phytoplankton class Chl-*a* values. Thus, considering 3 mg m^{-3} of Chl-*a*, a C:Chl-*a* included between 20:1 and 150:1 and a range of

phytoplankton cells abundance between $9x10^5$ and $68x10^5$ L^{-1}, a ~10 µm phytoplankton cell is producing about half (45 to 59%) the simulated satellite-like Chl-*a* produced by the 1 µm cell (Fig. 4.6), consistently with regression model A that suggested satellite Chl-*a* only detects 0.55 of total *in situ* Chl-*a* value (Table 4.3).

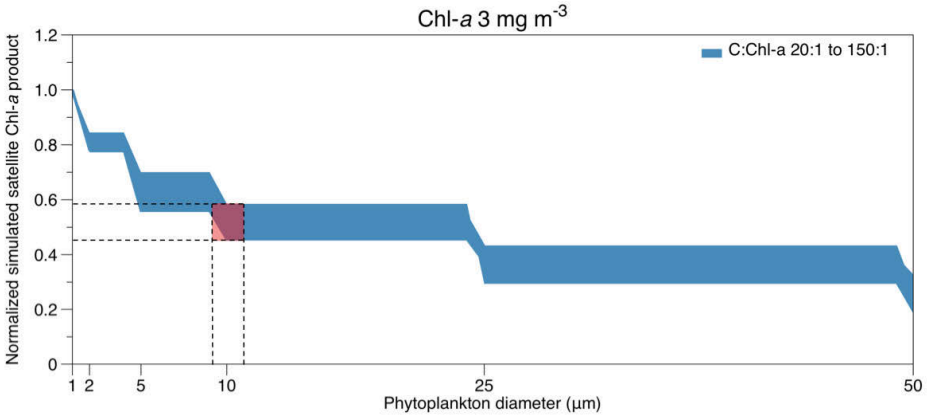

Figure 4.6 Simulated satellite Chl-*a* normalised by the 1 µm phytoplankton cells (3 mg m^{-3} Chl-*a* scenario from Fig. 4.5q). The figure shows C:Chl-*a* included between 20:1 and 150:1 in function of increasing phytoplankton sizes. The red area is comparing the simulated satellite-like Chl-*a* produced by 1 µm phytoplankton cells with the simulated satellite-like Chl-*a* produced by 10 ± 1 µm phytoplankton cells.

Therefore, simulations presented in this study are consistent with the *in situ* – satellite match-up analyses, showing an increased underestimation of the satellite-like Chl-*a* product for scenarios characterised by higher Chl-*a* (Fig. 4.5). On one hand, part of the satellite-like Chl-*a* underestimation could be related to components such as NAP or CDOM that were not considered in the simulations. On the other hand, these optical components are not major for Case I waters, but they can become more important with higher phytoplankton concentrations (Mobley et al., 2004).

Our match-up points between satellite and *in situ* data and our simulation results showed the satellite-like Chl-*a* underestimation to be related to phytoplankton cell size and cell abundance. Specifically, in our simulations, these two factors affect the intracellular Chl-*a* concentration causing an increased packaging effect and a weaker absorption signal. Moreover, backscattering coefficients are highly sensitive to cell

abundance and changes in the backscattering coefficient are almost not detectable for phytoplankton bigger than 10 μm. To improve the remotely sensed Chl-*a* product, *in situ* measurements that investigate links between phytoplankton communities size structure, bio-optical properties and the correspondent R_{rs}, from which the remotely sensed Chl-*a* product is estimated, would represent an extremely valuable source of data. Specifically, measurements that combine CTD profiles with IOPs, AOPs, CDOM, TSS and size fractionated Chl-*a* would allow to better explore the relation between the phytoplankton size structure and the remotely sensed Chl-*a* product underestimation. Furthermore, additional *in situ* size fractionated Chl-*a* measurements could provide enough information to determine when large phytoplankton cells contribute significantly to the total Chl-*a* concentration in a selected region. Then, based on these data, a Chl-*a* concentration threshold could be imposed to adjust the satellite Chl-*a* underestimation as well as have additional information on the phytoplankton size structure dynamics in the region.

5. Conclusion

In oligotrophic regions, such as the waters off eastern Australia, physical events regulate the nutrient supply to the euphotic zone. These nutrient injections cause an increase in Chl-*a*, associated with enhanced growth of large phytoplankton (e.g., diatoms; Doblin et al. 2016, Laiolo et al., 2016). Large photosynthetic cells are associated with lower absorption coefficients, related to an increased packaging effect that can cause higher uncertainty in the ocean colour product (e.g., Marra et al., 2007; Mouw et al., 2012). The matched-up points presented in this study revealed a regular underestimation for the higher values of *in situ* Chl-*a* analysed. Furthermore, the relation between the Chl-*a* associated with large phytoplankton cells and remotely sensed Chl-*a*, was confirmed.

The biogeochemical modelling community is now moving from assimilating remotely sensed Chl-*a* to assimilating remotely sensed reflectance, which has lower error (± 5%) compared to the remotely sensed Chl-*a* (± 35%) (e.g., Jones et al., 2016). *In situ* bio-optical

observations, including IOPs and AOPs will be useful to correct the remotely sensed Chl-*a* product. The number of automated platforms able to collect these measurements are increasing (i.e., Bio-Argo, gliders) and will soon provide extended spatial and temporal resolution of *in situ* bio-optical properties. These data could inform marine biogeochemical models able to solve for optical components, filling the gap between biogeochemical modelling and optics. Therefore, a combined assimilation of remotely sensed reflectance and *in situ* bio-optical observations will provide an improved representation of the real environment.

CHAPTER 5

General Discussion

5.1 Summary

In this PhD project, biogeochemical and optical modelling, ocean color data assimilation, *in situ* measurements and ship-board experiments were used to investigate phytoplankton dynamics and size structure in offshore eastern Australian waters (30°S to 40°S and 150°E to 160°E). Results presented in this thesis, summarised in Figure 5.1, have advanced the knowledge of phytoplankton dynamics in the study region, revealing insights about the assimilation of the remotely sensed Chl-*a* product.

Consistent with eddies occurring in other oligotrophic systems (e.g., Olaizola et al. 1993; Vaillancourt et al. 2003; Rodriguez et al. 2003; Brown et al. 2008), this thesis has shown that CE off East Australia are characterised by higher Chl-*a* and large phytoplankton cell (i.e., diatoms) concentrations, compared to ACE in the same region (Chapter 2). Furthermore, theoretical experiments presented in Chapter 3 suggested the remotely sensed Chl-*a* significantly underestimates Chl-*a* in CE and ACE because of a weak relationship between large-sized phytoplankton and remote-sensing reflectance. These observations are consistent with previous studies that suggest a direct relation between large-sized phytoplankton and increased underestimation of remotely sensed Chl-*a* (e.g., Marra et al., 2007; Szeto et al., 2011; Mouw et al., 2012). Subsequent comparisons between *in situ* Chl-*a* observations and corresponding ocean colour data have confirmed the remotely sensed Chl-*a* underestimation in eastern Australian waters and its relationship with the amount of Chl-*a* associated with large-sized phytoplankton (Chapter 4).

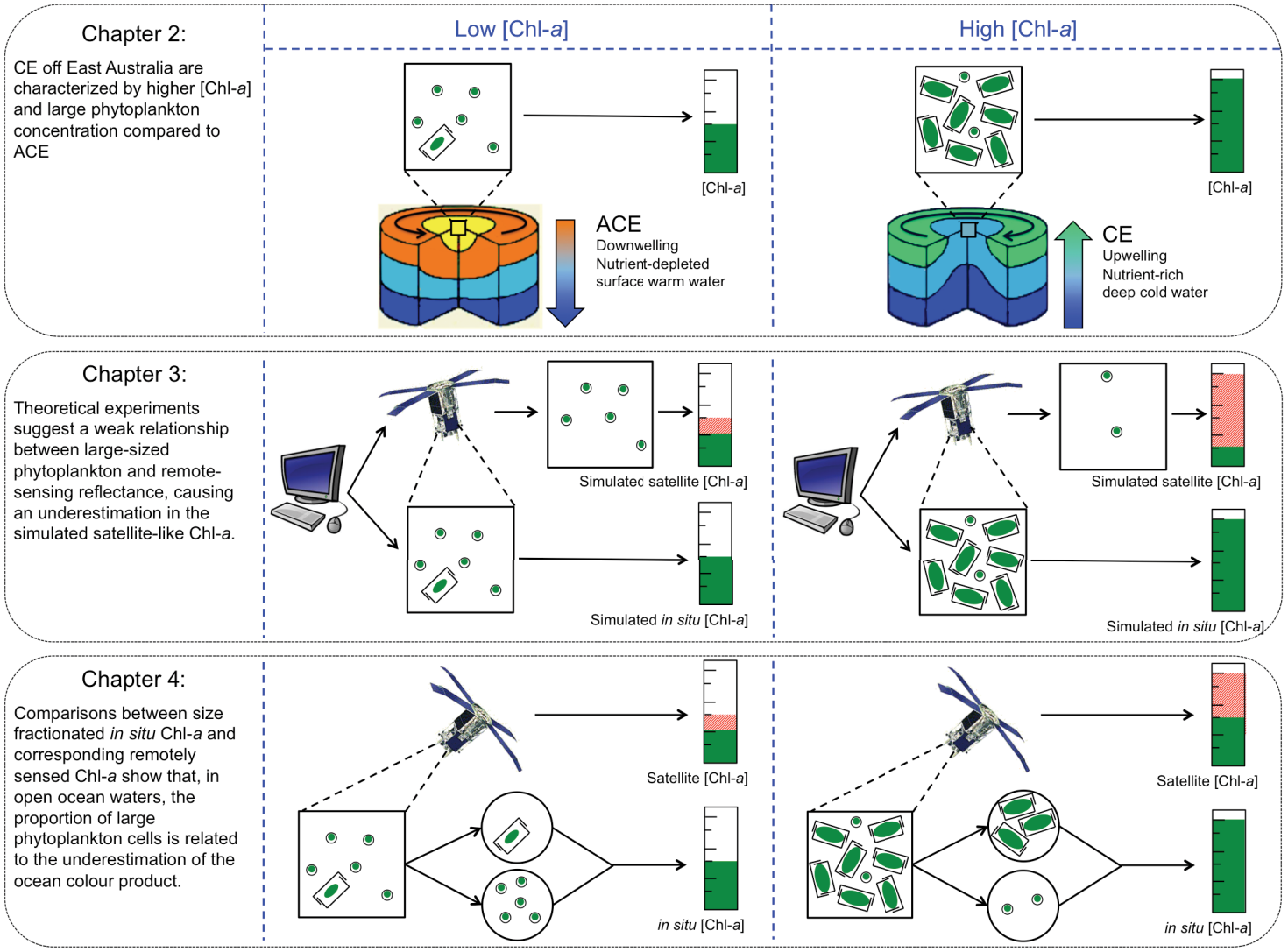

Figure 5.1: Conceptual diagram showing the key results of the thesis.

5.2 Implications for primary productivity

Remotely sensed measurements provide products characterized by high spatial and temporal resolution, particularly suitable for DA in marine biogeochemical models. Remotely sensed Chl-*a* represents the most commonly derived product used by the marine sciences community for DA and the key factor for interpreting ocean primary production (e.g., Behrenfeld, 2001; Campbell et al., 2002; Carr et al., 2006; Longhurst et al., 1995). Therefore, uncertainties and errors in the remotely sensed Chl-*a* product could lead to biased phytoplankton simulations and primary productivity estimates.

In this thesis, a single (WOMBAT) and a size dependent multi-phytoplankton class biogeochemical model (EMS) were used to investigate phytoplankton dynamics in CE and ACE off East Australia (Chapter 2). The parameters of the two biogeochemical models were optimised by assimilating the CE and ACE surface Chl-*a* seasonality, computed from remotely sensed Chl-*a*. Simulations obtained through WOMBAT and EMS showed similar primary productivity estimates for CE and ACE environments (Fig. 2.5 and 2.6). This result is not consistent with previously published empirical studies that suggest CEs are significantly more productive than ACEs (Jenkins, 1988; Falkowski et al., 1991; McGillicuddy and Robinson, 1998; McGillicuddy, 2015). This inconsistency could be related to the assimilated surface Chl-*a*, generated from the ocean colour product. Results presented in Chapter 3 and 4 revealed a regular satellite Chl-*a* product underestimation of *in situ* Chl-*a* concentrations. Specifically, in both simulations (Chapter 3) and observations (Chapter 4), the remotely sensed Chl-*a* underestimation appeared to be related to the amount of Chl-*a* associated with phytoplankton cells > 10 μm. Although all optical simulations performed in this thesis were processed through the OC3M algorithm, it has been shown that, in open ocean waters, different algorithms for different sensors (i.e., SeaWiFS, MODIS and MERIS) yield similar results (Morel et al., 2007). Therefore, the underestimation of the remotely sensed Chl-*a*

product should not be related to the specific algorithm used in this study to estimate the Chl-*a* (i.e., OC3M). Furthermore, results presented in Chapter 3 and 4 are consistent with previous studies that suggested the Chl-*a* product underestimation to be related to a greater packaging effect characteristic of large-sized phytoplankton, which reduces the absorption signal and hence increases the error of estimated Chl-*a* concentration (Marra et al., 2007; Szeto et al., 2011; Mouw et al., 2012).

The empirical results from this study add to a growing evidence base and suggest that there could be an underestimation by the Chl-*a* satellite product related to the amount of Chl-*a* associated with large-sized phytoplankton. In Chapter 2 of this thesis, the remotely sensed Chl-*a* was considered to be a good estimator of the total *in situ* Chl-*a*. Conversely, Chapter 3 and 4 revealed an underestimation by the Chl-*a* satellite associated with large-sized phytoplankton. Hence, based on results presented in Chapter 4, the Chl-*a* climatology of CE and ACE off East Australia (Fig. 2.4a) were assimilated again into EMS by weighting the Chl-*a* associated with the large phytoplankton size class by 0.35 (Table 4.3). This value was chosen on the basis of the results of the weighted linear regression which showed that there was a 35% underestimate of total Chl-a (Chapter 4).

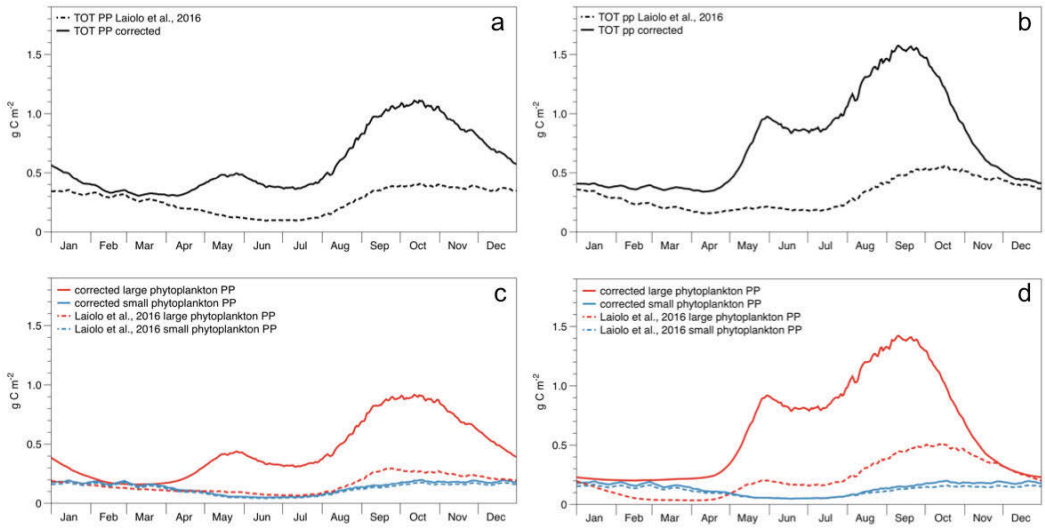

Figure 5.2: Primary proucctivity in ACE (left column) and CE (right column) before and after considering the remotely sensed Chl-*a* underestimation associated with large-sized

phytoplankton. Dashed lines in all panels show the primary productivity from Laiolo et al., 2016 (Chapter 2), while solid lines show the corrected primary productivity based on Chapter 4 (Table 4.3). Panels a and b represent the total primary productivity, panels c and d separate the total primary productivity into large (40 μm) and small (2 μm) phytoplankton contributions.

For this additional simulation, the Chl-*a* associated with the large phytoplankton class in EMS was multiplied by 0.35. Hence, EMS during the DA was forced to increase the large phytoplankton concentration to match the Chl-*a* climatology of CE and ACE, correcting for the estimated error associated with the large phytoplankton class (Fig. 2.4b; Chapter 2). The new DA produced a ~100% and ~85% increase in the CE and ACE total Chl-*a* respectively. This correction affected in turn, the primary productivity in both eddy environments. Indeed, compared to the case where the remotely sensed Chl-*a* was assumed to represent the *in situ* Chl-*a* (i.e., Chapter 2; Fig. 5.2a and b, dotted lines), the new simulations yielded a significant increase in the total primary productivity across the whole seasonal climatology, in both CE and ACE (~60% and ~50% respectively, Fig. 5.2a and b, solid lines). These differences appear to be uniquely related to the large-sized phytoplankton dynamics (Fig. 5.2c and d, solid red lines).

In eastern Australian waters, projections for climate change show a 20% increased transport of the EAC with an associated increase in eddy activity (Cai et al. 2005, Matear et al., 2013). These changes will impact phytoplankton concentration, composition and size structure, affecting primary productivity, export production, CO_2 uptake and sequestration (Doney et al. 2012; Dutkiewicz et al., 2015). Marine biogeochemical models are commonly used to estimate these ecosystem services. Errors associated with the ocean colour product are therefore propagated into the output of models calibrated through remotely sensed Chl-*a*. The simulations above show that the primary productivity in one CE could be 60% greater than is currently being estimated, so when scaled up to the number of eddies annually and how this may be projected into the future,

regional primary productivity could be significantly biased. Therefore, to have a consistent representation of the simulated environment, it is crucial to consider the role of phytoplankton size and its impact on bio-optical properties from which the Chl-*a* product is derived (Babin et al., 2003; Oubelkheir et al., 2006).

5.3 Implications for upper trophic levels

Phytoplankton represent the base of the marine food web and are responsible for almost half of the global primary production (Field et al., 1998). Usually, there is a tight relationship between nutrient availability, primary productivity, Chl-*a* and the size structure of the phytoplankton community (Falkowski and Knoll, 2007). As a consequence, increases in primary production and Chl-*a* propagate to higher trophic levels – i.e., primary and secondary consumers.

Zooplankton represent the intermediate trophic level between phytoplankton and fish. Small phytoplankton (i.e., ~2 μm) are grazed by ciliates and flagellates (i.e., 5 to 20 μm) (Sherr and Sherr, 1994). These microzooplankton can be consumed by larger zooplankton and thus contribute to food webs with five or more trophic levels (Sherr and Sherr, 1994; Link 2002). However, each trophic transfer is associated with ~70% loss of matter and energy (Cohen et al., 2003; Jennings and Mackinson, 2003). Conversely, larger phytoplankton (> 10 μm) are too big for most of the small grazers, hence they are grazed by larger zooplankton such as copepods (0.2 − 30 mm), which represent a direct food source for fishes (Ryther, 1969; Huys and Boxshall, 1991). Therefore, modelling phytoplankton size structure is essential to understand zooplankton dynamics and the consequent energy flow up the foodweb, with potential impacts even for fisheries (Mitra et al., 2014; Friedland et al., 2012). Indeed, Chapter 2 showed that, in CEs, higher concentrations of large phytoplankton increase significantly the growth rate of primary consumer (i.e., large sized zooplankton). The increased large sized zooplankton biomass can attract forage fish, resulting in the higher large sized

zooplankton mortality rate parameter value obtained through the data assimilation in CE. Conversely, this was not shown in the ACE environment simulations, where the large phytoplankton concentration was lower.

Marine biogeochemical models are extremely sensitive to zooplankton parameterization (e.g., Edwards and Yool, 2000; Mitra, 2009; Laiolo et al., 2016). Interestingly, less than ~20% of marine biogeochemical models assess their simulations with zooplankton observations (Arhonditsis and Brett, 2004). This is not only due to lack of data but is also because of the lack of awareness of available data and types of sampling systems (Everett et al., 2017). Chapter 2 of this thesis has shown that, in CE and ACE off East Australia, zooplankton parameters are a key factor in explaining the phytoplankton concentration and composition (Laiolo et al., 2016). A recommendation from this study is to make additional measurements of zooplankton biomass, size distribution to assess the results obtained through biogeochemical model simulations.

5.4 *In situ* and remotely-sensed measurements

Validation of biogeochemical models is critical in terms of their application to answering questions about changes in marine ecosystems. *In situ* observations (e.g., Laiolo et al., 2014) or remotely sensed data (e.g., Laiolo et al., 2016; Jones et al., 2016) are required to assess the simulation produced by marine biogeochemical models. Unfortunately, both *in situ* observations and remotely-sensed measurements are often not directly comparable with variables simulated by marine biogeochemical models.

Indeed, biogeochemical models usually represent phytoplankton biomass by the concentration of elements as nitrogen or carbon. On the other hand, one of the most common and convenient phytoplankton *in situ* observations is based on the active Chl-a fluorescence of cells (i.e., not a direct biomass measurement; Earp et al., 2011). Remotely sensed ocean

colour observations provide higher spatial and temporal resolution but are often not directly comparable with marine biogeochemical model outputs either. Indeed, ocean colour Chl-*a* does not represent a direct measurement of Chl-*a* as it is derived through algorithms from the remote-sensing reflectance (R_{rs}), which depends on the bio-optical properties of the water column. Conversely, bio-optical properties can be calculated from biogeochemical model simulations and these products could be directly compared with *in situ* (e.g., IOPs) or remotely sensed bio-optical observations (e.g., R_{rs}). Nevertheless, it is important to notice that there is no fully analytic bio-optical model yet. On the other hand, the optical model used in this thesis (Baird et al., 2016) is a great example where absorption is derived by physical principles, from particle sizes and pigment-specific absorption, without considering any empirical relationship.

Szeto et al., 2011 have shown that world's oceans are characterised by distinct optical properties, dependent on CDOM, NAP, phytoplankton cell sizes, their characteristic pigments and corresponding packaging within phytoplankton cells. Thus, models able to simulate optical properties of the water column represent a useful development for improving the simulation of variables in marine biogeochemical models (e.g., Fujii et al., 2007). Indeed, several studies have shown the advantages of adding optics into biogeochemical models (e.g., Sathyendranath and Platt, 2007; Kettle and Merchant, 2008) and recent studies have successfully coupled biogeochemical models to bio-optical models to simulate R_{rs} dynamics that can be directly compared with remotely-sensed observations (e.g., Dutkiewicz et al., 2015; Baird et al., 2016). The data presented in Chapter 3 of this thesis represents another example of the power of these coupled models. Indeed, a direct comparison between *in situ* and remotely sensed ocean colour was possible in an idealised experiment because IOPs, R_{rs} and a simulated satellite-like Chl-*a* product were calculated directly through EMS simulations by a bio-optical model.

In coastal water, CDOM and NAP concentrations do not covary with

phytoplankton concentrations, therefore they significantly influence the bio-optical properties of the water column (Mobley et al., 2004). Conversely, in open ocean waters, where phytoplankton is the main component responsible for variations in optical properties (Gordon and Morel, 1983; Morel and Prieur, 1977; Mobley et al., 2004), *in situ* and remotely sensed bio-optical observations represent a valuable and direct source of information to compare and calibrate marine biogeochemical models coupled with bio-optical models.

5.5 Future research

Nowadays, to better understand biogeochemical cycles and their links with phytoplankton dynamics, more complex models that add phytoplankton compartments and functional groups to the basic NPZD structure are required (Finkel et al., 2009; Follows and Dutkiewicz, 2011). While flow cytometry, molecular techniques and microscopy can provide much detail about the composition of phytoplankton communities (Doblin et al. 2016), for modellers these observations will always be sparse. Therefore, identifying phytoplankton functional types has typically involved remote sensing measurements (Mouw et al. 2017). These methods are based on algorithms that retrieve phytoplankton size classes (Fujiwara et al. 2011, Roy et al. 2011, Bricaud et al. 2012, Li et al. 2013), phytoplankton taxonomic composition (Alvain et al. 2005, Alvain et al. 2008, Bracher et al. 2009, Hirata et al. 2011, Sadeghi et al. 1012), or particle size distribution that comprises all particles including phytoplankton (Kostadinov et al. 2009, Kostadinov et al. 2010). The marine biogeochemical DA community is now moving from the assimilation of Chl-*a* derived from remotely sensed ocean colour to the assimilation of R_{rs}. Indeed, assimilating a combination of R_{rs} wavebands leads to a significant improvement over assimilating ocean colour derived Chl-*a* (e.g., Jones et al., 2016). Furthermore, results presented in this thesis suggest that remotely sensed Chl-*a* yields little information of large phytoplankton classes (e.g., filamentous, colonial N-fixers, large chain

forming diatoms) that can have important impacts on ecosystem services and cycles of different elements. Therefore, *in situ* measurements of bio-optical properties are required to assess optical models able to use the output of biogeochemical models to generate optical data that can be directly compared with observations (e.g., IOPs, R_{rs}).

This thesis highlighted the importance of considering the role of phytoplankton size structure in biogeochemical model simulations (Chapter 1), theoretical experiments (Chapter 2) and comparison between *in situ* and satellite observations (Chapter 3). Thus, *in situ* measurements able to link the phytoplankton size structure with the bio-optical properties and the correspondent R_{rs}, from which the remotely sensed Chl-*a* product is estimated, are extremely valuable to reduce the uncertainty of ocean colour products. Specifically, measurements that combine CTD profiles with IOPs (absorption, backscattering, particle size distribution), AOPs (R_{rs}), CDOM, total suspended particles (TSS), size fractionated Chl-*a* and primary production would be extremely useful for the DA scientific community. The information obtained from these measurements can then be used to extract phytoplankton size information from the R_{rs} and, in turn, inform size-dependent biogeochemical models.

Results presented in Chapter 3 of this thesis show that, *in situ* Chl-*a* observations and satellite remote sensing together can provide additional information about the phytoplankton size structure. The mismatch between *in situ* Chl-*a* concentration measurements and the corresponding remotely sensed Chl-*a* could be largely represented by phytoplankton larger than 10 μm. This information represents a crucial factor to progress our understanding of processes influencing regional primary productivity and elemental cycling (e.g., Fig. 5.2). While ocean colour already provides high spatial and temporal resolution data, the number of *in situ* observations is sparse in time and space, although the use of *in situ* automated platforms is increasing (e.g., Gliders, Bio-Argo). In particular, the new Bio-Argo platforms are equipped with low-power sensors that measure bio-optical and biogeochemical properties of the water column, including

backscattering and fluorescence (from which is possible to retrieve Chl-*a* concentration). Bio-Argo *in situ* measurements and remotely sensed data could be assimilated in a biogeochemical model able to solve for optically significant seawater constituents. Therefore, *in situ* information, coupled to remotely-sensed bio-optical measurements could lead the development of next-generation biogeochemical models.

Appendix 1

Bio-optical model

First the IOPs (i.e., absorption, scattering and backscattering) of the water column are calculated from the model state variables and parameters. Then, the optical model solves for the AOPs including the remote-sensing reflectance (R_{rs}). R_{rs} at two wavelengths can then be processed through the OC3M algorithm to obtain an estimation of the Chl-*a*.

Inherent optical properties (IOPs)

Absorption coefficient. The absorption-cross section (α) of a spherical cell without considering internal scattering is given by (Duysens, 1956; Kirk, 1975):

$$\alpha = \pi r^2 \left(1 - \frac{2\left(1-(1+2\gamma c_i r)e^{-2\gamma c_i r}\right)}{(2\gamma c_i r)^2}\right) \quad \text{(a.1)}$$

where (r) represents the radius of cell, (γ) the pigment-specific absorption coefficient, (c_i) the homogeneous intracellular pigment concentration. πr^2 is the projected area of a sphere and the bracketed term can range from 0 for no absorption ($\gamma c_i r = 0$) to 1 when the cell is fully opaque ($\gamma c_i r \to \infty$). The total absorption ($a_{T,\lambda}$), is given by:

$$a_{T,\lambda} = a_{w,\lambda} + \sum_{x=1}^{N} n_x \alpha_{x,\lambda} \quad \text{(a.2)}$$

where $a_{w,\lambda}$ represents clear water absorption, N the number of phytoplankton classes (in our case $N \leq 2$ large and small phytoplankton), n the concentration of cells (cell m^{-3}) and α_λ the absorption cross-section (m^2 $cell^{-1}$).

Scattering coefficient. The total scattering coefficient is given by:

$$b_{T,\lambda} = b_{w,\lambda} + b_{phy,\lambda} \sum_{x=1}^{N} n_x c_{i,x} V_x \quad \text{(a.3)}$$

$b_{w,\lambda}$ is the scattering coefficient due to sea water, the phytoplankton scattering is the product of the Chl-*a* specific phytoplankton scattering coefficient ($b_{phy,\lambda}$) and the water column concentration of all classes ($\sum_{x=1}^{N} n_x c_{i,x} V_x$), where N represents the number of phytoplankton classes, n the concentration of cells (cell m^{-3}), c_i is the Chl-*a* concentration in the cell

and V is the cell volume. The value for $b_{\mathrm{phy},\lambda}$ is set to 0.2 (mg Chl-*a* $m^{-2})^{-1}$ for all wavelengths, a typical value for marine phytoplankton (Kirk, 1994).

Backscattering coefficient. Backscattering coefficient (b_b) has a component due to pure seawater and a component due to particulates. The particulate component for phytoplankton is strongly related to cell carbon (and therefore cell size) and the number of cells (Vaillancourt et al., 2004):

$$b^*_{bphy,\lambda} = 5{\times}10^{-15} m_C^{1.002} \quad \text{(a.4)}$$

were m_C is the carbon content of the cells, here in pg cell^{-1}. The total backscatter then becomes:

$$b_{\mathrm{b},\lambda} = \tilde{b}_{\mathrm{w}} b_{\mathrm{w},\lambda} + b^*_{\mathrm{bphy},\lambda} n \quad \text{(a.5)}$$

where the backscatter ratio of pure seawater, ($\tilde{b}_{\mathrm{w}}$) is 0.5 and n is the concentration of cells.

Remote sensing reflectance (R_{rs})

To calculate the R_{rs} at the surface, we need to consider the light returning from multiple depths and the bottom. The ratio of the backscattering coefficient to the sum of backscattering and absorption coefficients for the whole water column, u_λ, is:

$$u_\lambda = \sum \frac{w_{\lambda,z'} b_{\mathrm{b},\lambda,z'}}{a_{\lambda,z'} + b_{\mathrm{b},\lambda,z'}} \quad \text{(a.6)}$$

where $w_{\lambda,z'}$ is a weighting representing the component of the R_{rs} due to the absorption and scattering at depth z'.

$$w_{\lambda,\mathrm{z}} = \frac{1}{z_1 - z_0}\left(\int_0^{z_1} \exp\left(-2K_{\lambda,z'}\right)\mathrm{d}z' - \int_0^{z_0} \exp\left(-2K_{\lambda,z'}\right)\mathrm{d}z'\right) \quad \text{(a.7)}$$

$$= \frac{1}{z_1 - z_0}\int_{z_0}^{z_1} \exp\left(-2K_{\lambda,z'}\right)\mathrm{d}z' \quad \text{(a.8)}$$

in this case, the integral of $w_{\lambda,z}$ to infinite depth is 1. In areas where light reaches the bottom, the integral of $w_{\lambda,z}$ to the bottom is less than one, and benthic reflectance is important. Note that the weighting of the surface expression of an IOP based on twice the vertical attenuation rate has been used in semi-analytical reflectance models (Lee et al., 2002), to consider

the surface expression of depth-varying Chl-*a* concentration (Moline and Prezelin, 2000). K_λ represents the vertical attenuation coefficient at wavelength λ, the factor of 2 accounts for the pathlength of both downwelling and upwelling light. When considering absorption and scattering, K_λ is given by:

$$K_\lambda = \frac{a_{\mathrm{T},\lambda}}{\cos\theta_{\mathrm{sw}}}\sqrt{1 + (g_{\mathrm{i}} + g_{\mathrm{ii}}\cos\theta_{\mathrm{sw}})\frac{b_{\mathrm{T},\lambda}}{a_{\mathrm{T},\lambda}}} \quad \text{(a.9)}$$

The term outside the square root approximates the effect of absorption, where $a_{\mathrm{T},\lambda}$ is the total absorption. The term within the square root represents scattering as an extended pathlength through the water column, where g_{i} and g_{ii} are empirical constants and take values of 0.402 and 0.180 respectively (Kirk, 1991; Mobley, 1994). For waters ranging from coastal to open ocean, the average cosine of scattering varies by only a small amount (0.86 – 0.95, Kirk, (1991)), and thus uncertainties in g_{i} and g_{ii} do not strongly affect K_λ.

The below-surface remote-sensing reflectance ($\mathrm{r_{rs}}$), is given by:

$$r_{\mathrm{rs},\lambda} = g_0 u_\lambda + g_1 u_\lambda^2 \quad \text{(a.10)}$$

where $g_0 = 0.895$ and $g_1 = 0.1247$ are empirical constants for the nadir-view in oceanic waters (Lee et al., 2002; Brando et al., 2012), and these constants result in a change of units from the unitless u to a per unit of solid angle, $\mathrm{sr^{-1}}$, quantity $r_{\mathrm{rs},\lambda}$.

The above-surface remote-sensing reflectance, through rearranging Lee et al. (2002), is given by:

$$R_{\mathrm{rs},\lambda} = \frac{0.52\mathrm{r_{rs},\lambda}}{1 - 1.7\mathrm{r_{rs},\lambda}} \quad \text{(a.11)}$$

References

Aas, E., 1996. “Refractive Index of Phytoplankton Derived from Its Metabolite Composition.” Journal of Plankton Research, 18 (12): 2223–2249. https://doi.org/10.1093/plankt/18.12.2223.

ACRI-ST GlobColour Team, Mangin, A., Fanton d’Andon, O., 2015. GlobColour Product User Guide, GC-UM-ACR-PUG-01, Version 3.2

Ajani, P., Lee, R., Pritchard, T., Krogh, M. (2001). Phytoplankton Dynamics at a Long-term Coastal Station off Sydney, Australia. Journal of Coastal Research, Special Issue 34. International Coastal Symposium (ICS 2000): Challenges for the 21st century in coastal sciences , Engineering and Environments, 60-73

Alvain, S., Moulin, C., Dandonneau, Y., Bréon, F. M., 2005. Remote sensing of phytoplankton groups in case 1 waters from global SeaWiFS imagery. Deep Sea Research Part I: Oceanographic Research Papers, 52(11): 1989–2004. doi:10.1016/j.dsr.2005.06.015

Alvain, S., Moulin, C., Dandonneau, Y., Loisel, H., 2008. Seasonal distribution and succession of dominant phytoplankton groups in the global ocean: A satellite view. Global Biogeochemical Cycles, 22(3): GB3001. doi:10.1029/2007GB003154

Anderson, D. M., Glibert, P. M., Burkholder, J. M., 2002. Harmful Algal Blooms and Eutrophication Nutrient Sources, Composition, and Consequences. Estuaries, 25: 704-726.

Anderson, T. R., 2005. Plankton functional type modelling: running before we can walk? Journal of Plankton Research, 27(11): 1073-1081.

Angel, M. V., Fasham, M. J. R., 1983. Eddies and biological processes A.R. Robinson (Ed.), Eddies in Marine Science, Springer, Berlin (1983) Chap. 22

Antoine, D., Babin, M., Berthon, J.-F., Bricaud, A., Gentili, B., Loisel, H., Maritorena, S., Stramski, D., 2014. Shedding Light on the Sea: André Morel's Legacy to Optical Oceanography. Annual Review of Marine Science, 6(1): 1–21. doi:10.1146/annurev-marine-010213-135135

Arhonditsis, G. B., Brett, M. T., 2004. Evaluation of the current state of mechanistic aquatic biogeochemical modeling. Mar. Ecol. Prog. Ser. 271,

13–26. doi: 10.3354/meps271013

Arístegui, J., Montero, M. F., 2005. Temporal and spatial changes in plankton respiration and biomass in the Canary Islands region: the effect of mesoscale variability. Journal of Marine Systems, 54(1-4): 65-82. doi:10.1016/j.jmarsys.2004.07.004

Arístegui, J., Tett, P., Hernandez-Guerra, A., Basterretxea, G., Montero, M. F., Wild, K., Sangra, P., Hernandez-Leon, S., Canton, M., Garcia-Braun, J. A., Pacheco, M., Barton, E. D., 1997. The influence of island-generated eddies on chlorophyll distribution: a study of mesoscale variation around Gran Canaria. Deep-Sea Research, 44(1): 71-96.

Astoreca, R., Doxaran, D., Ruddick, K., Rousseau, V., Lancelot, C., 2012. Influence of suspended particle concentration, composition and size on the variability of inherent optical properties of the Southern North Sea. Continental Shelf Research, 35: 117–128. doi:10.1016/j.csr.2012.01.007

Athias, V., Mazzega, P., Jeandel, C., 2000. Selecting a global optimization method to estimate the oceanic particle cycling rate constants. Journal of Marine Research, 58: 675–707.

Atkinson, L. P., Huthnance, J., Blanco, J. L., 2004. Circulation, mixing and the distribution of remineralized nutrients. The Sea, Volume 13, edited by Robinson A. R., McCarthy J., Rothschild B. J. Chapter 4 pp. 227–267.

Baas Becking, L. G. M., 1934. Geobiologie of Inleiding tot de Milieukunde. The Hague: Van Stockum & Zoon.

Babin, M., Stramski, D., Ferrari, G. M., Claustre, H., Bricaud, A., Obolensky, G., Hoepffner, N., 2003. Variations in the light absorption coefficients of phytoplankton, nonalgal particles, and dissolved organic matter in coastal waters around Europe. Journal of Geophysical Research, 108(C7), 3211. doi:10.1029/2001JC000882

Baird, M. E., Cherukuru, N., Jones, E., Margvelashvili, N., Mongin, M., Oubelkheir, K., Ralph, P.J., Rizwi, F., Robson, B.J., Schroeder, T., Skerratt, J., Steven, A.D.L., Wild-Allen, K.A., 2016. Remote-sensing reflectance and true colour produced by a coupled hydrodynamic, optical, sediment, biogeochemical model of the Great Barrier Reef, Australia:

Comparison with satellite data. Environmental Modelling & Software, 78(C): 79–96. doi:10.1016/j.envsoft.2015.11.025

Baird, M. E., Ralph, P. J., Rizwi, F., Wild-Allen, K. A., Steven, A. D. L., 2013. A dynamic model of the cellular carbon to chlorophyll ratio applied to a batch culture and a continental shelf ecosystem. Limnology and Oceanography, 58(4): 1215–1226. doi:10.4319/lo.2013.58.4.1215

Baird, M. E., Suthers, I. M., 2007. A size-resolved pelagic ecosystem model. Ecological Modelling, 203(3-4): 185-203.

Baird, M. E., Suthers, I. M., Griffin, D. A., Hollings, B., Pattiaratch, C., Everett, J. D., Roughan, M., Oubelkhei, K., Doblin, M. A., 2011. The effect of surface flooding on the physical-biogeochemical dynamics of a warm core eddy off southeast Australia. Deep-Sea Research II, 58 (5): 592-605.

Bakun, A. 2006. Fronts and eddies as key structures in the habitat of marine fish larvae: opportunity, adaptive response and competitive advantage. Scientia Marina, 70S2: 105-122.

Barlow, R., Aiken, J., Moore, G. F., Holligan, P. M., Lavender, S., 2004. Pigment adaptations in surface phytoplankton along the eastern boundary of the Atlantic Ocean. Marine Ecology Progress Series, 281: 13-26.

Barton, I. J. 2002. Ocean Currents from Successive Satellite Images: The Reciprocal Filtering Technique. Journal of Atmospheric and Oceanic Technology, 19: 1677–1689.

Becker, V., Huszar, V. L. M., Crossetti, L. O., 2009. Responses of phytoplankton functional groups to the mixing regime in a deep subtropical reservoir. Hydrobiologia, 628(1): 137-151.

Behrenfeld, M. J., 2001. Biospheric Primary Production During an ENSO Transition. Science, 291: 2594–2597. doi:10.1126/science.1055071

Behrenfeld, M. J., 2010. Abandoning Sverdrup's Critical Depth Hypothesis. Ecology, 91: 977-989.

Behrenfeld, M. J., Boss, E. S., 2014. Resurrecting the Ecological Underpinnings of Ocean Plankton Blooms. Annual Review of Marine Science, 6(1): 167-194. doi:10.1146/annurev-marine-052913-021325

Bergman, B., Sandh, G., Lin, S., Larsson, J., Carpenter, E. J., 2013.

Trichodesmium - a widespread marine cyanobacterium with unusual nitrogen fixation properties. FEMS Microbiology Reviews, 37: 286-302.

Bibby, T. S., Moore, C. M., 2011. Silicate:nitrate ratios of upwelled waters control the phytoplankton community sustained by mesoscale eddies in sub-tropical North Atlantic and Pacific. Biogeosciences, 8(3): 657-666. doi:10.5194/bg-8-657-2011

Bidigare, R. R., Ondursek, M. E., Morrow, J. H., Kiefer, D., 1990. In Vivo Absorption Properties of Algal Pigments. Proceedings for SPIE Ocean Optics X. http://dx.doi.org/10.1117/12.21451

Bindoff, N. L., Willebrand, J., Artale, V., Cazenave, A., Gregory, J.M., Gulev, S., Hanawa, K., Le Quéré, C., Levitus, S., Nojiri, Y., Shum, C. K., Talley, L. D., Unnikrishnan, A. S., 2007. Observations: oceanic climate change and sea level. In Climate Change 2007: The Physical Science Basis. Cambridge: Cambridge University Press, 385-432.

Bopp, L., Resplandy, L., Orr, J. C., Doney, S. C., Dunne, J. P., Gehlen, M., Halloran, P., Heinze, C., Ilyina, T., Séférian, R., Tjiputra, J., Vichi, M., 2013. Multiple stressors of ocean ecosystems in the 21st century: projections with CMIP5 models. Biogeosciences, 10(10): 6225-6245. doi:10.5194/bg-10-6225-2013

Boyd, P. W., Doney, S. C., 2002. Modelling regional responses by marine pelagic ecosystems to global climate change. Geophysical Research Letters, 29(16), 53-1–53-4. doi:10.1029/2001GL014130

Bracher, A., Vountas, M., Dinter, T., Burrows, J. P., Röttgers, R., Peeken, I., 2009. Quantitative observation of cyanobacteria and diatoms from space using PhytoDOAS on SCIAMACHY data. Biogeosciences, 6(5): 751–764. doi:10.5194/bg-6-751-2009

Brainerd, K. E., Gregg, M. C., 1995. Surface mixed and mixing layer depths. Deep Sea Research, 42: 1521-1543.

Brando, V. E., Dekker, A. G., Park, Y. J., Schroeder, T., 2012. Adaptive semianalytical inversion of ocean color radiometry in optically complex waters. Applied Optics, 51: 2808-2833.

Bricaud, A., 2004. Natural variability of phytoplanktonic absorption in oceanic

waters: Influence of the size structure of algal populations. Journal of Geophysical Research, 109: (C11):1526. doi:10.1029/2004JC002419

Bricaud, A., Babin, M., Morel, A., Claustre, H., 1995. Variability in the Chlorophyll-Specific Absorption Coefficients of Natural Phytoplankton: Analysis and Parameterization. Journal of Geophysical Research, 100: (C7):13321. https://doi.org/10.1029/95JC00463.

Bricaud, A., Ciotti, A. M., Gentili, B., 2012. Spatial-temporal variations in phytoplankton size and colored detrital matter absorption at global and regional scales, as derived from twelve years of SeaWiFS data (1998-2009). Global Biogeochemical Cycles, 26(1): GB1010. doi:10.1029/2010GB003952

Bricaud, A., Claustre, H., Ras, J., Oubelkheir, K., 2004. Natural Variability of Phytoplanktonic Absorption in Oceanic Waters: Influence of the Size Structure of Algal Populations. Journal of Geophysical Research, 109, C11010. doi:10.1029/2004JC002419

Bricaud, A., Stramski, D., 1990. Spectral Absorption Coefficients of Living Phytoplankton and Nonalgal Biogenous Matter: A Comparison between the Peru Upwelling Area and the Sargasso Sea. Limnology and Oceanography, 35(3): 562–582.

Brieva, D., Ribbe, J., Lemckert, C., 2015. Is the East Australian Current causing a marine ecological hot-spot and an important fisheries near Fraser Island, Australia? Estuarine and Coastal Marine Science, 153: 121–134. doi:10.1016/j.ecss.2014.12.012

Brown, S. L., Landry, M. R., Selph, K. E., Jin Yang, E., Rii, Y. M., Bidigare, R. R., 2008. Diatoms in the desert: Plankton community response to a mesoscale eddy in the subtropical North Pacific. Deep Sea Research Part II: Topical Studies in Oceanography 55: 1321–1333. doi:10.1016/j.dsr2.2008.02.012

Bruggeman, J., Kooijman, S. A. L. M., 2007. A biodiversity-inspired approach to aquatic ecosystem modeling. Limnology and Oceanography, 52(4): 1533-1544.

Cai, W., Shi, G., Cowan, T., Bi, D., Ribbe, J., 2005. The response of the

Southern Annular Mode, the East Australian Current, and the southern mid-latitude ocean circulation to global warming. Geophysical Research Letters, 32(23): L23706.

Campbell, J., Antoine, D., Armstrong, R., Arrigo, K., Balch, W., Barber, R., Behrenfeld, M., Bidigare, R., Bishop, J., Carr, M.-E., Esaias, W., Falkowski, P., Hoepffner, N., Iverson, R., Kiefer, D., Lohrenz, S., Marra, J., Morel, A., Ryan, J., Vedernikov, V., Waters, K., Yentsch, C., Yoder, J., 2002. Comparison of algorithms for estimating ocean primary production from surface chlorophyll, temperature, and irradiance. Global Biogeochemical Cycles, 16: 9–1–9–15. doi:10.1029/2001GB001444

Carder, K. L., Steward, R. G., Paul, J. H., Vargo, G. A., 1986. Relationships between chlorophyll and ocean color constituents as they affect remote-sensing reflectance models. Limnology and Oceanography, 31: 403-413.

Carr, M.-E., Friedrichs, M. A. M., Schmeltz, M., Noguchi, A. M., Antoine, D., Arrigo, K. R., Asanuma, I., Aumont, O., Barber, R., Behrenfeld, M., Bidigare, R., Buitenhuis, E.T., Campbell, J., Ciotti, A., Dierssen, H., Dowell, M., Dunne, J., Esaias, W., Gentili, B., Gregg, W., Groom, S., Hoepffner, N., Ishizaka, J., Kameda, T., Le Quéré, C., Lohrenz, S., Marra, J., Mélin, F., Moore, K., Morel, A., Reddy, T. E., Ryan, J., Scardi, M., Smyth, T., Turpie, K., Tilstone, G., Waters, K., Yamanaka, Y., 2006. A comparison of global estimates of marine primary production from ocean color. Deep-Sea Research Part II, 53(5-7): 741–770. doi:10.1016/j.dsr2.2006.01.028

Chelton, D. B., Schlax, M. G., Samelson, R. M., 2011. Global observations of nonlinear mesoscale eddies. Progress in Oceanography, 91: 167–216. doi:10.1016/j.pocean.2011.01.002

Cherukuru, N., Davies, P. L., Brando, V. E., Anstee, J. M., Baird, M. E., Clementson, L. A., Doblin, M. A., 2016. Physical oceanographic processes influence bio-optical properties in the Tasman Sea. Journal of Sea Research, 110: 1–7. doi:10.1016/j.seares.2016.01.008

Ciavatta, S., Kay, S., Saux-Picart, S., Butenschön, M., Allen, J. I., 2016. Decadal reanalysis of biogeochemical indicators and fluxes in the North West

European shelf-sea ecosystem. Journal of Geophysical Research, 121(3): 1824–1845. doi:10.1002/2015JC011496

Ciotti, Á.M., Bricaud, A., 2006. Retrievals of a size parameter for phytoplankton and spectral light absorption by colored detrital matter from water-leaving radiances at SeaWiFS channels in a continental shelf region off Brazil. Limnology and Oceanography, 4: 237–253. doi:10.4319/lom.2006.4.237

Ciotti, Á.M., Lewis, M.R., Cullen, J.J., 2002. Assessment of the relationships between dominant cell size in natural phytoplankton communities and the spectral shape of the absorption coefficient. Limnology and Oceanography, 47: 404–417. doi:10.4319/lo.2002.47.2.0404

Cohen, J.E., Pimm, S.L., Yodzis, P., Saldana, J., 1993. Body sizes of animal predators and animal prey in food webs. Journal of Animal Ecology. 62, 67-78

Crawford, W. R., Brickley, P. J., Thomas, A. C., 2007. Mesoscale eddies dominate surface phytoplankton in northern Gulf of Alaska. Progress in Oceanography, 75(2): 287-303.

Cresswell, G. R., 1982. The Coalescence of Two East Australian Current Warm-Core Eddies. Science, 215: 161-164.

Cresswell, G. R., 1983. Physical evolution of Tasman Sea Eddy J. Australian Journal of Marine and Freshwater Research, 34: 495-513.

Cresswell, G. R., 1994. Nutrient enrichment of the Sydney continental shelf. Australian Journal of Marine and Freshwater Research, 45: 677-691

CSIRO Coastal Environmental Modelling Team, 2014. CSIRO Environmental Modelling Suite: Scientific description of the optical, carbon chemistry and biogeochemical models parameterised for the Great Barrier Reef. Commonwealth Scientific and Industrial Research Organisation Marine and Atmospheric Research, GPO Box 1598, Hobart 7001, Australia.

de Boyer Montegut, C., Madec, G., Fischer, A. S., Lazar, A., Iudicone, D., 2004. Mixed layer depth over the global ocean: An examination of profile data and a profile-based climatology. Journal of Geophysical Research, 109: C12003.

Dickey, T., Lewis, M., Chang, G., 2006. Optical oceanography: Recent advances

and future directions using global remote sensing and in situ observations. Reviews of Geophysics, 44: RG1001. doi:10.1029/2003RG000148

Dickey, T., Lewis, M., Chang, G., 2006. Optical oceanography: Recent advances and future directions using global remote sensing and in situ observations. Reviews of Geophysics. 44: 1639. doi:10.1029/2003RG000148

Dietze, H., Matear, R. J., Moore, T., 2009. Nutrient supply to anticyclonic meso-scale eddies off western Australia estimated with artificial tracers released in a circulation model. Deep-Sea Research Part I, 56: 1440-1448.

Doblin, M. A., Petrou, K., Sinutok, S., Seymour, J.R., Messer, L.F., Brown, M.V., Norman, L., Everett, J.D., McInnes, A.S., Ralph, P.J., Thompson, P.A., Hassler, C.S., 2016. Nutrient uplift in a cyclonic eddy increases diversity, primary productivity and iron demand of microbial communities relative to a western boundary current. PeerJ, 4: e1973. doi:10.7717/peerj.1973

Doney, S. C., Fabry, V. J., Feely, R. A., Kleypas, J. A., 2009. Ocean acidification: the other CO2 problem. Annual Review of Marine Science, 1: 169-92.

Doney, S. C., Ruckelshaus, M., Duffy, E. J., Barry, J. P., Chan, F., English, C. A., Galindo, H. M., Grebmeier, J. M., Hollowed, A. B., Knowlton, N., Polovina, J., Rabalais, N. N., Sydeman, W. J., Talley, L. D., 2012. Climate Change Impacts on Marine Ecosystems. Annual Review of Marine Science, 4(1): 11-37.

Dong, S., Sprintall, J., Gille, S. T., Talley, L., 2008. Southern Ocean mixed-layer depth from Argo float profiles. Journal of Geophysical Research, 113(C6): C06013.

Doron, M., Brasseur, P., Brankart, J.-M., Losa, S. N., Melet, A., 2013. Stochastic estimation of biogeochemical parameters from Globcolour ocean colour satellite data in a North Atlantic 3D ocean coupled physical–biogeochemical model. Journal of Marine Systems, 117-118: 81–95. doi:10.1016/j.jmarsys.2013.02.007

Doty, M. S., Oguri, M., 1957. Evidencefor a photosynthetic daily periodicity. Limnology and Oceanography, 2: 37-40.

Dowd, M., 2011. Estimating parameters for a stochastic dynamic marine ecological system. Environmetrics, 72(3): 501–515. doi:10.1002/env.1083

Dubinsky, Z., Stambler, N., 2009. Photoacclimation processes in phytoplankton: mechanisms, consequences, and applications. Aquatic Microbial Ecology, 56: 163-176.

Dufois, F., Hardman-Mountford, N. J., Greenwood, J., Richardson, A. J., Feng, M., Matear, R. J., 2016. Anticyclonic eddies are more productive than cyclonic eddies in subtropical gyres because of winter mixing. Science Advances, 2(5): e1600282–e1600282. doi:10.1126/sciadv.1600282

Dufois, F., Hardman-Mountford, N. J., Greenwood, J., Richardson, A. J., Feng, M., Herbette, S., Matear R., 2014. Impact of eddies on surface chlorophyll in the South Indian Ocean. Journal of Geophysical Research: Oceans, 119(11): 8061-8077. doi:10.1002/2014JC010164

Dugdale, R. C., Wilkerson, F. P., 1998. Silicate regulation of new production in the equatorial Pacific upwelling. Nature, 391: 270–273. doi:10.1038/34630

Dutkiewicz, S., Follows, M. J., Bragg, J. G., 2009. Modeling the coupling of ocean ecology and biogeochemistry. Global Biogeochemical Cycles, 23, GB4017. doi:10.1029/2008GB003405

Dutkiewicz, S., Hickman, A. E., Jahn, O., Gregg, W. W., Mouw, C. B., Follows, M. J., 2015. Capturing optically important constituents and properties in a marine biogeochemical and ecosystem model. Biogeosciences, 12(14), 4447-4481. doi:10.5194/bg-12-4447-2015

Duysens, L. N. M., 1956. The Flattening of the Absorption Spectra of Suspensions as Compared to that of Solutions. Biochimica et Biophysica Acta, 19: 1–12. https://doi.org/10.1016/0006-3002(56)90380-8

Earp, A., Hanson, C. E., Ralph, P. J., Brando, V. E., Allen, S., Baird, M. E., Clementson, L., Daniel, P., Dekker, A. G., Fearns, P. R. C. S., Parslow, J. S., Strutton, P. G., Thompson, P. A., Underwood, M., Weeks, S., Doblin, M. A., 2011. Review of fluorescent standards for calibration of in situ fluorometers: recommendations applied in coastal and ocean observing programs. Optics Express, 19: 26768e26782.

Edwards, A. M., Yool, A., 2000. The role of higher predation in plankton population models. Journal of Plankton Research. 22, 1085-1112. doi: 10.1093/plankt/22.6.1085

Ellwood, M. J., Law, C. S., Hall, J., Woodward, E. M. S., Strzepek, R., Kuparinen, J., Thompson, K., Pickmere, S., Sutton, P., Boyd, P. W., 2013. Relationships between nutrient stocks and inventories and phytoplankton physiological status along an oligotrophic meridional transect in the Tasman Sea. Deep-Sea Research Part I, 72: 102-120.

Evans, G. T., 1999. The role of local models and data sets in the joint global ocean flux study. Deep-Sea Research Part I, 46: 1369–1389. doi: 10.1016/S0967-0637(99) 00010-2

Everett, J. D., Baird M. E., Oke P. R., Suthers I. M., 2012. An avenue of eddies: Quantifying the biophysical properties of mesoscale eddies in the Tasman Sea. Journal of Geophysical Research, 39: L16608. doi:10.1029/2012GL053091

Everett, J. D., Baird, M. E., Oke, P. R., Suthers, I. M., 2012. An avenue of eddies: Quantifying the biophysical properties of mesoscale eddies in the Tasman Sea. Geophysical Research Letters, 39: L16608, doi:10.1029/ 2012GL053091

Everett, J.D., Baird, M.E., Buchanan, P., Bulman, C., Davies, C., Downie, R., Griffiths, C., Heneghan, R., Kloser, R.J., Laiolo, L., Lara-Lopez, A., Lozano-Montes, H., Matear, R.J., McEnnulty, F., Robson, B., Rochester, W., Skerratt, J., Smith, J.A., Strzelecki, J., Suthers, I.M., Swadling, K.M., van Ruth, P., Richardson, A.J., 2017. Modeling What We Sample and Sampling What We Model: Challenges for Zooplankton Model Assessment. Frontiers in Marine Science. 4:77. doi: 10.3389/fmars.2017.00077

Falkowski P.G., Knoll A.H. 2007. Evolution of Primary Producers in the Sea. New York: Elsevier

Falkowski, P. G., 1994. The role of phytoplankton photosynthesis in global biogeochemical cycles. Photosynthesis Research, 39: 235-258.

Falkowski, P. G., 2012. The power of plankton. Nature, 483: 17-20.

Falkowski, P. G., Barber, R. T., Smetacek, V., 1998. Biogeochemical Controls and Feedbacks on Ocean Primary Production. Science, 281: 200–206. doi:10.1126/science.281.5374.200

Falkowski, P. G., Ziemann, D., Kolber, Z., Bienfang, P., 1991. Role of eddy pumping in enhancing primary production in the ocean. Nature, 352: 55-58.

Falkowski, P., 2012. The power of plankton. Nature, 483: 17–20.

Falkowski, P., Ziemann, D., Kolber, Z., Bienfang, P., 1991. Role of eddy pumping in enhancing primary production in the ocean. Nature, 352: 55–58.

Farikou, O., Sawadogo, S., Niang, A., Diouf, D., Brajard, J., Mejia, C., Dandonneau, Y., Gasc, G., Crepon, M., Thiria, S., 2015. Inferring the seasonal evolution of phytoplankton groups in the Senegalo-Mauritanian upwelling region from satellite ocean-color spectral measurements. Journal of Geophysical Research, 120(9): 6581–6601. doi:10.1002/2015JC010738

Fasham, M. J. R, 2003. Ed. Ocean Biogeochemistry (Springer, New York). Chapter 4: Phytoplankton and Their Role in Primary, New, and Export Production Falkowski P.,· Laws A. E. ·.Barber R. T., ·Murray J. W. pp 99-118.

Fasham, M. J. R., Ducklow, H.W., McKelvie, S.M., 1990. A nitrogen-based model of plankton dynamics in the oceanic mixed layer. Journal of Marine Research, 48: 591-639.

Fasham, M. J., Evans, G. T., Kiefer, D. A., Creasey, M., Leach, H., 1995. The use of optimization techniques to model marine ecosystem dynamics at the JGOFS station at 47 degrees N 20 degrees. Philosophical Transactions of the Royal Society B, 348: 203–209. doi: 10.1098/rstb.1995.0062

Fennel W., Neumann, T., 2004. Introduction to the Modelling of Marine Ecosystems. Elsevier Oceanography Series, Volume 72 pp. 297.

Field, C. B., Behrenfeld, M. J., Randerson, J. T., Falkowski, P. G., 1998. Primary Production of the Biosphere: Integrating Terrestrial and Oceanic Components. Science. 281, 237–240. doi:10.1126/science.281.5374.237

Finkel, Z. V., Beardall, J., Flynn, K. J., Quigg, A., Rees, T. A. V., Raven, J. A., 2009. Phytoplankton in a changing world: cell size and elemental stoichiometry. Journal of Plankton Research, 32: 119–137.

doi:10.1093/plankt/fbp098

Flombaum, P., Gallegos, J. L., Gordillo, R. A., Rincon, J., Zabala, L. L., Jiao, N., Karl, D. M., Li, W. K. W., Lomas, M. W., Veneziano, D., Vera, C. S., Vrugt, J. A., Martiny, A. C., 2013. Present and future global distributions of the marine Cyanobacteria Prochlorococcus and Synechococcus. Proceedings of the National Academy of Sciences, 110: 9824-9829.

Follows, M. J., Dutkiewicz, S., 2011. Modeling Diverse Communities of Marine Microbes. Annual Review of Marine Science, 3: 427-451.

Friedrichs, M. A. M., Dusenberry, J. A., Anderson, L. A., Armstrong, R. A., Chai, F., Christian, J. R., Doney, S. C., Dunne, J., Fujii, M., Hood, R., McGillicuddy., D. J., Moore, K. J., Schartau, M., Spitz, Y. H., Wiggert, J. D., 2007. Assessment of skill and portability in regional marine biogeochemical models: Role of multiple planktonic groups. Journal of Geophysical Research, 112(C8): C08001.

Froneman, P. W., Perissinotto, R., 1996. Structure and grazing of the microzooplankton communities of the Subtropical Convergence and warm-core eddy in the Atlantic sector of the Southern Ocean. Marine Ecology Progress Series, 135: 237-245.

Froneman, P. W., Perissinotto, R., Pakhomov, E. A., 1997. Biogeographical structure of the microphytoplankton assemblages in the region of the Subtropical Convergence and across a warm-core eddy during austral winter. Journal of Plankton Research, 19: 519-531.

Frost, B. W., 1991. The role of grazing in nutrient-rich areas of the open sea. Limnology and Oceanography, 36(8): 1616-1630.

Fujii, M., Boss, E., Chai, F., 2007. The value of adding optics to ecosystem models: a case study. Biogeosciences 4, 817-835

Fujiwara, A., Hirawake, T., Suzuki, K., Saitoh, S. I., 2011. Remote sensing of size structure of phytoplankton communities using optical properties of the Chukchi and Bering Sea shelf region. Biogeosciences, 8(12): 3567–3580. doi:10.5194/bg-8-3567-2011

Gharamti, M. E., Samuelsen, A., Bertino, L., Simon, E., Korosov, A., Daewel, U., 2017. Online tuning of ocean biogeochemical model parameters using

ensemble estimation techniques: Application to a one-dimensional model in the North Atlantic. Journal of Marine Systems, 168: 1–16. doi:10.1016/j.jmarsys.2016.12.003

Godfrey, J., Cresswell, G., Golding, T., Pearce, A., Boyd, R., 1980. The separation of the East Australian Current, Journal of Physical Oceanography, 10: 430-440

Gordon, H. R., Brown, O. B., Evans, R. H., Brown, J. W., Smith, R. C., Baker, K. S., Clark, D. K., 1988. A semianalytic radiance model of ocean color. Journal of Geophysical Research, 93(D9): 10909–10924. doi:10.1029/JD093iD09p10909

Gordon, H. R., Morel, A., 1983. Remote Assessment of Ocean Color for Interpretation of Satellite Visible Imagery: A Review, 114 pp., Springer, New York.

Guidi, L., L. Legendre, G. Reygondeau, J. Uitz, L. Stemman, Henson S., 2015. A new look at ocean carbon remineralization for estimating deepwater sequestration, Global Biogeochemical Cycles, 29: 1044–1059, doi:10.1002/2014GB005063.

Hallegraeff, G. M., 1981. Seasonal Study of Phytoplankton Pigments and Species at a Coastal Station off Sydney: Importance of Diatoms and the Nanoplankton. Marine Biology, 61: 107-118.

Hamon, B. V., 1965. The East Australian Current, 1960-1964. Deep-Sea Research, 12: 889-921.

Hassler, C. S., Djajadikarta, J. R., Doblin, M. A., Everett, J. D., Thompson, P. A., 2010. Characterisation of water masses and phytoplankton nutrient limitation in the East Australian Current separation zone during spring 2008. Deep-Sea Research Part II, 58(5): 664–677. doi:10.1016/j.dsr2.2010.06.008

Haury, L. R., 1984. An Offshore Eddy in the California Current System Part IV: Plankton Distributions. Progress in Oceanography, 13: 95-111.

Hemmings, J. C. P., Srokosz, M. A., Challenor, P., Fasham, M. J. R., 2003. Assimilating satellite ocean-colour observations into oceanic ecosystem models. Philosophical Transactions of the Royal Society A, 361: 33–39.

doi:10.1098/rsta.2002.1104

Hirata, T., Hardman-Mountford, N. J., Brewin, R. J. W., Aiken, J., Barlow, R., Suzuki, K., Isada, T., Howell, E., Hashioka, T., Noguchi-Aita, M., Yamanaka, Y., 2011. Synoptic relationships between surface Chlorophyll-a and diagnostic pigments specific to phytoplankton functional types. Biogeosciences, 8(2): 311–327. doi:10.5194/bg-8-311-2011

Hobday, A. J., Hartmann, K., 2006. Near real-time spatial management based on habitat predictions for a longline bycatch species. Fisheries Management and Ecology, 13: 365–380. doi: 10.1111/j.1365-2400.2006.00515.x

Hobday, A. J., Young, J. W., Moeseneder, C., Dambacher, J. M., 2011. Defining dynamic pelagic habitats in oceanic waters off eastern Australia. Deep-Sea Research II 58 (5): 734-745

Hoepffner, N., Sathyendranath, S., 1991. Effect of Pigment Composition on Absorption Properties of Phytoplankton. Marine Ecology Progress Series, 73: 11–23.

Hooker, S. B., Clementson, L., Thomas, C.S., Schlüter, L., Allerup, M., Ras, J., Claustre, H., Normandeau, C., Cullen, J., Kienast, M., Kolowski, W., Vernet, M., Chakraborty, S., Lohrenz, S., Tuel, M., Redalje, D., Cartaxana, P., Mendes, C. R., Brotas, V., Matondkar, S. G. P., Parab, S.G., Neeley, A., Egeland, E. S. 2012. The fifth SeaWiFS HPLC Analysis Round-Robin Experiment (SeaHARRE–5), NASA Technical Memorandum 2012–217503. NASA Goddard Space Flight Center, Maryland.

Huang, B., Hu, J., Xu, H., Cao, Z., Wang, D., 2010. Phytoplankton community at warm eddies in the northern South China Sea in winter 2003/2004. Deep-Sea Research Part II, 57: 1792-1798

Huys, R., Boxshall, G.A., 1991. Copepod Evolution, volume 159, The Ray Society, London

Iglesias-Rodríguez, M. D., Brown, C. W., Doney, S. C., Kleypas, J., Kolber, D., Kolber, Z., Hayes, P. K., Falkowski, P. G., 2002. Representing key phytoplankton functional groups in ocean carbon cycle models: Coccolithophorids. Global Biogeochemical Cycles, 16(4), 1100.

Iglesias-Rodriguez, M. D., Halloran, P. R., Rickaby, R. E. M., Hall, I. R.,

Colmenero-Hidalgo, E., Gittins, J. R., Green, D.R.H., Tyrrell, T., Gibbs, S.J., von Dassow, P., Rehm, E., Armbrust, E.V., Boessenkool, K. P., 2008. Phytoplankton Calcification in a High-CO2 World. Science, 320(5874): 336-340.

IOCCG, (2006). Remote Sensing of Inherent Optical Properties: Fundamentals, Tests of Algorithms, and Applications. Lee, Z.-P. (ed.), Reports of the International Ocean-Colour Coordinating Group, No. 5, IOCCG, Dartmouth, Canada

Irigoien, X., 2005. Phytoplankton blooms: a “loophole” in microzooplankton grazing impact? Journal of Plankton Research, 27(4): 313-321.

Jeffrey, S. W., Hallegraeff, G. M., 1980. Studies of Phytoplankton Species and Photosynthetic Pigments in a Warm Core Eddy of the East Australian Current. II. A Note on Pigment Methodology. Marine Ecology Progress Series, 3: 295–301.

Jenkins, W., 1988. Nitrate flux into the euphotic zone near Bermuda. Nature, 331: 521-523.

Jennings, S., Mackinson, S., 2003. Abundance-body mass relationships in size-structured food webs. Ecology Letters. 6, 971-974

Jonasz, M., Fournier, G., 2007. Light Scattering by Particles in Water: Theoretical and Experimental Foundations: Theoretical and Experimental Foundations. 1st ed. London: Academic Press, 714 pp.

Jones, E. M., Baird, M. E., Mongin, M., Parslow, J., Skerratt, J., Lovell, J., Margvelashvili, N., Matear, R. J., Wild-Allen, K., Robson, B., Rizwi, F., Oke, P., King, E., Schroeder, T., Steven, A., Taylor, J., 2016. Use of remote-sensing reflectance to constrain a data assimilating marine biogeochemical model of the Great Barrier Reef. Biogeosciences, 13(23): 6441–6469. doi:10.5194/bg-13-6441-2016

Kanwisher, J., 1963. On the exchange of gases between the atmosphere and the sea. Deep-Sea Research, 10: 195-207.

Kettle, H., Merchant, C. J., 2008. Modeling ocean primary production: sensitivity to spectral resolution of attenuation and absorption of light. Progress in Oceanography, 78: 135-146.

Kidston, M., Matear, R. J., Baird, M. E., 2011. Parameter optimisation of a marine ecosystem model at two contrasting stations in the Sub-Antarctic Zone. Deep Sea Research Part II, 58: 2301–2315. doi:10.1016/j.dsr2.2011.05.018

Kidston, M., Matear, R., Baird, M. E., 2013. Phytoplankton growth in the Australian sector of the Southern Ocean, examined by optimising ecosystem model parameters. Journal of Marine Systems, 128: 123-137. doi:10.1016/j.jmarsys.2013.04.011

Kirk, J. T. O., 1975. A theoretical analysis of the contribution of algal cells to the attenuation of light within natural waters. I. General treatment of suspensions of pigmented cells. New Phytologist, 75: 11-20.

Kirk, J. T. O., 1976. A Theoretical Analysis of the Contribution of Algal Cells to the Attenuation of Light within Natural Waters. III. Cylindrical and Spheroidal Cells. New Phytologist, 77: 341–58.

Kirk, J. T. O., 1983. Light and photosynthesis in aquatic ecosystems. 401 pp. Cambridge – London – New York: Cambridge University Press 1983.

Kirk, J. T. O., 1991. Volume scattering function, average cosines, and the underwater light field. Limnology and Oceanography, 36: 455-467.

Kirk, J. T. O., 1994. Light and Photosynthesis in Aquatic Ecosystems, second ed. Cambridge University Press, Cambridge.

Klein, P., Lapeyre, G., 2009. The Oceanic Vertical Pump Induced by Mesoscale and Submesoscale Turbulence. Annual Review of Marine Science, 1(1): 351-375. doi:10.1146/annurev.marine.010908.163704

Kruger, J., 1993. Simulated annealing: a tool for data assimilation into an almost steady model state. Journal of Physical Oceanography, 23: 679-688.

Laiolo, L., Barausse, A., Dubinsky, Z., Palmeri, L., Goffredo, S., Kamenir, Y., Al-Najjar, T., Iluz, D., 2014. Phytoplankton dynamics in the Gulf of Aqaba (Eilat, Red Sea): A simulation study of mariculture effects. Marine Pollution Bulletin, 86: 481–493. doi:10.1016/j.marpolbul.2014.06.026

Laiolo, L., McInnes, A. S., Matear, R. J., Doblin, M. A., 2016. Key Drivers of Seasonal Plankton Dynamics in Cyclonic and Anticyclonic Eddies off East Australia. Frontiers in Marine Science, 3, 492.

doi:10.3389/fmars.2016.00155

Lancelot, C., Hannon, E., Becquevort, S., Veth, C., De Baar, H. J. W., 2000. Modeling phytoplankton blooms and carbon export production in the Southern Ocean: dominant controls by light and iron in the Atlantic sector in Austral spring 1992. Deep-Sea Research I, 47: 1621-1662.

Large, W. G., Yeager, S. G., 2008. The global climatology of an interannually varying air–sea flux data set. Climate Dynamics, 33: 341–364. doi: 10.1007/s00382-008- 0441-3

Lee-Lueng, F., Chelton, D. B., Le Traon, P., Morrow, R., 2010. Eddy dynamics from satellite altimetry. Oceanography, 23(4): 14-25

Lee, T. N., Yoder, J. A., Atkinson, L. P., 1991. Gulf Stream frontal eddy influence on productivity of the southeast U.S. continental shelf. Journal of Geophysical Research, 96(22): 191-205.

Lee, Z., Carder, K. L., Arnone, R. A., 2002. Deriving inherent optical properties from water color: a multiband quasi-analytical algorithm for optically deep waters. Applied Optics, 41: 5755-5772.

Levy, M., Klein, P., 2004. Does the low frequency variability of mesoscale dynamics explain a part of the phytoplankton and zooplankton spectral variability? Proceedings of the Royal Society A: Mathematical, Physical and Engineering Sciences, 460: 1673–1687. doi:10.1098/rspa.2003.1219

Levy, M., Klein, P., Treguier, A. M., 2001. Impact of sub-mesoscale physics on production and subduction of phytoplankton in an oligotrophic regime. Journal of Marine Research, 59: 535-565.

Li, Z., Li, L., Song, K., Cassar, N., 2013. Estimation of phytoplankton size fractions based on spectral features of remote sensing ocean color data. Journal of Geophysical Research: Oceans, 118(3): 1445–1458. doi:10.1002/jgrc.20137

Link, J., 2002. Does food web theory work for marine ecosystems? Marine Ecology Progress Series. 230, 1–9

Lochte, K., Pfannkuche, O., 1987. Cyclonic cold-core eddy in the eastern North Atlantic. II. Nutrients, phytoplankton and bacterioplankton. Marine Ecology Progress Series, 39: 153-164

Longhurst, A., Sathyendranath, S., Platt, T., Caverhill, C., 1995. An estimate of global primary production in the ocean from satellite radiometer data. Journal of Plankton Research, 17: 1245–1271. doi:10.1093/plankt/17.6.1245

Macdonald, H. S., Roughan, M., Baird, M. E., Wilkin, J., 2016. The formation of a cold-core eddy in the East Australian Current. Continental Shelf Research, 114(C): 72-84. doi:10.1016/j.csr.2016.01.002

Mann, D. G., 1999. The species concept in diatoms. Phycologia, 38: 437–495. doi:10.2216/i0031-8884-38-6-437.1

Marañón E., 2015. Cell Size as a Key Determinant of Phytoplankton Metabolism and Community Structure. Annual Review of Marine Science, 7: 241-264.

Maritorena, S., Siegel, D. A., 2005. Consistent merging of satellite ocean color data sets using a bio-optical model. Remote Sensing of Environment, 94(4): 429–440. doi:10.1016/j.rse.2004.08.014

Marra, J., Trees, C. C., O'Reilly, J. E., 2007. Phytoplankton pigment absorption: A strong predictor of primary productivity in the surface ocean. Deep Sea Research Part I: Oceanographic Research Papers, 54: 155–163. doi:10.1016/j.dsr.2006.12.001

Mata, M. M., Tomczak, M., Wijffels, S., Church, J. A., 2000. East Australian Current volume transports at 30 degrees S: estimates from the World ocean circulation experiment hydrographic sections PR11/P6 and the PCM3 current meter array. Journal of Geophysical Research, 105: 28509–28526. doi: 10.1029/1999JC000121

Matear, R. J., 1995. Parameter optimization and analysis of ecosystem models using simulated annealing: A case study at Station P. Journal of Marine Research, 53(4): 571–607. doi:10.1357/0022240953213098

Matear, R. J., Chamberlain, M. A., Sun, C., Feng, M., 2013. Climate change projection of the Tasman Sea from an Eddy-resolving Ocean Model. Journal of Geophysical Research: Oceans, 118(6): 2961-2976. doi:10.1002/jgrc.20202

McAndrew, P. M., Bjorkman, K. M., Church, M. J., Morris, P. J., Jachowski, N., Williams, P. J. L. B., Karl, D. M., 2007. Metabolic response of oligotrophic

plankton communities to deep water nutrient enrichment. Marine Ecology Progress Series, 332: 63–75. doi:10.3354/meps332063

McClain, C. R., 2009. A Decade of Satellite Ocean Color Observations*. Annual Review of Marine Science, 1(1): 19–42. doi:10.1146/annurev.marine.010908.163650

McGillicuddy, D. J., Robinson, A. R., 1998. Interaction between the oceanic mesoscale and the surface mixed layer. Dynamics of Atmospheres and Oceans: 27, 549–574. doi:10.1016/s0377-0265(97)00030-4

McGillicuddy, D. J., Robinson, A. R., Siegel, A. A., Jannasch, H. W., Johnson, R., Dickey, T. D., McNeil, J., Michaels, A. F., Knap, A. H., 1998. Influence of mesoscale eddies on new production in the Sargasso Sea. Nature, 394: 263-266.

McGillicuddy, D., 2015. Mechanisms of Physical - Biological - Biogeochemical Interaction at the Oceanic Mesoscale. Annual Review of Marine Science, (8), 13.1-13.36. doi:10.1146/annurev-marine-010814-015606

McGillicuddy, D., Robinson, A., 1997. Eddy-induced nutrient supply and new production in the Sargasso Sea. Deep Sea Research Part I, 44: 1427–1450. doi: 10.1016/S0967-0637(97)00024-1

McWilliams, J. C., 2008. The nature and consequences of oceanic eddies. Ocean Modeling in an Eddying Regime. American Geophysical Union, 177: 5–15. doi: 10.1029/177GM03

Mitra, A., 2009. Are closure terms appropriate or necessary descriptors of zooplankton loss in nutrient–phytoplankton–zooplankton type models? Ecological Modelling. 220, 611-620. doi: 10.1016/j.ecolmodel.2008.12.008

Mobley, C. D., 1994. Light and water: radiative transfer in natural waters, Academic Press, San Diego, CA.

Mobley, C. D., Stramski, D., Bissett, P., Boss, E., 2004. Optical Modeling of Ocean Waters: Is the Case 1 - Case 2 Classification Still Useful? Oceanography, 17(2): 60–67. doi:10.5670/oceanog.2004.48

Moheimani, N. R., Webb, J. P., Borowitzka, M. A., 2012. Bioremediation and other potential applications of coccolithophorid algae: A review. Algal Research, 1: 120-133.

Moline, M. A., Prezelin, B. B., 2000. Optical fractionation of chlorophyll and primary production for coastal waters of the Southern Ocean. Polar Biology, 23: 129-136.

Moloney, C. L., Field, J. G., 1991. The size-based dynamics of plankton food webs. I. A simulation model of carbon and nitrogen flows. Journal of Plankton Research, 13(5): 1003-1038.

Montoya, J. P., Holl, C. M., Zehr, J. P., Hansen, A., Villareal, A., Capone, D. G., 2004. High rates of N2 fixation by unicellular diazotrophs in the oligotrophic Pacific Ocean. Nature, 430: 1027-1031.

Moore, C.M., Suggett, D. J., Hickman, A. E., Kim, Y. N., Tweddle, J.F., Sharples, J., Geider, R. J., Holligan, P. M., 2006. Phytoplankton photoacclimation and photoadaptation in response to environmental gradients in a shelf sea. Limnology and Oceanography, 51(2): 936-949

Moore, T. S., Matear, R. J., Marra, J., Clementson, L., 2007. Phytoplankton variability off the Western Australian Coast: Mesoscale eddies and their role in cross-shelf exchange. Deep Sea Research Part II: Topical Studies in Oceanography, 54(8-10): 943-960. doi:10.1016/j.dsr2.2007.02.006

Morel, A., Ahn, Y., Partensky, F., Vaulot, D., Claustre, H., 1993. Prochlorococcus and Synechococcus: A comparative study of their optical properties in relation to their size and pigmentation. Journal of Marine Research, 51: 617-649.

Morel, A., Bricaud, A., 1981. Theoretical Results Concerning the Optics of Phytoplankton with Special References to Remote Sensing Applications. In Oceanography from Space. Plenum Press, Venice, Italy

Morel, A., Huot, Y., Gentili, B., Werdell, P. J., Hooker, S. B., & Franz, B. A., 2007. Examining the consistency of products derived from various ocean color sensors in open ocean (Case 1) waters in the perspective of a multi-sensor approach. Remote Sensing of Environment, 111(1), 69–88. doi:10.1016/j.rse.2007.03.012

Morel, A., Maritorena, S., 2001. Bio-optical properties of oceanic waters: A reappraisal. Journal of Geophysical Research, 106(C4): 7163–7180. doi:10.1029/2000JC000319

Morel, A., Prieur, L., 1977. Analysis of variations in ocean color. Limnology and Oceanography, 22: 709–722. doi:10.4319/lo.1977.22.4.0709

Mouw, C. B., Hardman-Mountford, N. J., Alvain, S., Bracher, A., Brewin, R. J. W., Bricaud, A., Ciotti, A. M., Devred, E., Fujiwara, A., Hirata, T., Hirawake, T., Kostadinov, T. S., Roy, S., Uitz, J., 2017. A Consumer's Guide to Satellite Remote Sensing of Multiple Phytoplankton Groups in the Global Ocean. Frontiers in Marine Sceince, 4:41. doi: 10.3389/fmars.2017.00041

Mouw, C. B., Barnett, A., McKinley, G. A., 2016. Phytoplankton size impact on export flux in the global ocean. Global Biogeochemical Cycles, 30(10), 1542–1562. http://doi.org/10.1002/2015GB005355.

Mouw, C. B., Yoder, J. A., Doney, S. C., 2012. Impact of phytoplankton community size on a linked global ocean optical and ecosystem model. Journal of Marine Systems, 89: 61–75. doi:10.1016/j.jmarsys.2011.08.002

Natvik, L. J., Evensen G., 2003. Assimilation of ocean colour data into a biochemical model of the North Atlantic. Journal of Marine Systems, 40-41: 127–153. doi:10.1016/S0924-7963(03)00016-2

Nilsson, C. S., Cresswell, G. R., 1981. The formation and evolution of East Australian Current warm-core eddies. Progress in Oceanography, 9: 133-183.

O'Reilly, J. E., Maritorena, S., Mitchell, B. G., Siegel, D. A., Carder, K. L., Garver, S. A., Kahru, M., McClain, C., 1998. Ocean color chlorophyll algorithms for SeaWiFS. Journal of Geophysical Research: Oceans (1978–2012) 103, 24937–24953. doi:10.1029/98JC02160

Odermatt, D., Gitelson, A., Brando, V. E., Schaepman, M., 2010. Review of constituent retrieval in optically deep and complex waters from satellite imagery. Remote Sensing Environment, 118: 1–11. doi:10.1016/j.rse.2011.11.013

Officer, C. B., Ryther, J. H., 1980. The Possible Importance of Silicon in Marine Eutrophication. Marine Ecology Progress Series, 3: 83–91. doi:10.3354/meps003083

Officier, C. B., Ryther, J. H., 1980. The Possible Importance of Silicon in Marine Eutrophication. Marine Ecology Progress Series, 3: 83-91.

Oke, P. R., Brassington, G. B., Griffin, D. A., Schiller, A., 2008. The Bluelink ocean data assimilation system (BODAS). Ocean Modelling, 21(1-2): 46-70. doi:10.1016/j.ocemod.2007.11.002

Oke, P. R., Griffin, D.A., 2011. The cold-core eddy and strong upwelling off the coast of New South Wales in early 2007. Deep-Sea Research II, 58 (5): 574–591.

Oke, P.R., Middleton, J.H., 2001. Nutrient enrichment off Port Stephens: the role of the East Australian Current. Continental Shelf Research 21: 587-606

Olaizola, M., Ziemann, D. A., Bienfang, P. K., Walsh, W. A., Conquest, L. D., 1993. Eddy-induced oscillations of the pycnocline affect the floristic composition and depth distribution of phytoplankton in the subtropical Pacific. Marine Biology, 116, 533-542.

Oschlies, A., Garcon, V., 1998. Eddy induced enhancement of primary production in a model of the North Atlantic Ocean. Nature, 394: 266-269.

Oubelkheir, K., Clementson, L. A., Webster, I. T., Ford, P. W., Dekker, A. G., Radke, L. C., Daniel, P., 2006. Using inherent optical properties to investigate biogeochemical dynamics in a tropical macrotidal coastal system. Journal of Geophysical Research, 111(C7), C07021. doi:10.1029/2005JC003113

Paerl, H. W., Huisman, J., 2008. Blooms Like It Hot. Science, 320: 57-58.

Partensky, F., Blanchot, J., Vaulot, D., 1999a. Differential distribution and ecology of Prochlorococcus and Synechococcus in oceanic waters: a review. Bulletin de l'Institut oceanographique, Monaco 19: 457–475.

Partensky, F., Hess, W. R., Vaulot, D., 1999. Prochlorococcus, a Marine Photosynthetic Prokaryote of Global Significance. Microbiology and Molecular Biology Reviews, 63: 106-127.

Pauly, D., Christensen, V., 1995. Primary production required to sustain global fisheries. Nature, 344: 255-257.

Pegau, W. S., Boss, E., Martínez, A., 2002. Ocean color observations of eddies during the summer in the Gulf of California. Geophysical Research Letters, 29: 6–1–6–3. doi:10.1029/2001GL014076

Pilo, G. S., Mata, M. M., Azevedo, J. L. L., 2015. Eddy surface properties and

propagation at Southern Hemisphere western boundary current systems. Ocean Science, 11(4): 629-641. doi:10.5194/os-11-629-2015

Pitcher, G. C., Walker, D. R., Mitchell-Innes, B. A., Moloney, C. L., 1991. Short-term variability during an anchor station study in the southern Benguela upwelling system: Phytoplankton dynamics. Progress in Oceanography: 28: 39–64. doi:10.1016/0079-6611(91)90020-m

Postgate, J., 1998. Nitrogen Fixation. Edward Arnold, London. pp 109.

Poulain, P-M., Mauri, E., Ursella, L., 2004. Unusual upwelling event and current reversal off the Italian Adriatic coast in summer 2003. Geophysical Research Letters, 31 (5): L05303 doi:10.1029/2003GL019121

Pritchard, T. R., Lee, R. S., Ajani, P. A., Rendell, P. S., Black, K., Koop, K., 2003. Phytoplankton Responses to Nutrient Sources in Coastal Waters off Southeastern Australia. Aquatic Ecosystem Health & Management, 6(2): 105-117.

Raven, J. A., 1998. The twelfth Tansley Lecture. Small is beautiful: the picophytoplankton. Functional Ecology, 12: 503-513.

Redfield, A. C., 1934. On the proportions of organic derivatives in sea water and their relation to the composition of plankton. Daniel R., J. editor. James Johnstone Memorial Volume. University Press of Liverpool, pp. 177-92.

Redfield, A. C., Ketchum, B., Richards, F. 1963. The influence of organisms on the composition of sea-water. Hill M. editor. The Sea. Interscience, New York, pp. 26-77.

Ridgway, K. R., Dunn, J. R., 2003. Mesoscale structure of the mean East Australian Current System and its relationship with topography. Progress in Oceanography, 56: 189–222. doi:10.1016/S0079-6611(03)00004-1

Ridgway, K. R., Dunn, J. R., Wilkin, J. L., 2002. Ocean interpolation by four-dimensional least squares -Application to the waters around Australia. Journal of Atmospheric and Oceanic Technology, 19: 1357–1375. doi: 10.1175/1520- 0426(2002)019<1357:OIBFDW>2.0.CO;2

Robinson, A. R., 1983. Eddies in Marine Science, Springer, New York, 609pp.

Robinson, I. S., 2004. Measuring the ocean from space: The Principles and Methods of Satellite Oceanography Praxis Publishing, Ed. Springer, UK,

669 pp.

Robinson, I. S., 2004. Measuring the ocean from space: The Principles and Methods of Satellite Oceanography Praxis Publishing, Springer, UK, 669pp.

Rodriguez, F., Varela, M., Fernandez, E., Zapata, M., 2003. Phytoplankton and pigment distributions in an anticyclonic slope water oceanic eddy (SWODDY) in the southern Bay of Biscay. Marine Biology, 143: 995–1011. doi: 10.1007/s00227- 003-1129-1

Roemmich, D., Gilson, J., Willis, J., Sutton, P., Ridgway, K., 2005. Closing the Time-Varying Mass and Heat Budgets for Large Ocean Areas: The Tasman Box. Journal of Climate. 18, 2330-2343.

Roughan, M., Middleton, J. H., 2002. A comparison of observed upwelling mechanisms off the east coast of Australia. Continental Shelf Research, 22: 2551–2572. doi:10.1016/S0278-4343(02)00101-2

Roy, S., Sathyendranath, S., Platt, T., 2011. Retrieval of phytoplankton size from bio-optical measurements: theory and applications. Journal of the Royal Society Interface, 8(58): 650–660. doi:10.1098/rsif.2010.0503

Ryther, J.H., 1969. Photosynthesis and fish production in the sea Science. 166, 72-76

Sadeghi, A., Dinter, T., Vountas, M., Taylor, B. B., Altenburg-Soppa, M., Peeken, I., Bracher, A., 2012. Improvement to the PhytoDOAS method for identification of coccolithophores using hyper-spectral satellite data. Ocean Science, 8(6): 1055–1070. doi:10.5194/os-8-1055-2012

Salihoglu, B., Hofmann, E. E., 2007. Simulations of phytoplankton species and carbon production in the equatorial Pacific Ocean 1. Model configuration and ecosystem dynamics. Journal of Marine Research, 65: 219-273.

Sallée, J. B., Llort, J., Tagliabue, A., Levy, M., 2015. Characterization of distinct bloom phenology regimes in the Southern Ocean. ICES Journal of Marine Science, 72(6): 1985-1998. doi:10.1093/icesjms/fsv069

Sathyendranath, S., Platt, T., 2007. Spectral effects in bio-optical control on the ocean system. Oceanologia, 49: 5-39.

Schroeder, T., Behnert, I., Schaale, M., Fischer, J., Doerffer, R., 2007.

Atmospheric correction algorithm for MERIS above case-2 waters. International Journal of Remote Sensing, 28(7): 1469–1486. doi:10.1080/01431160600962574

Sherr, E.B., Sherr, B.F., 1994. Bactivory and herbivory: key roles of phagotrophic protists in pelagic food webs Microbial Ecology. 28, 223–235

Shulman, I., Frolov, S., Anderson, S., Penta, B., Gould, R., Sakalaukus, P., Ladner, S., 2013. Impact of bio-optical data assimilation on short-term coupled physical, bio-optical model predictions. Journal of Geophysical Research, 118(4): 2215–2230. doi:10.1002/jgrc.20177

Sonntag, S., Hense, I., 2011. Phytoplankton behavior affects ocean mixed layer dynamics through biological-physical feedback mechanisms. Geophysical Research Letters, 38(15): L15610, doi:10.1029/2011GL048205

Stock, C. A., Powell, T. M., Levin, S. A., 2008. Bottom-up and top-down forcing in a simple size-structured plankton dynamics model. Journal of Marine Systems, 74(1-2): 134–152.

Stramski, D., Kiefer, D. A., 1991. Light scattering by microorganisms in the open ocean. Progress in Oceanography, 28: 343–383.

Sullivan, J. M., Twardowski, M. S., 2009. Angular Shape of the Oceanic Particulate Volume Scattering Function in the Backward Direction. Applied Optics, 48(35): 6811. https://doi.org/10.1364/AO.48.006811.

Sunda, W. G., Huntsman, S. A., 1992. Feedback interactions between zinc and phytoplankton in seawater. Limnology and Oceanography, 37(1): 25-40

Sverdrup H. U., 1953. On conditions for the vernal blooming of phytoplankton. Journal Du Conseil, 18: 287-295.

Szeto, M., Werdell, P. J., Moore, T. S., & Campbell, J. W., 2011. Are the world's oceans optically different? Journal of Geophysical Research, 116(7), 2019. doi:10.1029/2011JC007230

Teruzzi, A., Dobricic, S., Solidoro, C., Cossarini, G., 2014. A 3-D variational assimilation scheme in coupled transport-biogeochemical models: Forecast of Mediterranean biogeochemical properties. Journal of Geophysical Research, 119(1): 200–217. doi:10.1002/2013JC009277

The Ring Group, 1981. Gulf Stream cold-core rings: their physics, chemistry and

biology. Science, 212: 1091-1100.

Thingstad, F. T., Strand, E., Larsen, A., 2010. Stepwise building of plankton functional type (PFT) models: A feasible route to complex models? Progress in Oceanography, 84: 6-15.

Thompson, P. A., Baird, M. E., Ingleton, T., Doblin, M. A., 2009. Long-term changes in temperate Australian coastal waters: implications for phytoplankton. Marine Ecology Progress Series, 394: 1-19.

Thompson, P. A., Bonham, P., Waite, A. M., Clementson, L. A., Cherukuru, N., Hassler, C., Doblin, M. A., 2011. Contrasting oceanographic conditions and phytoplankton communities on the east and west coasts of Australia. Deep-Sea Research Part II, 58(5): 645-663. doi:10.1016/j.dsr2.2010.10.003

Tilburg, C. E., Hurlburt, H. E., O'Brien, J. J., Shriver, J. Y., 2001. The dynamics of the East Australian current system: the Tasman Front, the East Auckland Current, and the East Cape Current. Journal of Physical Oceanography 31: 2917-2943.

Tilburg, C. E., Subrahmanyam, B., O'Brien, J. J., 2002. Ocean color variability in the Tasman Sea. Geophysical Research Letters, 29: 125–1–125–4. doi:10.1029/2001GL014071

Timmermann, A., Jin, F., 2002. Phytoplankton influences on tropical climate. Geophysical Research Letters, 29(23): 2104, doi:10.1029/2002GL015434

Tranter, D. J., Carpenter, D. J., Leech, G. S., 1986. The Coastal Enrichment Effect of the East Australian Current Eddy Field. Deep-Sea Research Part a-Oceanographic Research Papers, 33: 1705. doi:10.1016/0198-0149(86)90075-0

Tranter, D. J., Leech, G. S., Vaudrey, D. J., 1982. Biological significance of surface flooding in warm-core ocean eddies. Nature, 297: 572-574.

Tranter, D. J., Parker, R. R., Cresswell, G.R., 1980. Are warm-core eddies unproductive? Nature, 284: 540-542.

Tréguer P., Nelson, D.M., Van, Bennekom, A.J., DeMaster, D.J., Leynaert, A., Quéguiner, B., 1995. The silica balance in the world ocean: A reestimate. Science, 268: 375-379.

Vaillancourt, R. D., Brown, C. W., Guillard, R. R. L., Balch, W. M. 2004. Light backscattering properties of marine phytoplankton: relationships to cell size, chemical composition and taxonomy. Journal of Plankton Research, 26 (2): 191–212. doi:10.1093/plankt/fbh012

Vaillancourt, R. D., Marra, J., Seki, M. P., Parsons, M. L., Bidigare, R. R., 2003. Impact of a cyclonic eddy on phytoplankton community structure and photosynthetic competency in the subtropical North Pacific Ocean. Deep-Sea Research Part I, 50: 829–847. doi:10.1016/S0967-0637(03)00059-1

Vallina, S. M., Follows, M. J., Dutkiewicz, S., Montoya, J. M., Cermeno, P., Loreau, M., 2014. Global relationship between phytoplankton diversity and productivity in the ocean. Nature Communications, 5: 4299. doi:10.1038/ncomms5299

Van Heukelem, L., Thomas, C. S., 2001. Computer-assisted high-performance liquid chromatography method development with applications to the isolation and analysis of phytoplankton pigments. Journal of Chromatography A, 910: 31-49.

Volten, H., de Haan, J. F., Hovenier, J. W., Schreurs, R., Vassen, W., Dekker, A. G., Hoogenboom, H. J., Charlton, F., Wouts, R., 1998. Laboratory Measurements of Angular Distributions of Light Scattered by Phytoplankton and Silt. Limnology and Oceanography, 43 (6): 1180–1197.

Wellek, S., 2010. Testing Statistical Hypotheses of Equivalence, Chapman and Hall/CRCm, 431 pp.

Witkowski, K., Król, T., Zieliński, A., Kuteń, E., 1998. A Light-Scattering Matrix for Unicellular Marine Phytoplankton. Limnology and Oceanography, 43: 859–69.

Witty, M., 2011. The White Cliffs of Dover are an Example of Natural Carbon Sequestration. Ecologia, 1: 23-30.

Wu, L., Cai, W., Zhang, L., Nakamura, H., Timmermann, A., Joyce, T., McPhaden, M. J., Alexander, M., Qiu, B., Visbeck, M., Chang, P., Giese, B., 2012. Enhanced warming over the global subtropical western boundary currents. Nature Climate Change, 2(3): 161-166.

Yasuda, I., Ito, S., Shimizu, Y., Ichikawa, K., Ueda, K., Honma, T., Uchiyama, M.,

Watanabe, K., Sunou, N., Tanaka, K., Koizumi, K., 2000. Cold-Core Anticyclonic Eddies South of the Bussol' Strait in the Northwestern Subarctic Pacific. Journal of Physical Oceanography, 30: 1137-1157.

Yool, A., Tyrrell, T., 2003. Role of diatoms in regulating the ocean's silicon cycle. Global Biogeochemical Cycles, 17 (4): 1103-1124.